Eumelanin and polydopamine: self-assembly, structure, and properties

by

Chun-Teh Chen

B.S., Civil Engineering
National Central University, 2006
M.S., Civil Engineering
National Taiwan University, 2009

Submitted to the Department of Civil and Environmental Engineering
in partial fulfillment of the requirements for the degree of

Doctor of Philosophy

at the

MASSACHUSETTS INSTITUTE OF TECHNOLOGY

September 2016

Signature redacted
Author ....
Department of Civil and Environmental Engineering
Aug 18, 2016

Signature redacted
Certified by..... ....
Markus J. Buehler
Professor of Civil and Environmental Engineering
Thesis Supervisor

Signature redacted
Accepted by... ....
Jesse H. Kroll
Associate Professor of Civil and Environmental Engineering
Chair, Graduate Education Committee

Eumelanin and polydopamine: self-assembly, structure, and properties

by

Chun-Teh Chen

Submitted to the Department of Civil and Environmental Engineering
on Aug 18, 2016, in partial fulfillment of the
requirements for the degree of
Doctor of Philosophy

Abstract

In this thesis, a detailed hierarchical structure of eumelanin is described and validated in molecular dynamics simulations. For the first time, the gap between primary, secondary, and aggregate structures of eumelanin is bridged. Based on the hierarchical structure, a new explanation of the photoprotective function of eumelanin is proposed. The interplay of geometric order and disorder characteristics of the hierarchical structure results in significant and random excitonic couplings among eumelanin protomolecules. Consequently, these couplings broaden the spectrum and give rise to a relative enhancement of absorption intensity at the higher-energy end. To provide a more in-depth understanding of the structure–property relationship for exploring practical applications of synthetic eumelanin, polydopamine (PDA), a model that mimics the polymerization mechanism of eumelanin via controlled *in silico* covalent cross-linking is presented. The results show the possibility of tuning the molecular structures and mechanical properties of eumelanin by controlling the extent of polymerization. Since the lack of well-defined and readily available structures for eumelanin has hindered the progress of computational studies in this field, a set of more realistic molecular models for eumelanin is proposed. A brute-force algorithm is used to generate and evaluate probable molecular structures of eumelanin. The most stable dimers, trimers, and tetramers of eumelanin protomolecules are identified. The results show that more planar molecular structures have a tendency to be more stable; thus, they are more likely to exist. Combining these molecular models, the heterogeneous nature of eumelanin as well as the structural planarity of its protomolecules can both be satisfied. One of the most extensively studied applications of PDA is in the form of a component in graphene oxide (GO) nanocomposites. Here, explanations of the enhanced mechanical properties and shrinking ability in response to the environmental humidity of GO–PDA nanocomposites are proposed.

Thesis Supervisor: Markus J. Buehler
Title: Professor of Civil and Environmental Engineering

To my family and my love

Acknowledgments

My Ph.D. journey began when I first stepped into room 1-236 and started to work in the Laboratory for Atomistic and Molecular Mechanics (LAMM) in the fall of 2011. I learned new things every day and met incredible and passionate people along the way. This thesis is the end of this journey. I would like to thank all of those who helped make this thesis possible and my Ph.D. an unforgettable experience.

I would like to express my appreciation and gratitude to my advisor, Prof. Markus J. Buehler who guided, inspired, and encouraged me during these past years. He always gave me priceless advice about my research, presentations, and career. Words cannot express how thankful I am to have had such a fantastic advisor. I would also like to thank my committee members, Prof. Timothy K. Lu, Prof. Heather J. Kulik, and Prof. Xuanhe Zhao. I am extremely grateful for their expertise and guidance. Their comments and suggestions improved this thesis by leaps and bounds. This research was funded by the Public Research Centre Henri Tudor (CRP Henri Tudor) and Taiwan Government whose support is greatly appreciated.

I would like to thank all my collaborators: Vincent Ball, Igor Bdikin, Jianshu Cao, Chern Chuang, Marco d'Ischia, Jose Gracio, Gang Seob Jung, Shangchao Lin, Shengjie Ling, Francisco Martin-Martinez, Alessandra Napolitano, Zhao Qin, David Ruch, Manoj Singh, and Valerie Toniazzo. It was a great honor and privilege working with all of them.

Additionally, I would like to thank my labmates who helped me personally and professionally: Talal Al-Mulla, Graham Bratzel, Dieter Brommer, Shu-Wei Chang, Chia-Ching Chou, Steven Cranford, Baptiste Depalle, Leon Dimas, Nina Dinjaski, Davoud Ebrahimi, Kassu Gebresellasie, Tristan Giesa, Greta Gronau, Grace Gu, Kai Jin, Denvid Lau, Flavia Libonati, Diego Lopez Barreiro, Reza Mirzaeifar, Arun Nair, Seunghwa Ryu, Max Solar, Isabelle Su, Anna Tarakanova, and Tuukka Verho. I would also like to thank Marygrace Aboudou for keeping the lab in line, specifically, helping me secure the times and dates for my milestones on this journey.

I would like to thank all my good friends at MIT with whom I shared many great and wonderful experiences: Kevin Chen, Yu-Han Chen, Yu-Hsin Chen, Chia-Hao Chuang, Ting-Yun Huang, Chris Lai, Shu-Heng Shao, Tony Wu, and Sabrina Yang. I feel lucky and grateful to have had such wonderful friends. I would also like to thank my professors in Taiwan, Prof. Yeong-Bin Yang, Prof. Liang-Jenq Leu, and Prof. R. Y. Tan. It was on their recommendation that I applied to MIT to pursue my doctoral degree and start this incredible journey.

I would be remiss not to express my greatest thanks and appreciation to my family. I am greatly indebted to my parents and brother for the tremendous support and encouragement they have provided me in every stage of my life. I would be nowhere without them. They have always been there for me.

Cambridge, MA *Chun-Teh Chen*
August 18, 2016

Contents

List of Figures

List of Tables

Chapter 1

Introduction

Parts of the review presented in this chapter have been published in Marco d'Ischia, Alessandra Napolitano, Vincent Ball, Chun-Teh Chen, and Markus J. Buehler. Polydopamine and eumelanin: from structure–property relationships to a unified tailoring strategy. *Accounts of Chemical Research*, 47(12):3541–3550, 2014.

1.1 Melanin in biology

Melanin, from the Greek *melanos*, meaning black color, is a ubiquitous biological pigment, and the primary ingredient by which the skin protects deoxyribonucleic acid (DNA) in underlying tissues from ultraviolet radiation (UVR). Unlike the vast majority of natural pigments (e.g., chlorophyll and carotenoid), melanin cannot be described in terms of a well-defined structure; therefore, melanin is regarded as one of the most enigmatic pigments found in nature, and there remains a lack of consensus concerning what melanin really is [14]. There are different types of melanin in nature, including eumelanin, pheomelanin, and neuromelanin. Eumelanin is a black-to-brown insoluble photoprotective pigment. Pheomelanin is a yellow-to-reddish pigment existing in red-haired individuals, unfortunately with a high propensity to sunburn and cancer. Neuromelanin is a dark pigment that accumulates within the dopaminergic neurons of the substantia nigra, selectively degenerating in Parkinson's disease. These three types of melanin often coexist together in many species, including humans [15].

Among these three types of melanin, eumelanin is the most common and by far the most relevant from a biological and technological perspective; thus, it is the most extensively studied. Accordingly, the term "melanin" is often used to refer to "eumelanin" in non-academic articles. This thesis mainly focuses on eumelanin, including natural eumelanin, which can be isolated in large quantities from the ink sacs of the cuttlefish *sepia officinalis*, allowing in vitro studies using physical techniques [16, 17], and also synthetic eumelanin (polydopamine), which can be produced by the oxidative polymerization of dopamine (DA). The other types of melanin (i.e., pheomelanin and neuromelanin) will not be discussed in this thesis.

Eumelanin is responsible for multiple critical functions. In humans, eumelanin is the primary determinant of the color of skin, hair, and eyes. Besides its pigmentation, eumelanin is also an efficient photoprotective pigment. Eumelanin has an unusual broadband ultraviolet-visible (UV-Vis) absorption spectrum [18, 19, 20, 21], which is a result of biological evolution for protecting living organisms from intense sunlight, especially harmful UVR [22, 23]. This featureless (lacking in peaks) absorption is very uncommon amongst organic chromophores [24]. Humans whose ancestors lived for long periods in the regions of the globe near the equator, which receives more of the sun's energy, generally have more eumelanin in their skins. For example, people of African descent tend to produce more eumelanin than people of European descent. In addition, eumelanin also provides structural support for some species. For instance, eumelanin has been identified as a major constituent of the jaws of the bloodworm (*Glycera dibranchiata*).

1.2 Melanin in human skin

The human skin provides an extremely critical physical barrier against environmental influences that may affect the physiological status of the body. Three main layers can be found in the skin: the epidermis, dermis, and hypodermis [25]. The epidermis, the external, stratified epithelium devoid of blood or nerve, supplies of 5–100 μm thickness, and is composed of two primary cell populations: melanocytes and keratinocytes [25]. Melanin, including eumelanin and pheomelanin, is biosynthesized in melanocytes, which are located in the stratum basal layer. The melanin is packaged into membrane-bound organelles referred to as melanosomes and then transferred via melanocyte dendrites to surrounding keratinocytes. Keratinocytes then move outwards to distribute melanin throughout the epidermis [26]. UVR from the sun is extremely energetic and is the primary environmental factor that influences the function and survival of many cells and the main causative factor in the induction of skin tumors. The photoprotective function of melanin, especially eumelanin, is achieved by its ability to absorb UVR. Dividing cells are then protected from harmful UVR when melanin is produced and distributed properly in the skin. Ironically, given the fact that melanin helps protect cells from UVR damage, it has also been implicated in the chain of events that led to melanoma [27], a type of skin cancer that develops from melanocytes, and accounts for the vast majority of skin cancer deaths. According to the American Cancer Society, it is estimated that there will be 76,380 new cases of melanoma in the United States in 2016 and 10,130 deaths from the disease. Consequently, it is crucial to understand the biological functionality and structure–property relationships of melanin as well as its role in melanoma.

1.3 Synthetic eumelanin: polydopamine

Eumelanin has been found to have many attractive physicochemical properties including the broadband UV-Vis absorption spectrum, an intrinsic free radical character, efficient non-radiative energy dissipation, and a water-dependent, ionic-electronic hybrid conductor behavior [28]. These properties have gradually attracted the interest of scientists from diverse disciplines toward exploitation of synthetic eumelanin as a biocompatible multifunctional platform. In 2007, Messersmith, Lee, and co-workers described a universal eumelanin-like coating material called polydopamine (PDA) [1]. Their work was inspired by mussels, which have been shown to attach to virtually all types of inorganic and organic surfaces (Fig. 1-1a). According to their work, 3,4-dihydroxy-L-phenylalanine (DOPA) and lysine amino acids in mussel adhesive proteins such as Mytilus edulis foot protein-5 (Mefp-5, shown in Fig. 1-1b to 1-1d) are crucial for achieving adhesion to a broad spectrum of materials. Dopamine (DA, shown in Fig. 1-1e) has been identified as a small-molecule compound that contains both functional groups. PDA is a black insoluble material produced by the oxidative polymerization of DA without the need of any complicated instruments or harsh reaction conditions. Simple immersion of substrates in a dilute aqueous solution of DA under alkaline conditions in the presence of oxygen results in spontaneous deposition of a thin adherent PDA film (Fig. 1-1f to 1-1h). The thickness of the PDA film measured by atomic force microscopy (AFM) was found to be a function of the immersion time and reached up to 50 nm after 24 hours. X-ray photoelectron spectroscopy (XPS) analysis of 25 diverse materials coated for 3 hours or more revealed the absence of signals specific to the substrate (solid red bars in Fig. 1-1h), indicating the formation of a PDA coating of 10 nm or more in thickness. Little variation in the atomic composition of the coating was found (blue circles in Fig. 1-1h). PDA films provide protection for the underlying material against external erosion by agents like strong oxidants and acids. Furthermore, surface modification of the underlying material can be used to control the surface properties and to create additional functionalities. As a result, PDA has entered the scene of materials science in recent years, with applications that go beyond coatings [29, 30], such as solar energy [31], water purification [32], shape memory polymer [33], microrobots [34], biomedicine [35, 36, 37], and nanotechnology [30, 38].

1.4 Biosynthesis and chemical synthesis

Eumelanin biosynthesis in epidermal melanocytes involves tyrosinase-catalyzed oxidation of tyrosine or DOPA to produce DOPAquinone, which then rapidly undergoes internal cyclization to form DOPAchrome (Fig. 1-2) [2]. DOPAchrome then spontaneously decomposes to form mostly 5,6-Dihydroxyindole (DHI) and to a lesser extent 5,6-dihydroxyindole-2-carboxylic acid (DHICA). *In vivo*, this latter process is catalyzed by DOPAchrome tautomerase (Dct) [39]; thus, the availability of Dct

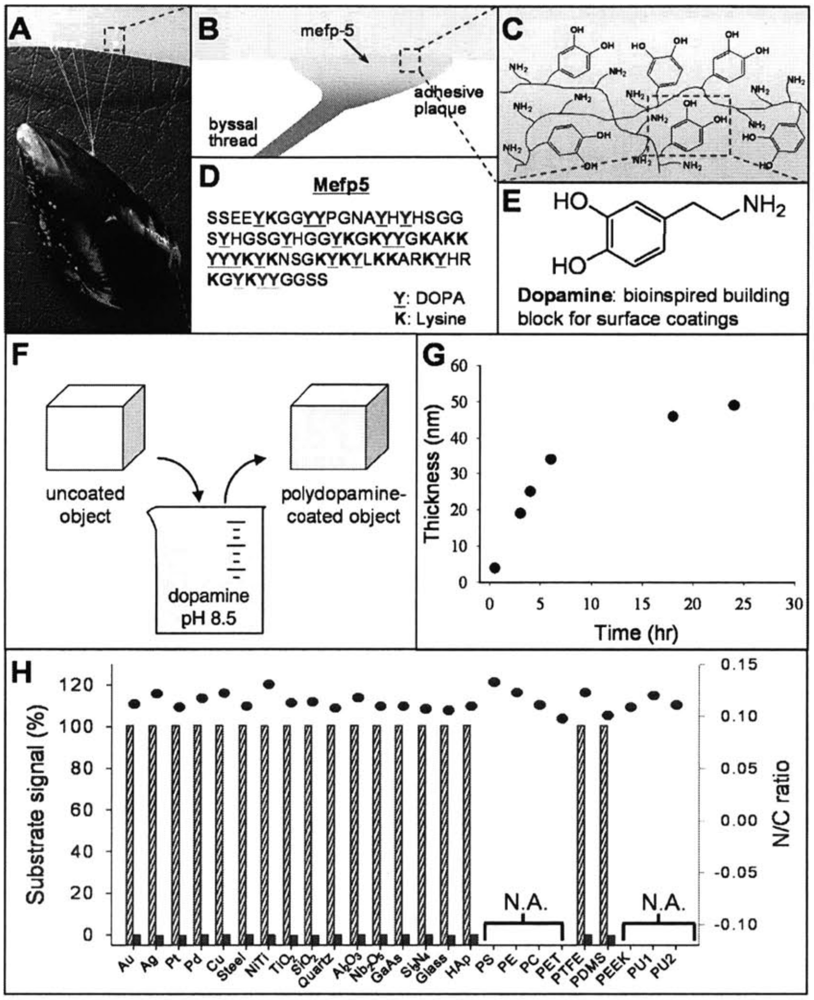

Figure 1-1: Mussel-inspired surface chemistry for multifunctional coatings. (a) Photograph of mussel attached to commercial PTFE. (b) Schematic illustration of interfacial location of Mefp-5. (c) Simplified molecular representation of characteristic amine and catechol groups. (d) Amino acid sequence of Mefp-5. (e) Dopamine contains both amine and catechol functional groups found in Mefp-5. (f) Schematic illustration of thin film deposition of polydopamine. (g) Thickness evolution of polydopamine coating on Si as measured by AFM of patterned surfaces. (h) XPS characterization of 25 different polydopamine-coated surfaces. This figure is adopted from Ref. [1]. Reprinted with permission from AAAS.

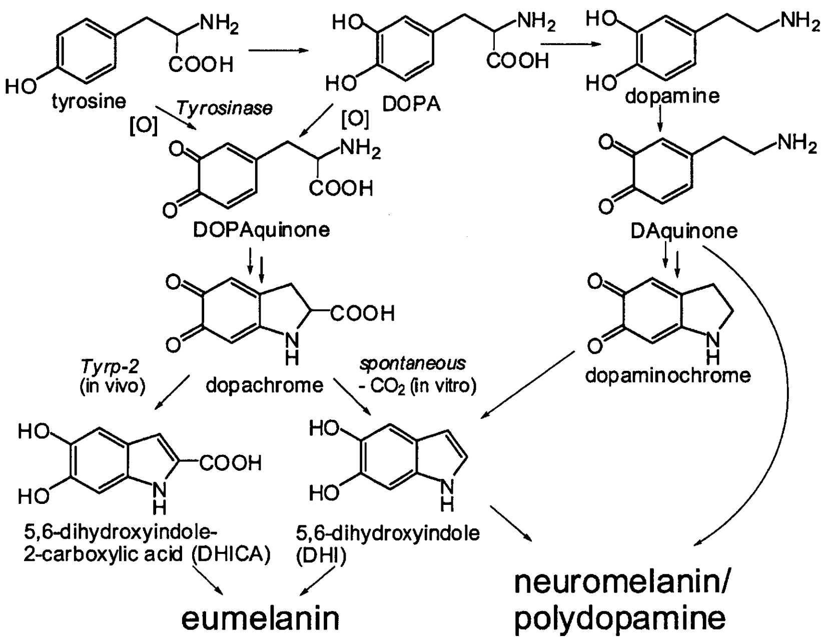

Figure 1-2: Biological and chemical synthetic pathways for eumelanin and PDA. This figure is adopted from Ref. [2]. Reprinted with permission from American Chemical Society.

determines the relative amounts of DHI and DHICA produced in the final product. Finally, oxidative polymerization of DHI and DHICA gives rise to the deposition of eumelanin. The ratio of DHI and DHICA varies widely depending on how eumelanin is synthesized. If the eumelanin under consideration contains mainly DHI, it is referred to as DHI-melanin. On the other hand, if it contains mainly DHICA, it is referred to as DHICA-melanin. With chemically induced polymerization, the isomerization reaction proceeds spontaneously with decarboxylation to give mostly DHI. Simply put, natural eumelanin usually contains a proportion of DHICA-derived units, whereas PDA contains mainly DHI-related units [14]. Analysis of this synthesis process is extremely complicated due to the highly unstable nature of the intermediates and the extremely stable insoluble nature of the final product [16]. It should be noted that a variety of synthetic eumelanin can be produced under different conditions in vitro; this thesis only focuses on a particular type of synthetic eumelanin, PDA.

1.5 Hierarchical structure

The term "structure" used in relation to eumelanin has a more complex meaning than just referring to its molecular structure. The hierarchical structure of eumelanin is thought to be made up of at least three structural levels: primary, secondary, and aggregate [2, 9, 10, 40, 41]. It is instructive to compare the hierarchical structures of eumelanin and proteins, which are macromolecules with multiple different levels of structure: primary, secondary, tertiary, and higher orders. The primary structure of a protein is its molecular structure, which is made up of 20 different standard amino acids in the polypeptide chain. These amino acids are referred to as fundamental building blocks of proteins, and can join to form chain-like structures, which are referred to as peptides or proteins, depending on the number of amino acids in the sequences. The primary structure of eumelanin is also referred to as its molecular structure, which is made up of two fundamental building blocks: DHI and DHICA. Unlike proteins, the primary structure of eumelanin is not well-defined because these fundamental building blocks can form various molecules (oligomers) with different sizes (polymerization degrees). The structural investigation of natural eumelanin is challenging due to its amorphous character, marked insolubility in almost all organic solvents, and close association with the cellular ingredients of the biological matrix.

Since eumelanin consists of more than one species of molecules and the detailed molecular structures are still controversial, the term "eumelanin molecule" is considered inappropriate to use. Accordingly, an alternative term "eumelanin protomolecule" is often used to refer to the primary level of eumelanin structure in literature, as does this thesis. Some important structural characteristics of eumelanin's primary structure have been identified in experiments. X-ray diffraction studies [6, 7] and scanning tunneling microscopy (STM) measurements [3, 42, 43] show that the size of eumelanin protomolecules is around 15–20 Å, which suggests that the tetramers and pentamers formed by covalently bonded DHI and DHICA units are the most probable molecular structures of eumelanin. Matrix-assisted laser desorption/ionization (MALDI) mass spectrometry studies [44, 45, 46, 47, 48] show that the mass of eume-

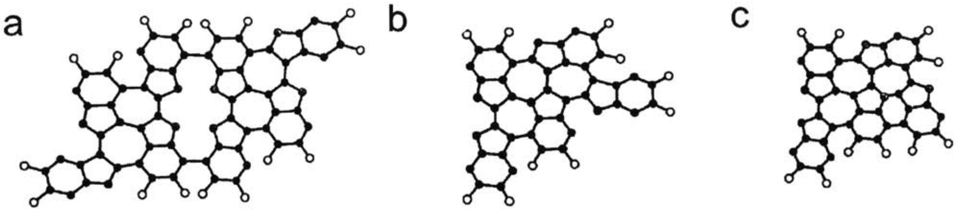

Figure 1-3: Molecular models for eumelanin. (a) Octameric model shown with random linkage of DHI units. (b) Pentameric model shown with random linkage of DHI units. (c) Variant of the model shown in (b). This figure is adopted from Ref. [3]. Reprinted with permission from Elsevier.

lanin protomolecules is within or below 600–1200 amu, while large polymeric structures are not observed, with the exception of data reported in a recent study [49]. Furthermore, most mass spectrometry investigations support the claim that tetramers and pentamers constitute the majority of eumelanin, while slightly larger structures, such as the hexamers, heptamers, and octamers, are also possible. Fig. 1-3 shows molecular models proposed by Cheng et al. [6, 7], which were created by random linkages of DHI units based on the probable sizes of eumelanin protomolecules (around 15–20 Å). Due to the small polymerization degree of eumelanin protomolecules, they are referred to as oligomers instead of polymers in this thesis. As with eumelanin, MALDI mass spectrometry analysis of PDA has indicated mixtures of low molecular weight (up to octamers) [50]. As a result, PDA is not a real polymer, and the term "polydopamine" is misleading. In addition to the low molecular weight, PDA does not arise by dehydrative condensation of DA to form a polymer, as the name suggests. Thus, the term "dopamine melanin" is more appropriate than "polydopamine" and is strongly recommended by d'Ischia et al. [2]. However, to be consistent with the studies in the field of eumelanin and PDA chemistry, the term "polydopamine" will still be used in this thesis to refer to the material synthesized by the oxidative polymerization of DA.

The secondary structure of proteins characterizes local structural conformations due to well-aligned hydrogen bonds. The two main types of secondary structures of proteins are α-helix and β-sheet. In the case of eumelanin, X-ray diffraction studies

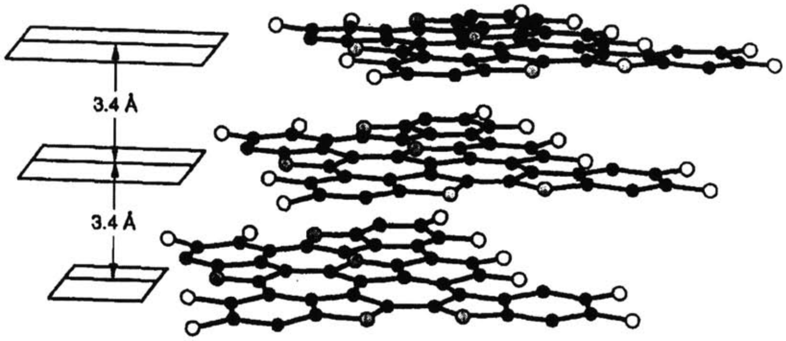

Figure 1-4: Three-dimensional molecular model of eumelanin as three stacked eumelanin protomolecules. This figure is adopted from Ref. [3]. Reprinted with permission from Elsevier.

[6, 7], STM measurements [3, 42, 43], atomic force microscopy (AFM) [17], and transmission electron microscopy (TEM) [40], suggest the existence of small near-planar oligomers that appear to be stacked together via non-covalent intermolecular interactions including van der Waals and π-π interactions to form graphite-like layered aggregates. Fig. 1-4 shows the stacking of eumelanin protomolecules, which was proposed to capture the prominent stacking feature found in experiments. This stacking structure is referred to as secondary structure of eumelanin and is one of the most important structural features of eumelanin.

The tertiary structure of a protein is a description of the complex and irregular folding of the peptide chain in three dimensions. However, the higher order structural levels of eumelanin are not well-defined. Larger particles formed by eumelanin's secondary structures are sometimes called eumelanin's aggregate structures in literature [24]. However, unlike eumelanin's secondary structure, which has the prominent stacking feature, the manner in which eumelanin's aggregate structure form from its secondary structures is unclear and will be investigated in this thesis.

1.6 Chemical disorder

Unlike other biomaterials such as DNA and proteins with well-defined and ordered structures, the structural and physicochemical properties of eumelanin-like materials imply various levels of chemical disorder. From small-scale to large-scale, these chemical disorder levels are monomeric disorder, oligomeric size disorder, molecular disorder, electronic disorder, and supramolecular disorder. Monomeric disorder relates to the variety of fundamental building blocks participating in the polymerization process. Oligomeric size disorder refers to the formation of different sizes of oligomers in the polymerization process. Molecular disorder denotes the degree of structural diversity due to the covalent bonds formed at different positions in the monomers to form oligomers. Electronic disorder relates to the distribution of redox states within oligomers. Supramolecular disorder depends on the variety of aggregates that can be generated by intermolecular interactions between oligomers. As a result, eumelanin and PDA are characterized by huge chemical disorder, and control of this disorder may allow the shaping of the physicochemical properties of these materials [2].

1.7 Motivation and objective

The progress in the field of eumelanin and PDA chemistry has been based on empirical approaches rather than a solid framework of structure–property relationships. The main reason is that there remains a lack of knowledge to link the fundamental building blocks (i.e., DHI and DHICA) of eumelanin and PDA to their macroscopic properties. The rational design and tailoring of eumelanin and PDA may greatly benefit from the current advances of *in silico* modeling approaches which yield considerable insight into their architecture and properties. Atomistic simulation methods, such as density functional theory (DFT) and molecular dynamics (MD), can serve as powerful tools to predict the physicochemical properties of materials. Provided that all atom positions and charges are known, atomistic simulation provides the possibility to understand the structure–property relationships of materials from a bottom-up approach to design and optimize materials to achieve desired properties. However, the lack of well-defined and readily available structures for eumelanin and PDA has hindered the progress of computational studies in this field. For example, only a few attempts have been made to investigate the optical properties of eumelanin from a computational perspective. These studies were limited to considering no more than three molecules [5, 51, 52, 53, 54, 55, 56], which ignoring the hierarchical structure of eumelanin, and were not able to provide a full picture of its optical properties. This thesis aims to provide the fundamental knowledge necessary to explain the physicochemical properties, such as the self-assembly mechanism, and the structural, mechanical, and optical properties, of eumelanin-like materials. In addition, this thesis also aims to provide insight into the polymerization process that leads to the actual structure of eumelanin-like materials, as well as to provide better molecular models for these materials, which is extremely critical for performing more accurate simulations.

1.8 Thesis outline

This thesis is organized into three parts. The first part, consisting of Chapters 2, 3, and 4, reproduces some of the important properties of eumelanin-like materials using large-scale simulations and explains the underpinning mechanisms that control these properties. The simulations in the first part are carried out using two different approaches: oligomer-based and monomer-based. Chapter 2 begins with an investigation of the self-assembly and structural properties of eumelanin-like materials using the simulations from the oligomer-based approach, in which the molecular models of eumelanin and PDA are adopted directly from literature. These models include a monomeric model proposed by Dreyer et al. [8], a tetrameric model proposed by Kaxiras et al. [5, 53], as well as pentameric and octameric models proposed by Cheng et al. [6, 7], which cover a broad range of the most probable molecular sizes of eumelanin-like materials. Chapters 3 and 4 continue to use the same molecular models for studying the optical and mechanical properties, respectively, of eumelanin-like materials. Chapter 3 reports a first-principles computational investigation to explain the broadband absorption feature of eumelanin-like materials, which has long been a topic of scientific debate. Chapter 4 introduces a new computational model in which the degree of polymerization can be controlled via *in silico* covalent cross-linking between DHI units. This computational model belongs to the monomer-based approach, in which the molecular models of eumelanin and PDA are generated in simulations based on the most probable cross-linking sites of DHI units.

The second part, Chapter 5, of this thesis deals with elucidating the molecular structures of eumelanin-like materials, one of the most challenging issues in this field. Chapter 5 presents a set of modeling methods to generate and evaluate probable molecular structures of eumelanin and PDA systematically, explains some important structural features, and provides new molecular models for more accurate modeling of these materials. The third part, Chapter 6, presents a study of the mechanical properties of graphene oxide (GO) and PDA nanocomposites, one of the most popular applications of PDA, focusing on their mechanical strength, and shrinking mechanism during dehydration.

The last chapter of this thesis, Chapter 7, summarizes the key findings and their significances, discusses the results, and proposes possible future directions.

1.9 Methodology

1.9.1 Molecular dynamics

Molecular dynamics (MD) simulation is a powerful tool for applications in various research fields including physics, chemistry, biology, and engineering. The evolution over time of a set of interacting atoms is followed by integrating their equations of motion given by Newton's second law:

$$m_i \frac{\mathrm{d}^2 r_i}{\mathrm{d}t^2} = -\frac{\mathrm{d}U(r_i)}{\mathrm{d}r_i} \tag{1.1}$$

where m_i is the mass of atom i, r_i is the position vector of atom i, and U is the potential energy. The equations of motion are ordinary differential equations, which can be solved numerically. There are many integration algorithms to solve ordinary differential equations; however, it is better to use algorithms specifically suited for systems obeying Newton's equations of motion such as the Verlet algorithm. The motion (atomic positions and velocities) is calculated and recorded, and other quantities are derived from it. The key to MD simulations is the determination of the potential energy, U. This quantity is determined from a prescribed force field. Reactive force fields such as ReaxFF are capable of capturing covalent bond chemistry; other non-reactive force fields can only simulate non-covalent interactions. The total potential energy of a system can be expressed by the superposition of valence, cross-term, and non-bonded interactions shown below:

$$E_{total} = E_{valence} + E_{crossterm} + E_{nonbond} \tag{1.2}$$

The valence interactions consist of bond stretching, bond angle bending, dihedral angle torsion, and out-of-plane (oop) angle torsion terms shown below:

$$E_{valence} = E_{bond} + E_{angle} + E_{torsion} + E_{oop} \tag{1.3}$$

The geometry definitions of bond length, bond angle, dihedral angle, and out-of-plane angle are shown in Fig. 1-5. The non-bonded interactions consist of van der Waals, electrostatic, and (in some force fields) hydrogen bond terms shown below:

$$E_{nonbond} = E_{vdW} + E_{coulomb} + E_{hbond} \tag{1.4}$$

The cross-terms represent coupling between deformations of internal coordinates. These terms are sometimes required to accurately reproduce experimental vibrational frequencies and other dynamic properties of molecules.

1.9.2 Consistent valence force field

In this thesis, the classical MD simulations in Chapters 2, 3, 4, and 5, are performed using the large-scale atomic/molecular massively parallel simulator (LAMMPS) [57] with the consistent valence force field (CVFF) [58, 59]. CVFF is a generalized valence force field, which was developed to reproduce the properties of small organic crystals and gas phase structures. It also handles peptides, proteins, and a wide range of

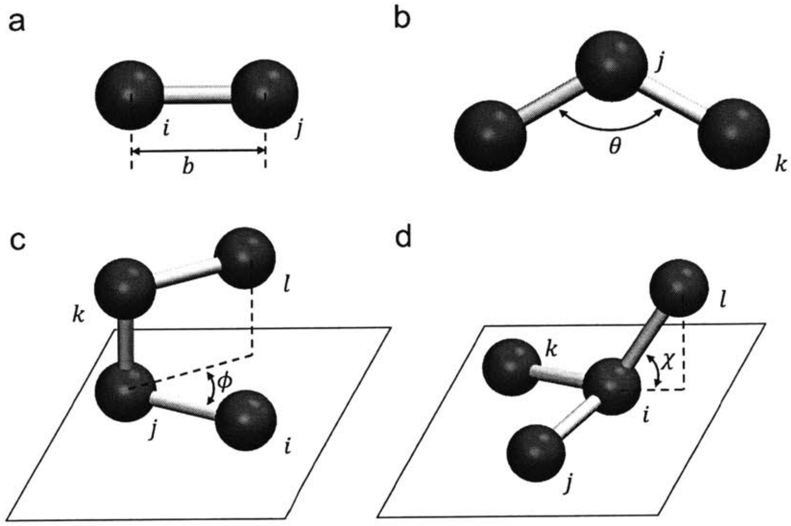

Figure 1-5: Schematic diagrams of valence interactions. (a) bond, (b) bond angle, (c) dihedral angle, and (d) out-of-plane angle.

organic systems. CVFF has been widely applied in modeling organic molecules with aromatic rings such as benzene and caffeine co-crystals [60]. At the same time, efforts have been made to parameterize CVFF for inorganic materials, including silica as well as the interface between epoxy and silica [61]. The analytic form of the total potential energy expression used in CVFF is shown below:

$$\begin{aligned} E_{total} = &\sum_{b} K_b \left(b - b_0\right)^2 + \sum_{\theta} K_\theta \left(\theta - \theta_0\right)^2 + \sum_{\phi} K_\phi \left[1 + d\cos(n\phi)\right] \\ &+ \sum_{\chi} K_\chi \left[1 + d\cos(m\phi)\right] + \sum 4\epsilon_{ij} \left[\left(\frac{\sigma_{ij}}{r_{ij}}\right)^{12} - \left(\frac{\sigma_{ij}}{r_{ij}}\right)^{6}\right] + \sum \frac{q_i q_j}{\epsilon r_{ij}} \end{aligned} \tag{1.5}$$

where K_b, K_θ, K_ϕ, and K_χ are stiffness constants. The terms b_0 and θ_0 are the equilibrium bond length and angle, respectively. The terms b, θ, ϕ and χ are bond length, bond angle, dihedral angle, and out-of-plane angle, respectively. The term r_{ij} is the distance between the i-th and j-th atoms with chagres q_i and q_j, respectively. The term ϵ_{ij} is the depth of the Lennard-Jones potential well and σ_{ij} is the finite distance at which the inter-particle potential is zero between the i-th and j-th atoms. The term ϵ is the dielectric constant for Coulombic interactions, which is used to reduce the strength of the interactions.

Terms 1, 2, 3, and 4 in Eq. 1.5 represent the energy of deformation of bond lengths, bond angles, torsion angles, and out-of-plane angles, respectively. Note that these four terms are all in the harmonic form. A more complex term given by Morse potential can be used for the bond-stretching term in CVFF. However, the Morse form is computationally more expensive than the harmonic form (Term 1). In this thesis, all MD systems are equilibrated at room temperature (300 K) before studying their properties; thus, the bond lengths in the systems are near their equilibrium lengths. Since the difference between the harmonic form and Morse form when a bond is close to its equilibrium length is negligible, the more accurate, yet more expensive, Morse potential is not used in this thesis. In addition, the dynamic properties of molecules are not a focus; thus the cross-terms in CVFF are ignored in the simulations to increase the efficiency. The last two terms (Terms 5 and 6) describe the non-bonded interactions. Term 5 represents the van der Waals interaction with a Lennard-Jones potential. Term 6 is the Coulombic representation of electrostatic interactions. In CVFF, hydrogen bonds are a natural consequence of the standard van der Waals and electrostatic parameters. To input the correct parameters for CVFF, the molecular models of eumelanin and PDA used in Chapters 2, 3, 4, and 5 are created in Materials Studio [62], where the atom types for CVFF can be correctly assigned. The bond increment section of the force field file for CVFF has been expanded so that partial charges can be determined. The connectivity of the molecules is obtained from Materials Studio and converted to data files for LAMMPS.

1.9.3 Reactive force field

In this thesis, the reactive MD simulations in Chapter 6 are performed using LAMMPS with a reactive force field, ReaxFF, developed by van Duin, Goddard, and co-workers [4]. Non-reactive force fields such as CHARMM (Chemistry at HARvard Macromolecular Mechanics) and CVFF are only capable of describing bond stretching around the equilibrium state, and cannot describe bond dissociation and formation. To get a smooth transition from non-bonded to single, double and triple bonded systems, a proper description of bond length and bond order relationship is required. ReaxFF can capture the change of bonds by considering bond-orders that are estimated by the relative distances between atoms. The bond-order information enables simulations to consider quantum chemical states of atoms to form or dissociate bonds in the systems. Fig. 1-6 shows a concept of the bond-order of ReaxFF for hydrocarbon systems [4]. Based on the bond-order dependency, the potential between carbon atoms changes and goes to zero when it reaches the defined breaking points. Unlike non-reactive force fields in which the bond orders are fixed and defined using multiple atom types in the systems, ReaxFF updates its bond orders every iteration. All connectivity-dependent interactions are made bond-order dependent, insuring that their energy contributions disappear upon bond dissociation. Non-bonded interactions are calculated between every atom pair, irrespective of connectivity. Excessive close-range non-bonded interactions are avoided by shielding. ReaxFF uses a geometry-dependent charge calculation scheme that accounts for polarization effects. ReaxFF has been shown to provide an accurate description of hydrocarbons and water [4], and allows for an explicit consideration of long-range and non-bonded interactions (i.e., van der Waals, Coulombic, and hydrogen bonding interactions), making it particularly suitable for simulations of graphene oxide (GO) systems [63, 64]. In Chapter 6, ReaxFF is adopted for studying the mechanical properties of GO and GO–PDA nanocomposites.

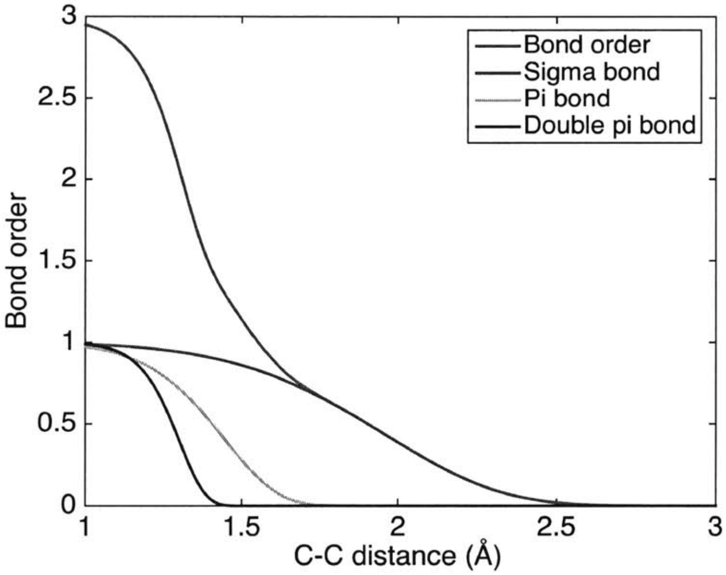

Figure 1-6: Interatomic distance dependency of carbon-carbon bond order for ReaxFF. This figure is modified from Ref. [4].

Chapter 2

Self-assembly and structural properties of eumelanin

This chapter contains the content regarding the self-assembly and structural properties of eumelanin in the publications:

1. Chun-Teh Chen, Vincent Ball, Jose Joaquim de Almeida Gracio, Manoj Kumar Singh, Valerie Toniazzo, David Ruch, and Markus J. Buehler. Self-assembly of tetramers of 5, 6-dihydroxyindole explains the primary physical properties of eumelanin: Experiment, simulation, and design. *ACS Nano*, 7(2):1524–1532, 2013.
2. Chun-Teh Chen, Chern Chuang, Jianshu Cao, Vincent Ball, David Ruch, and Markus J. Buehler. Excitonic effects from geometric order and disorder explain broadband optical absorption in eumelanin. *Nature Communications*, 5, 2014.

2.1 Introduction

Essential structural characteristics that provide valuable insights into the self-assembly and structural properties of eumelanin have been found in experiments, albeit the detailed structure of eumelanin including the molecular and higher level structures are still unclear. The X-ray scattering experiments implemented by Cheng et al. [6, 7] and the STM experiments performed by Zajac et al. [3], suggest that eumelanin is a heterogeneous material consisting of stacked oligomers. The increasingly more experimental evidence is in favor of the heterogeneous model [65, 66]. Although some studies have proposed molecular models for eumelanin based on experimental observations, they have not yet included any large-scale computational investigations (e.g., MD simulations) to verify if the proposed eumelanin molecular models can reproduce the self-assembly and structural properties of eumelanin.

Recently, Kaxiras et al. [5] proposed a new, detailed molecular model for eumelanin, based on a tetrameric molecular structure consisting of four monomer units, in arrangements that contain an inner porphyrin ring. In their subsequent work, Meng and Karixas [53] performed DFT calculations to establish a transition to higher level aggregates from a single tetramer. They found that two such tetramers do not only associate in a quasi-parallel arrangement with an interlayer spacing of around 3–4 Å via π-stacking and van der Waals interaction, but also bind in a covalent manner via interlayer C–C bonds. However, these studies restricted the systems to only two tetramers due to the computational limitations of DFT calculations. Consequently, these studies could not provide a full understanding of the self-assembly and structural properties of eumelanin. It is of great interest to consider larger systems to have more physical information about the formation of eumelanin. Therefore it is mandatory to go from the two-tetramer systems investigated by Meng and Kaxiras [53] to somewhat larger and more realistic systems made up of some hundreds of eumelanin protomolecules.

The objective of this chapter is to study the self-assembly and structural properties of eumelanin by using large-scale MD simulations. Since there is still no agreement on the molecular structures of eumelanin, a variety of eumelanin molecular models supported by experimental or theoretical studies are considered. The simulated aggregate structures are compared with synthetic eumelanin (PDA) as characterized using high-resolution TEM.

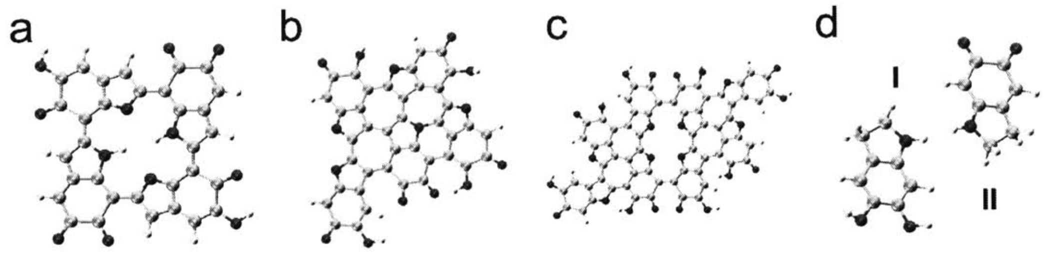

Figure 2-1: Molecular models of eumelanin. (a) Tetrameric model proposed by Kaxiras et al. [5]. (b) Pentameric and (c) octameric models proposed by Cheng et al. [6, 7]. (d) Monomeric model proposed by Dreyer et al. [8]. The two monomers in the monomeric model are called M1 and M2 here. This figure is adopted from Ref. [9]. Reprinted with permission from Nature Publishing Group.

2.2 Methods

2.2.1 Eumelanin molecular models

Eumelanin protomolecules comprise DHI and DHICA, as well as their derived redox forms. These redox forms include hydroquinone (HQ), indolequinone (IQ) and its tautomers (QIs) including quinone-methide (MQ) and quinone-imine (NQ). According to the DFT study by Kaxiras et al. [5], there are 21 possible arrangements of four individual monomer units (e.g., HQ, IQ, MQ, and NQ) in a tetrameric model, if considering the two QI forms (e.g., MQ and NQ) as one type. However, only eight of them that contain two or three QI units have large positive formation energy. As a result, these eight tetramers are considered the dominant tetramers. In this chapter, the most stable tetramer among the eight dominant tetramers, the IQ-MQ-IQ-MQ tetramer containing two IQ and two MQ units, is adopted as one of the eumelanin molecular models (Fig. 2-1a) in the simulations. In addition to this tetrameric model, other eumelanin molecular models proposed in the literature are also considered. These molecular models include a pentameric (Fig. 2-1b) and octameric (Fig. 2-1c) models proposed by Cheng et al. [6, 7] as well as a monomeric model (Fig. 2-1d) proposed by Dreyer et al. [8]. These four different molecular models cover a broad range of the most probable molecular sizes of eumelanin.

2.2.2 Atomistic modeling and equilibration

Full atomistic MD simulations are implemented using LAMMPS [57] with CVFF [58, 59]. The comparison between DFT calculations and MD simulations with CVFF is discussed in Appendix B.1. The charge is taken into account in the simulations. The total charge of the four eumelanin molecular models is zero (electroneutral). Energy minimization using the conjugate gradient (CG) algorithm is implemented before MD simulations. The nonbonding interactions (12/6 Lennard-Jones and Coulombic interactions) are computed using a neighbor list cutoff of 12 Å. Periodic boundary conditions (PBCs) are applied.

Four large-scale systems are created. Three of them consist of 729 molecules using the tetrameric, pentameric, and octameric models. The remaining one consists of 1,458 (729-set) molecules using the monomeric model. The initial distance between two molecules in the systems is set to larger than 30 Å to ensure that there are no intermolecular interactions in the initial configuration. After energy minimization, the systems are simulated with the NPT ensemble at a constant temperature of 1,000 K and pressure of 1.013 bar for 2 ns to ensure sufficient exploration of the configurations of the final aggregates. The high temperature in the simulations allows the molecules to reach more stable configurations much faster than simulating at room temperature (300 K). However, there are some vacancies in the systems after the previous NPT ensemble, and these vacancies might remain in the systems for a long time even after the temperature is reduced to 300 K. In order to remove these vacancies, the systems are then simulated with the NPT ensemble at a constant temperature of 300 K and pressure of 10,130 bar for another 2 ns. The high pressure in the simulations compresses the systems and removes these vacancies. To study the self-assembly and structural properties at room temperature (300 K) and standard atmospheric pressure (1.013 bar), the systems are then simulated with the NPT ensemble at a constant temperature of 300 K and pressure of 1.013 bar for another 2 ns in the final step.

2.3 Results and discussion

2.3.1 Small-scale MD simulations

One of the most important structural characteristics of eumelanin is that the eumelanin protomolecules tend to stack together in planar graphitic arrangements. To calculate the equilibrium interlayer spacing between two stacked eumelanin protomolecules, a simple system containing only two tetramers is investigated. The initial distance between these two tetramers is adjusted to 1.8 Å. After energy minimization, the interlayer spacing is increased from 1.8 Å to 3.3 Å. This spacing is very close to previous experimental and computational studies [53]. To start the investigation on the self-assembly mechanism, a small system containing four tetramers is investigated. After energy minimization, the system is simulated with the NVT ensemble at a constant temperature of 300 K. The snapshots of the system during the simulation are shown in Fig. 2-2. In the figure, these four tetramers are separated from each other in the initial configuration (0 ps) and are stacked together to form a layered structure, which is also referred to as secondary structure, after 6 ps. The simulation shows that forming secondary structures is thermodynamically more favorable compared to other configurations.

Other two small systems are created to study the size distribution of secondary structures. One of them contains eight tetramers and the other contain twelve tetramers. After energy minimization, the systems are simulated with the NVT ensemble at a constant temperature of 300 K for 100 ps, and the snapshots of the systems after the simulations are shown in Fig. 2-3. One secondary structure can be identified in the snapshot of the system containing eight tetramers shown in Fig. 2-3a. These eight tetramers all stacked together to form a secondary structure. In the snapshot of the system containing twelve tetramers shown in Fig. 2-3b, three secondary structures can be identified, and each one of them contains four tetramers. These three secondary structures also attract to each other via nonbonding interactions to form an aggregate structure. Note that the number of secondary structures that will form depend on the initial configuration (positions and velocities) of the molecules. The

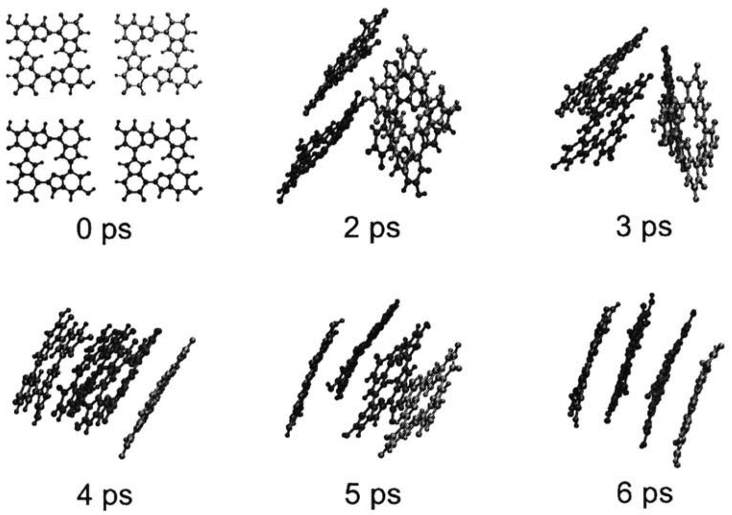

Figure 2-2: Snapshots of eumelanin self-assembly obtained from MD simulations.

simulation results do not imply that eight tetramers will form one secondary structure, and twelve tetramers will form three secondary structures. With a different initial configuration or different simulation setup, a system containing eight tetramers could form two secondary structures and a system containing twelve tetramers could form only one secondary structure. In most cases, a large secondary structure is less stable than two or more smaller secondary structures aggregating together. The criteria used to define secondary structures is described in Appendix A.1.

2.3.2 Large-scale MD simulations

The investigation of eumelanin aggregate structure is then expanded to the large-scale systems consisting of 729 oligomers (i.e., tetramers, pentamers, and octamers) or 1,458 (729-set) monomers. The snapshots of the large-scale systems after the MD equilibrations (see Methods section for details) are shown in Fig. 2-4 [9]. The snapshots obtained from the simulations using the oligomeric models (Fig. 2-4a, 2-4b, and 2-4c) reveal simulated aggregate structures similar to those observed experimentally [10, 40]. Fig. 2-5 [10] shows a TEM micrograph of synthetic eumelanin (PDA). In both the simulated and experimentally obtained aggregate structures, some layered

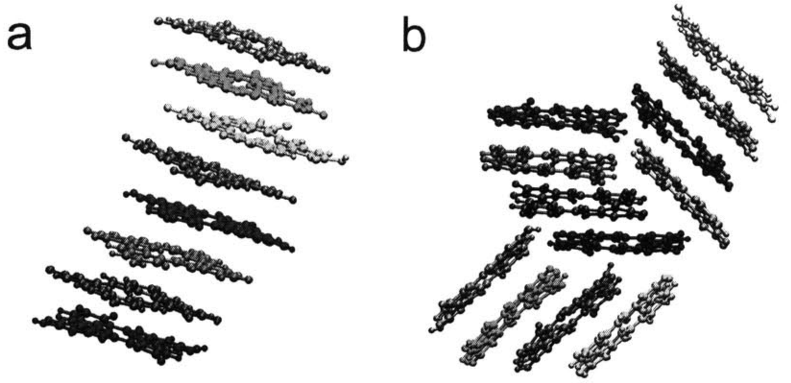

Figure 2-3: Snapshots of eumelanin aggregate structures obtained from MD simulations. (a) One secondary structure contains eight tetramers. (b) Three secondary structures contain a total of twelve tetramers.

structures are identified. The distance between stacked eumelanin protomolecules is around 3.3 Å on average, which is very close to the interlayer spacing of graphite [67]. The presence of ordered cylinders of aggregates randomly oriented trough the cluster was also found in the TEM micrographs reported by Watt et al. [40]. However, no such secondary structures are found in the simulation using the monomeric model (Fig. 2-4d). The result shows that the monomeric model is failed at reproducing the structural properties of eumelanin.

In the large-scale simulations, the size distributions of the secondary structures extend to a dozen of eumelanin protomolecules (Fig. 2-6). These eumelanin protomolecules tend to adopt random-like orientations (Appendix Fig. B-2) and stack together to form secondary structures in different sizes. There are only 29 tetramers (4.0%), 66 pentamers (9.3%), and 129 octamers (17.7%) among 729, not forming secondary structures. For the monomeric model, there are 437 monomers (30%) among 1,458 (729-set) not forming secondary structures. The ratio is higher compared to the oligomeric models, due to its small molecular size.

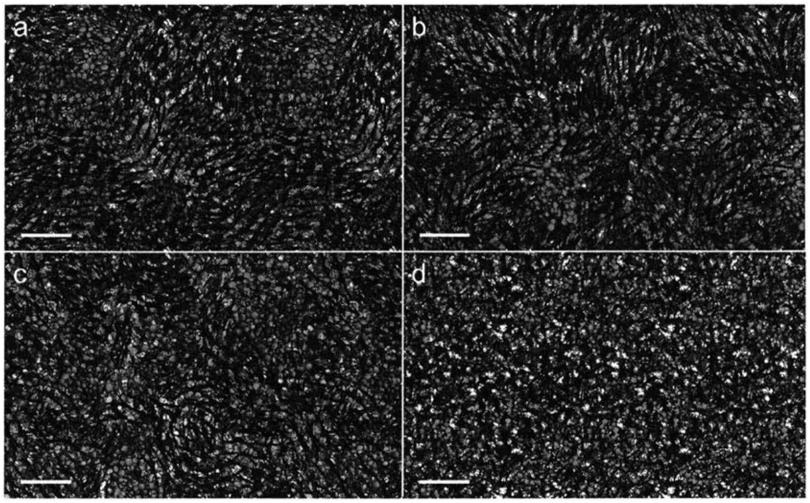

Figure 2-4: Snapshots of large-scale systems obtained from MD simulations. Aggregate structure of (a) tetrameric, (b) pentameric, (c) octameric, and (d) monomeric model, respectively. The scale bars represent a length of 2 nm. This figure is adopted from Ref. [9]. Reprinted with permission from Nature Publishing Group.

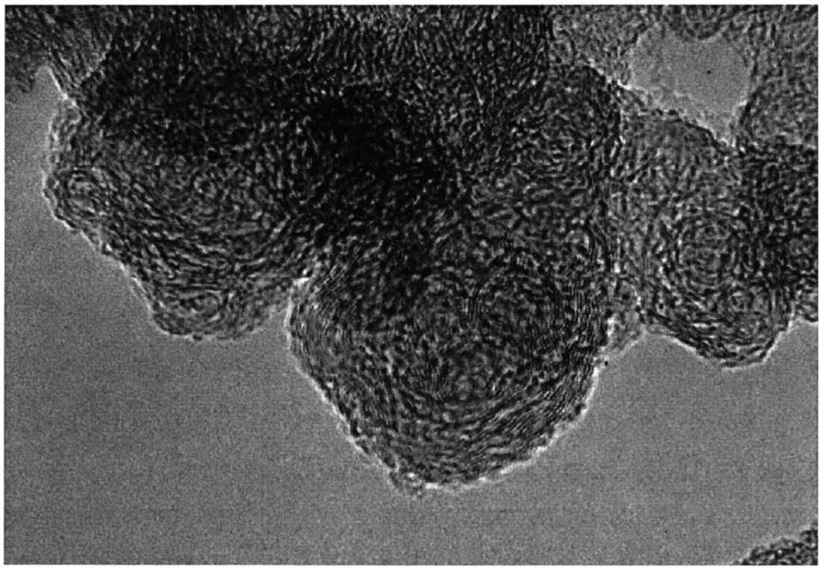

Figure 2-5: TEM micrograph of synthetic eumelanin (PDA). The scale bar represents a length of 10 nm. This figure is adopted from Ref. [10]. Reprinted with permission from American Chemical Society.

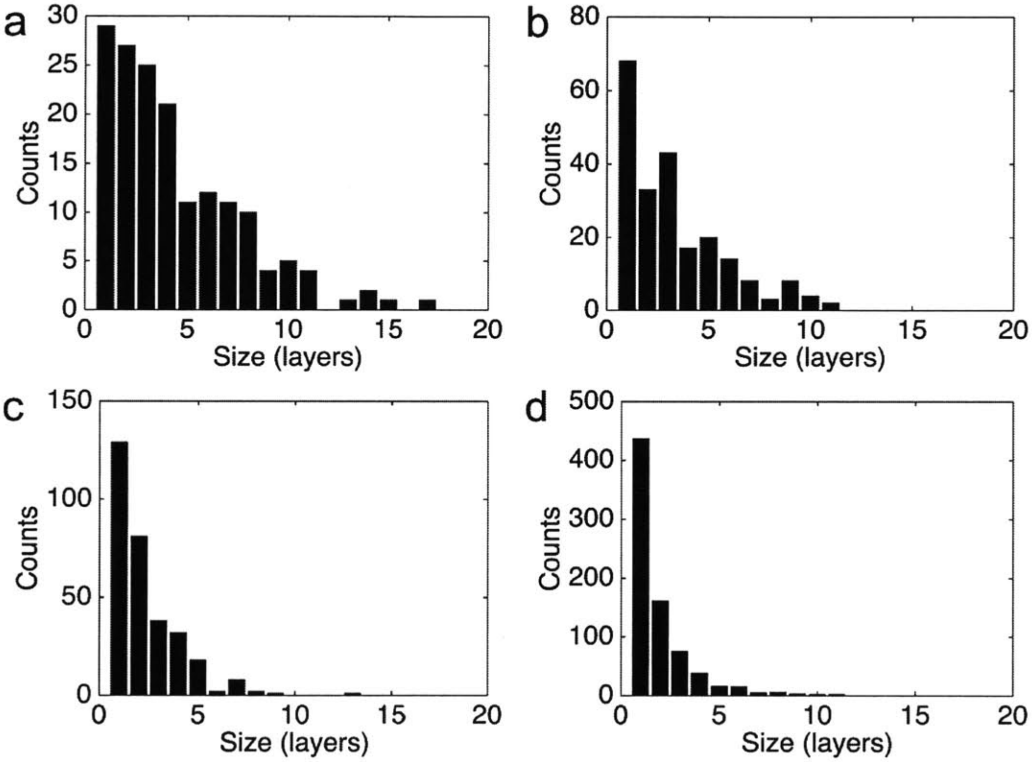

Figure 2-6: Secondary structure distributions of eumelanin protomolecules in aggregates made up of n molecules in large-scale systems consisting of (a) 729 tetramers, (b) 729 pentamers, (c) 729 octamers, and (d) 1,458 (729-set) monomers, respectively. This figure is adopted from Ref. [9]. Reprinted with permission from Nature Publishing Group.

2.4 Conclusions

This chapter confirms the hypothesis that eumelanin is a heterogeneous material consisting of stacked eumelanin protomolecules (oligomers) via self-assembly. The simulation results show that making the assumption that eumelanin protomolecules are planar oligomers is sufficient to reproduce the structural properties of eumelanin. The simulation results give additional proof that the "stacked oligomer" model can explain the self-assembly and structural properties of eumelanin. For the first time, the gap between primary, secondary, and aggregate structures of eumelanin is bridged to describe the formation of eumelanin-like materials containing a reasonable number (hundreds) of protomolecules. The simulation results imply that the random-like arrangement (entropic contribution) with stacked eumelanin protomolecules (enthalpic contribution) is thermodynamically more favorable than completely ordered arrangements.

Chapter 3

Optical properties of eumelanin

This chapter contains the content regarding the optical properties of eumelanin in the publication, Chun-Teh Chen, Chern Chuang, Jianshu Cao, Vincent Ball, David Ruch, and Markus J. Buehler. Excitonic effects from geometric order and disorder explain broadband optical absorption in eumelanin. *Nature Communications*, 5, 2014.

3.1 Introduction

Eumelanin is the most common biological melanin and is responsible for multiple critical functions in living organisms. In humans, eumelanin is the primary determinant of the color of skin, hair, and eyes. Besides its pigmentation, eumelanin is also an efficient photoprotective pigment. The broadband absorption spectrum of eumelanin [18, 19, 20, 21] is a result of biological evolution to protect living organisms from intense sunlight [22, 23]. Any gaps in the spectrum would leave living organisms vulnerable to these specific wavelengths of sunlight. It has been known that UVA and UVB radiation are major environmental factors that influence the functions and survival of many cell types. Eumelanin dissipates approximately 90% of the UV energy as heat in a nanosecond or even faster time scale [18, 68]. In addition, studies have demonstrated that visible light can also induce cellular dysfunction and cell death, especially the blue region (400–500 nm), since it has relatively high energies and longer penetration depth [69]. The absorption spectrum of eumelanin must monotonically increase toward the higher-energy end to provide an efficient photoprotective function. To synthesize biomimetic materials with similar optical properties as eumelanin for industrial or medical applications, a thorough understanding of the intrinsic structural factors and precise mechanisms that give rise to the broadband absorption feature is critical. However, despite significant experimental and theoretical efforts over the past several decades, the origin of the broadband absorption spectrum is still a topic of scientific debate, and how the molecular and aggregate structures of eumelanin relate to its overall optical properties is not well-understood [26, 28].

The chemical disorder model is a widely accepted model to explain the broadband absorption spectrum of eumelanin [20, 55, 70]. Accordingly, eumelanin consists of many chemically distinct species and its broadband absorption spectrum is a result of averaging over the spectra of these species. The sharp peaks in the spectra due to DHI and its oligomers could be eliminated after this process [5, 20, 52, 54, 55, 56, 70]. Even though the chemical disorder model combined with the superposition principle seems able to reproduce broadband absorption spectra, it is still insufficient to provide a full explanation of the optical properties of eumelanin. First, experiments have suggested that eumelanin is made up of stacked oligomers with an interlayer distance of around 3–4 Å [10, 40]. As a result, it is expected that when molecules are brought this close, the electron density and spectrum will change. Studies have shown that the interactions among eumelanin protomolecules are strong enough to affect the spectrum significantly, and the superposition principle apparently does not hold [54]. Second, the molecular structures of eumelanin are still poorly understood, and so are the ratios of distinct species. It is less convincing that over-fitting does not occur when averaging over chemical inhomogeneity. Third, the chemical disorder model requires many different species of eumelanin protomolecules to reproduce the broadband absorption feature. However, these families of molecules have not been shown to reproduce other important properties of eumelanin, such as its structural and mechanical properties. Last but not least, the chemical disorder model is unable to explain why the absorption spectrum of eumelanin monotonically increases toward the higher-energy end, which is one of the most important spectroscopic features of eumelanin.

There have been several attempts to calculate the absorption spectrum of eumelanin. However, due to computational limitations, the system sizes were limited to no more than three molecules [5, 51, 52, 53, 54, 55, 56]. Such a setup is unable to capture the full picture of the optical properties of eumelanin since it neglects the geometric disorder characteristic. It is necessary to go beyond these studies and to consider more realistic systems, which introduce the effect of geometric disorder through ensemble sampling. This chapter adopts the four different eumelanin molecular models (Fig. 3-1a to 3-1d) discussed in Chapter 2 to study their optical properties. In addition, other molecular models proposed and experimentally validated by Panzella et al. [12] and Arzillo et al. [13] are also considered. The absorption spectra of small-scale systems made of these models are obtained through conventional quantum chemical calculations, and the Frenkel exciton model is used to calculate the absorption spectra of large-scale systems.

3.2 Methods

3.2.1 ZINDO/S method

The molecular models of eumelanin are first optimized using DFT calculations implemented in an *ab initio* quantum chemistry program package, ORCA [71], with the Becke three-parameter Lee-Yang-Parr functional (B3LYP) [72, 73] and the Ahlrichs-VDZ polarized basis set [74]. These optimized molecular structures are then used as the inputs of the Zerner's Intermediate Neglect of Differential Overlap (ZINDO/S) method implemented in Gaussian 09 [75], to calculate the absorption spectra in the gas phase. A Lorentzian broadening with Full Width at Half Maximum (FWHM) of 7.5 nm is applied to the raw results to generate the simulated absorption spectra. The raw results are used as the inputs of the Frenkel exciton model to calculate the absorption spectra of the large-scale systems.

3.2.2 Frenkel exciton model

To include the excitonic effect among eumelanin protomolecules, the standard Frenkel exciton model is adopted [76]. The Frenkel exciton model takes into account only the singly excited manifolds of the molecules of interest, which is appropriate for this study. Both the spectral broadening effects originating from static (inhomogeneous) and dynamical (homogeneous) disorders are ignored for simplicity. The Hamiltonian is shown below:

$$H = \sum_{m=1}^{N_M} \sum_{i=1}^{N_S} \omega_{m,i} \left| m,i \right\rangle \left\langle m,i \right| + \sum_{m>n=1}^{N_M} \sum_{i,j=1}^{N_S} J\left(m,i;n,j\right) \left| m,i \right\rangle \left\langle n,j \right| \tag{3.1}$$

where $\omega_{m,i}$ is the transition energy of the i-th transition of molecule m. Since chemical disorder is not considered throughout the system, $\omega_{m,i} = \omega_i$, that is, the transition energies are independent of the site label. The term $\left|m,i\right\rangle$ denotes the state in which the i-th electronic transition of the m-th molecule is excited, while all other molecules in the system are in their ground state. The terms N_M and N_S are the size of the aggregate structure and number of monomeric transitions included in the calculation, respectively. Note that the summations over m and n in the second term exclude the case where $m = n$; in other words, there is no coupling between transitions within the same molecule. The term $J\left(m,i;n,j\right)$ specifies the coupling between the i-th transition of the m-th molecule and the j-th transition of the n-th molecule. The atomic transition charge distribution method [77, 78] is adopted and shown below:

$$J\left(m,i;n,j\right) = \sum_{k=1}^{M_m} \sum_{l=1}^{M_n} \frac{q_k^{(i)} q_l^{(j)}}{r_{kl}} \left(1 - \delta_{mn}\right) \tag{3.2}$$

where $q_k^{(i)}$ is the transition electron density between the ground state and i-th excited state on the k-th atom, and r_{kl} is the separation between corresponding atoms, taken from the results of the MD simulations described before. The summations run over all the atoms of molecules m (M_m) and n (M_n), and the linear absorption spectrum of the system is obtained by numerically diagonalizing the Hamiltonian. The terms in the parentheses insure that the interaction exists only between different molecules. In this chapter, 48 electronic transitions of the molecules with the largest oscillator strengths are considered (i.e., $N_s = 48$) in the calculations. The absorption spectra show no noticeable difference by either increasing the system size (N_m) or the number of gas phase transitions included (N_s). The Frenkel exciton model has been validated to be accurate in calculating the spectra of eumelanin protomolecules since it can predict similar absorption spectra as those obtained using the ZINDO/S method (see Appendix B.3 for details).

3.3 Results and discussion

3.3.1 Absorption spectra of small-scale systems

The four different eumelanin molecular models have distinct optical characteristics in the gas phase, in line with the chemical disorder model. The individual molecular structures are shown in Fig. 3-1a to 3-1d. The investigation begins by studying the absorption spectra of small-scale systems (no more than three oligomers or six monomers in a system). The geometry of a single molecule of each molecular model in the gas phase is optimized using DFT calculations. However, it is computationally demanding to perform DFT calculations (see Methods section for details) on the systems with more than one molecule, and the proper account of van der Waals interactions in DFT is still an open subject of study. MD simulations are implemented to find the equilibrium structures of the systems that contain more than one molecule. The equilibrium structures of the small-scale systems are shown in Fig. 3-1e to 3-1l. Based on these structures, the absorption spectra of the small-scale systems calculated using the ZINDO/S method are shown in Fig. 3-2. Several sharp peaks in the spectra are observed, which are expected results for small organic molecules. These results clearly show that the absorption spectra of eumelanin protomolecules change as a function of aggregate size. Similar results for different eumelanin molecular models (see Appendix B.4 for details) and different redox forms (see Appendix B.5 for details) are also found. These results indicate the inadequacy of calculating the absorption spectrum of eumelanin using the superposition principle since it simply ignores the excitonic couplings among the eumelanin chromophores.

3.3.2 Absorption spectra of large-scale systems

The large-scale systems consist of either 729 oligomers (i.e., tetramers, pentamers, and octamers) or 1,458 (729-set) monomers, which are adopted from Chapter 2. Based on the simulated spectra of the small-scale systems, one expects that the spectra will continue to change as a function of aggregate size. However, calculating the spectra of systems that contain more than a few eumelanin protomolecules is beyond the capability of quantum chemical methods. Consequently, the spectra of the large-scale systems obtained from MD equilibrations (see Chapter 2 for details) are calculated with a proper account of the excitonic couplings based on the Frenkel exciton model [76]. The basis of the Frenkel exciton model is spanned by the singly excited states of the constituent eumelanin protomolecules in the gas phase, calculated with the ZINDO/S method. In addition, for an accurate estimation of the excitonic interactions, the atomic transition charge distribution method is adopted instead of the more traditional point dipole method. This choice is necessary since the interlayer spacing between eumelanin protomolecules observed in the MD simulations is approximately 3–4 Å (see Chapter 2 for details), even smaller than the typical dimension of the eumelanin protomolecules. The point dipole method is known to give inaccurate estimations of the excitonic couplings to the extent of an order of magnitude in such circumstances [79, 80, 81].

The absorption spectra of the large-scale systems calculated using the Frenkel exciton model are shown in Fig. 3-3. It appears that the simulated spectra of the aggregate structures are drastically different from those of the oligomers in the gas phase. For the oligomeric models (Fig. 3-3a to 3-3c), the simulated spectra appear to have characteristics similar to the experimental results [18, 19, 20, 21], namely being smooth and monotonically increasing toward the higher-energy end. However,

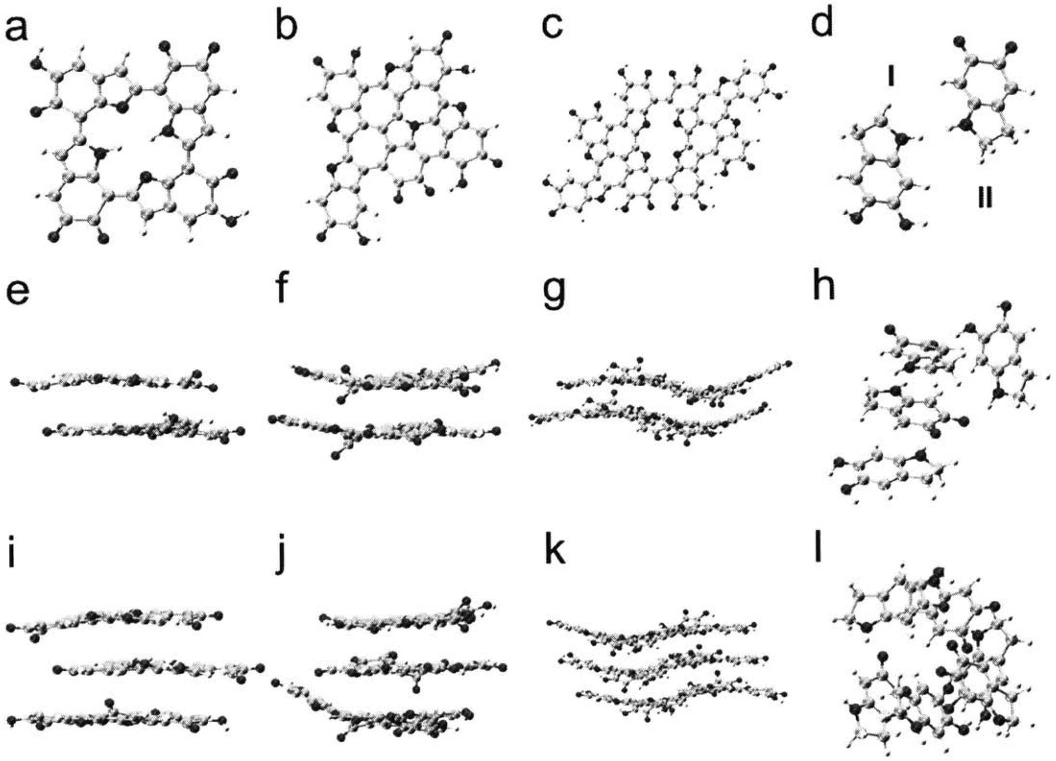

Figure 3-1: Molecular models of eumelanin. (a) Tetrameric model proposed by Kaxiras et al. [5]. (b) Pentameric and (c) octameric models proposed by Cheng et al. [6, 7]. (d) Monomeric model proposed by Dreyer et al. [8]. The two monomers in the monomeric model are called M1 and M2 here. Two-layer stacked structure of (e) tetrameric, (f) pentameric, and (g) octameric models, respectively. (h) Two-set (two M1 monomers and two M2 monomers) stacked structure of monomeric model. Three-layer stacked structure of (i) tetrameric, (j) pentameric, and (k) octameric models, respectively. (l) Three-set (three M1 monomers and three M2 monomers) stacked structure of monomeric model. The equilibrium structures are obtained from MD simulations with the NVT ensemble at a constant temperature of 300 K for 2.0 ns. This figure is adopted from Ref. [9]. Reprinted with permission from Nature Publishing Group.

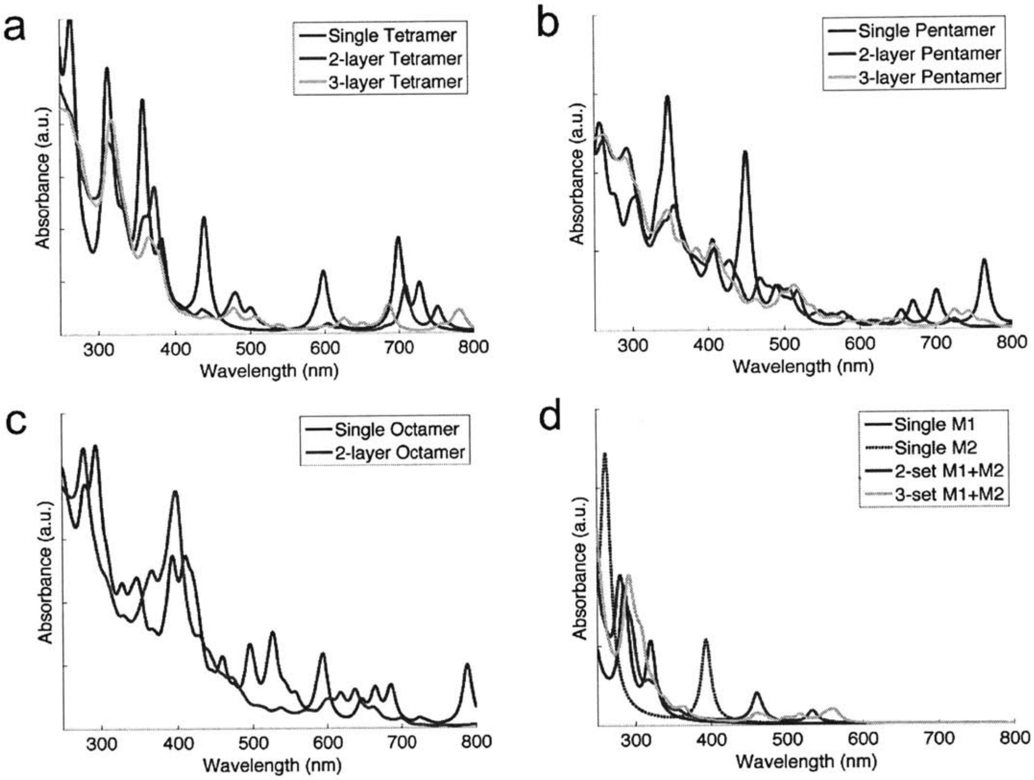

Figure 3-2: Absorption spectra of small-scale systems. The respective spectra are calculated directly with the ZINDO/S method. This figure is adopted from Ref. [9]. Reprinted with permission from Nature Publishing Group.

the simulated spectra of the monomeric model (Fig. 3-3d) show that the monomers cannot absorb visible light, which is in marked contrast with the experimental spectra of eumelanin [22, 23, 24]. In addition, the absorption spectra of the systems consisting of 27 oligomers (or 54 monomers) are similar to those systems consisting of 729 oligomers (or 1,458 monomers). This similarity suggests that the large-scale systems considered in this chapter are large enough to capture the full picture of the optical properties of eumelanin. In other words, the delocalization length of the exciton is much smaller than the box size. This result holds not only for the possibly hypothetical planar tetrameric model proposed by Kaxiras et al. [5], and for the planar pentameric and octameric models proposed by Cheng et al. [6, 7], but also for the non-planar oligomers (see Appendix B.4 for details) whose presence in solution has been demonstrated experimentally [12, 13].

3.3.3 Spectral broadening from excitonic interactions

Intriguingly, the peaks at the lower-energy end of the simulated spectra are broadened and lowered substantially compared to those at the higher-energy end. Two main factors contribute to this observation. First, the excitonic interactions among the stacked eumelanin protomolecules are enhanced due to the short interlayer spacing around 3–4 Å. This short spacing essentially grants the excitons extended radii over some neighboring molecules. The energies of the excitons are then redistributed within the range of approximately $4\left|\bar{J}\right|$, where $\left|\bar{J}\right|$ is the average nearest neighbor coupling strength, centered at the gas phase peak locations [82]. Second, upon close inspection of the microscopic details of molecular arrangements obtained through the MD simulations, no correlation of molecular orientations within individual secondary structures is observed. In other words, the self-assembly mechanism of eumelanin protomolecules is characterized only through reducing intermolecular separations and the alignment of molecular planes, whereas molecules are allowed to rotate freely on the axis of aggregations. This randomness is due to both the isotropy and weakness of the intermolecular forces compared to the kinetic energy at physiological temperatures. Consequently, the oscillator strength is redistributed more or less evenly within the

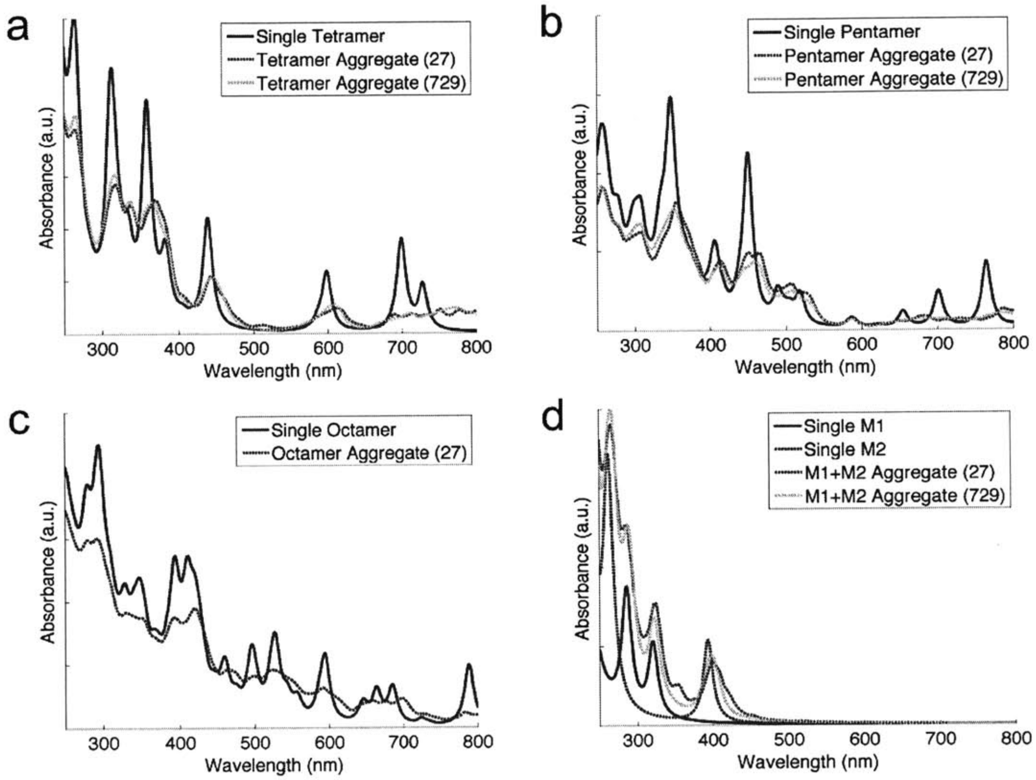

Figure 3-3: Absorption spectra of large-scale systems. Quantum chemistry calculations are not feasible in this case. Excitonic interactions are calculated through the Frenkel exciton model with the atomic transition charge distribution method. This figure is adopted from Ref. [9]. Reprinted with permission from Nature Publishing Group.

range of $4\left|\bar{J}\right|$ as mentioned above. This result is in sharp contrast to the phenomenon of exchange narrowing observed in aggregate molecular systems having well-defined geometries, especially with definite orientation order [83].

Generically, the gas phase absorption peaks of the eumelanin protomolecules are redistributed when they randomly stack together and are allowed to interact via excitons. Moreover, this redistribution is carried out in such a way that ones with lower transition energies are spread to a larger extent than others. The low energy transitions are attenuated compared to the high energy ones upon the formation of secondary structures. These results in the rather featureless spectrum in which the absorbance increases toward the higher-energy end in a monotonic manner, and in agreement with the experimental findings [22, 23, 24]. A simple explanation can be given to rationalize this observation: using the tetrameric model as an example, and considering a simpler situation, where only two absorption peaks of individual molecule are retained, one located at 358 nm and another at 699 nm with similar oscillator strengths (64.7 and 61.3 Debye^2 from the ZINDO/S method, respectively), and the Frenkel exciton model calculation is performed with the same aggregate structure (i.e., 729 tetramers, see Chapter 2 for details). These two absorption peaks are located at the two extremities of the visible spectrum. The simulated spectra of this simplified system are shown in Fig. 3-4a and 3-4b. As indicated in the figures, there is no noticeable intensity borrowing effect [84] between the two energetically well-separated bands, since the ratio between the integrated intensities are the same for the gas phase and aggregate structure. In frequency space (Fig. 3-4a), the bandwidth of these two bands is roughly the same (6.0×10^3 cm^{-1} for the lower-energy band and 7.5×10^3 cm^{-1} for the higher-energy band). However, when plotted in wavelength space (Fig. 3-4b), the bandwidth of these two bands appears to be drastically changed relative to each other: the higher-energy band is much narrower than the lower-energy band.

The above observation is rationalized as follows. The average excitonic couplings of these two excitations within the single excitation manifold ($\bar{J}_k$) are similar. Therefore, as stated previously, the width of the bands is also similar in frequency (energy)

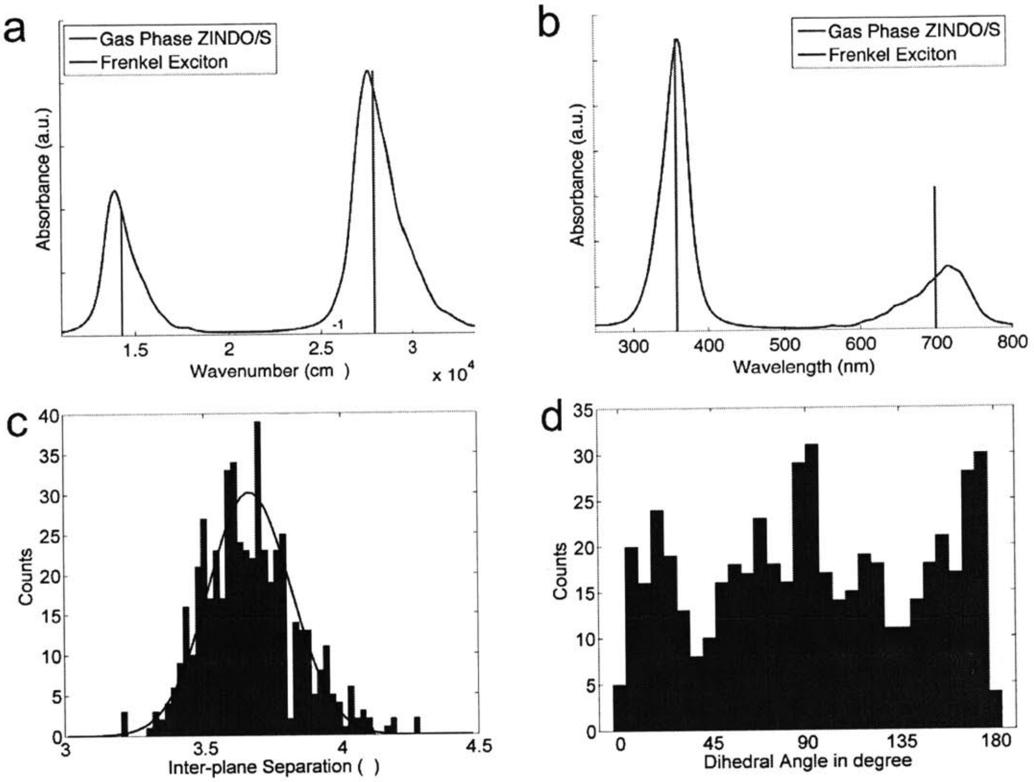

Figure 3-4: Absorption spectra of simplified system and in-depth analysis of MD simulation trajectory. The panels depict comparison of same absorption spectrum in (a) frequency and (b) wavelength space, calculated with the same aggregate structure (i.e., 729 tetramers) but using only two transitions ($E_k = 2.79 \times 10^4$, 1.43×10^4 cm^{-1} or $\lambda_k = 358$, 699 nm) and oscillator strengths ($f_k = 64.7$, 61.3 Debye^2) per molecule. Red sticks correspond to result from the ZINDO/S method for gas phase, and blue line represents result of the Frenkel exciton calculation for aggregate structure. (c) Distribution of plane-to-plane distances. The mean value is 3.67 Å, with a standard deviation of 0.15 Å, when fitted to the Gaussian distribution. (d) Distribution of dihedral angles among adjacent molecules. The result indicates that there is no preferred rotational configuration of stacked eumelanin protomolecules. This figure is adopted from Ref. [9]. Reprinted with permission from Nature Publishing Group.

space. In other words, the location and the range of the bands can be represented as $E_k \pm \alpha \bar{J}_k$, where E_k is the energy of the k-th gas phase absorption peak (in wavenumber) and is a dimensionless constant. The same expression in wavelength space is show below:

$$\frac{10^7}{E_k \pm \alpha \bar{J}_k} = \frac{10^7}{E_k}\left[1 \pm \frac{\alpha \bar{J}_k}{E_k} + \left(\frac{\alpha \bar{J}_k}{E_k}\right)^2 + \dots\right] \approx \lambda_k \pm \alpha' \frac{\bar{J}_k}{E_k^2} \tag{3.3}$$

where 10^7 is the transformation factor relating wavenumbers and wavelengths. The term $\lambda_k = 10^7/E_k$ is the wavelength of the k-th transition in nanometer, and $\alpha' = 10^7 \cdot \alpha$ is the proportionality factor in wavelength space. The Taylor series is truncated to the first order in $\alpha \bar{J}_k/E_k$, which is typically on the order of 10^{-1} to 10^{-2} in the calculations and is characteristic of molecular aggregates in the visible light region [76]. Note that the bandwidth is now proportional to $\bar{J}_k/E_k^2$. In the simplified two-state calculation, this means that the ratio of the width of the two bands is multiplied by a factor of $(E_1/E_2)^2 = 3.8$, in favor of the band with higher energy. Moreover, due to the summation rule of oscillator strength, this corresponds to a relative increment in the absorption intensity by a factor of 3.8.

Another factor comes from the fact that the absorbance is proportional to the product of oscillator strength and transition energy. In typical spectroscopic studies on molecular aggregates, one usually focuses only on the oscillator strength and takes the transition energy as constant. The reason is that the absorption intensities of molecular aggregates with well-defined geometries are concentrated at the upper or lower band edges, for H- or J- aggregates [85], respectively. However, in this work, the energy range under discussion is very broad, and the lack of ordered aggregate structures precludes the intensity-concentration effect. Apart from the oscillator strength characteristic of the selected eumelanin protomolecules, there is an additional factor of transition energy contributing to the absorption intensity. The above argument also applies to the general situation where all gas phase transitions (instead of just two) are included. Moreover, this argument is not limited to the systems that consist only one kind of molecular structure and is also compatible with the chemical disorder model.

3.3.4 Statistical view of geometric order and disorder

To support the above argument, the same aggregate structure (i.e., 729 tetramers, see Chapter 2 for details) is used as an example, and a more in-depth analysis of the MD simulation trajectory is presented. The statistical analysis on the geometry of adjacent molecules is shown in Fig. 3-4c and 3-4d. In Fig. 3-4c, the distribution of interlayer spacing between adjacent molecules is plotted. The definition of intermolecular adjacency is provided in Appendix A.1. The distribution has a Gaussian form with a mean value of 3.67 Å, which correlates well with the experimental observations [10, 40]. In addition, the distribution of the dihedral angles between adjacent molecules is shown in Fig. 3-4d. No preferred rotational configuration of the stacked molecules at physiological temperatures is observed. The above observations, consistent with the experimental findings that there is no crystalline order within eumelanin aggregate structures [10, 40], is crucial to the explanation of the broadband absorption feature induced by excitonic couplings. This kind of disorder destroys the intensity-concentrating effect typically observed in molecular (H- or J-) aggregates with rotational ordering. In the rotationally disordered eumelanin aggregate structures, the oscillator strength is scattered across the full range of the band, spanned by the excitonic couplings.

From the above analysis, the geometric order together with disorder originating from the thermodynamics of the large-scale systems lead to the peculiar characteristics of the optical properties of eumelanin can be concluded. The geometric order refers to the stacking of the planar eumelanin protomolecules with nearest separation in a range of 3–4 Å, whereas the geometric disorder refers to the lack of preference on the rotational degrees of freedom between adjacent molecules, as well as the slipping along the molecular planes. The geometric order gives rise to significant excitonic couplings among eumelanin protomolecules. On the other hand, the geometric disorder scatters the absorption intensity over the exciton energy band.

3.4 Conclusions

The absorption spectra of eumelanin aggregate structures consisting of hundreds of eumelanin protomolecules with a proper account of excitonic couplings are calculated for the first time. This chapter shows that the inclusion of excitonic interactions among eumelanin protomolecules drastically changes the landscape of the spectrum, which mimics the one obtained experimentally. The interplay of geometric order and disorder characteristics of eumelanin aggregate structures results in significant and random excitonic couplings among the molecules. Consequently, these couplings broaden the spectrum and give rise to a relative enhancement of absorption intensity at the higher-energy end, which is proportional to the cube of the absorption energy. While the chemical disorder is not included explicitly and the absorption spectra are calculated individually for each molecular model, this principle is compatible with the general case including chemical inhomogeneity. It should be noted that several research groups have considered the effect of dynamical disorder [86, 87], where short-range interactions among nearby molecules affect the molecular geometry dynamically. However, as in the case of chemical (static) disorder model, the excitons are still restricted within one (segment of a) molecule since their interactions are neglected in these studies. As such, the delocalization of excitons over several neighboring eumelanin protomolecules will prove crucial for the comprehensive understanding of the broadband absorption feature.

This chapter shows that the excitonic effect can play a decisive role in the interpretation of the broadband absorption spectrum of eumelanin. The significance of the excitonic couplings is strongly suggested by the fact that eumelanin is composed of (a mixture of) conjugated molecules and the short interlayer spacing among the stacked eumelanin protomolecules shown in both the MD simulations and experiments. In addition, the rotational disorder and slip along molecular planes within individual secondary structures are also key ingredients to the spectroscopic features of eumelanin. The results confirm the model of heterogeneous aggregation for eumelanin, but in a different way than previous reports that deal with the simulations of the optical properties of eumelanin, based on solely the superposition principle. In the earlier reports, the heterogeneity originated from a chemical point of view since different eumelanin protomolecules were used to calculate the absorption spectra. In contrast, the heterogeneity in this chapter comes from the fact that the stacked eumelanin protomolecules have various sizes and randomly oriented, leading to the peculiar excitonic interactions among them.

More broadly, this chapter demonstrates that in addition to the exact chemical identity of eumelanin, which differs from one kind of molecules to another, there exists a universal enhancement of absorption intensity to the cube of the absorption energy. Therefore, the overall shape of the eumelanin spectrum, which is broadband and smoothly decaying to the lower-energy end, can be rationalized accordingly. It should be noted that although the chemical disorder model can explain the broadband absorption feature of eumelanin, it is unable to explain why the spectrum of eumelanin is monotonically increasing toward the higher-energy end. In contrast, this chapter reveals both important optical characteristics of eumelanin. The concept uncovered here has implications beyond the specific microscopic models of eumelanin, and provides a significant advance in the understanding of the optical properties of other materials with similar chemical and structural characteristics. It may also enable the design of bio-inspired materials with similar optical properties as eumelanin.

Chapter 4

Mechanical properties of eumelanin

This chapter contains the content regarding the mechanical properties of eumelanin in the publications:

1. Shangchao Lin, Chun-Teh Chen, Igor Bdikin, Vincent Ball, Jose Gracio, and Markus J. Buehler. Tuning heterogeneous poly(dopamine) structures and mechanics: *in silico* covalent cross-linking and thin film nanoindentation. *Soft Matter*, 10(3):457464, 2014.
2. Chun-Teh Chen, Chern Chuang, Jianshu Cao, Vincent Ball, David Ruch, and Markus J. Buehler. Excitonic effects from geometric order and disorder explain broadband optical absorption in eumelanin. *Nature Communications*, 5, 2014.

4.1 Introduction

Eumelanin is a ubiquitous biological pigment and also the predominant component in the human pigmentary system. In addition to its well-known pigmentation and photoprotective function, which is discussed in Chapter 3, eumelanin also provides structural support for binding protein and metals in some living organisms. For instance, eumelanin has been identified as a major constituent of the jaws of the bloodworm (*Glycera dibranchiata*). Moses et al. [88, 89] showed that the abrasion resistance of the jaws is superior to all engineering polymers and competitive with the hardest metallic alloys based on the metric H^3/E^2 (H is the hardness and E is the Young's modulus). The remarkable mechanical properties of the jaws come from a robust cross-linked network of organic molecules, particularly eumelanin.

A fundamental question concerning natural eumelanin and synthetic eumelanin (PDA) is how their structures and self-assembly result in their properties. The heterogeneous polymeric nature of eumelanin-like materials makes them difficult to characterize owing to their insolubility in most organic solvents. Nevertheless, there is a broad consensus that the fundamental building block of eumelanin and PDA is DHI, an intermediate oxidized product of dopamine (Fig. 4-1a) [11], while the debate concerns the self-assembly and oxidative polymerization mechanism. Inspired by previous studies of natural eumelanin, which share many characteristics with PDA thin films, several covalently cross-linked molecular models have been suggested. Linear oligomeric structures, wherein DHI monomers are covalently cross-linked via aryl–aryl linkages on different possible reaction sites on the indole ring (Fig. 4-1a) [11], are the most popular structures [50, 90]. Although the polydispersity of such an oligomeric system has not been (and is not easily) quantified, it is proposed that each linear oligomer, on average, is composed of around four DHI monomers (as a tetramer) [90]. In Chapters 2 and 3, the four different eumelanin molecular models are used to study the self-assembly and structural properties of eumelanin. It should be noted that although the oligomeric models (i.e., tetrameric, pentameric, and octameric models) discussed in Chapters 2 and 3 can reproduce some physical properties of eumelanin-like materials, other possible covalently cross-linked molecular models cannot be completely ruled out without more experimental and computational evidence.

The proposed covalently cross-linked molecular models of eumelanin and PDA differ mainly in: (i) the degree of cross-linking or polymerization (η), as reflected by the number of cross-links in the entire polymeric system, and (ii) the polydispersity index (PDI), as indicated by the resulting distribution of molecular weight of (or the number of monomeric units in) an oligomer. Recently, Dreyer et al. [8] suggested that PDA is not a covalent polymer but instead a supramolecular aggregate of monomers consisting primarily of DHI and its redox forms. This monomeric model is discussed in Chapters 2 and 3 can be viewed as the reference state in which $\eta = 0$ and PDI $= 1$ for a homogeneous system. In Chapters 2 and 3, the four eumelanin molecular models are adopted from literature; therefore the degree of polymerization cannot be adjusted during the simulations. In this chapter, a computational model in which the degree of polymerization can be controlled via *in silico* covalent cross-linking between DHI monomers is proposed. The resulting distribution of the number of monomeric units in an oligomer (e.g., dimer, trimer, tetramer, and pentamer), the polydispersity index (PDI), and the simulated mechanical properties in terms of the elastic constant (Young's modulus, E) of the generated systems are reported as a function of the degree of cross-linking. Simulation results are compared with the simulated mechanical properties obtained using the four eumelanin molecular models discussed in Chapters 2 and 3, as well as previous experimental studies on natural eumelanin.

4.2 Methods

4.2.1 Non-covalent DHI aggregate simulations

Full atomistic MD simulations are implemented using LAMMPS [57] with CVFF [58, 59] in this chapter. The simulation setup is the same as that described in Chapter 2. The initial pure DHI system consists of 840 ordered DHI monomers positioned in a cubic lattice. After energy minimization, the system is simulated with the NPT ensemble at a constant temperature of 600 K and pressure of 1.013 bar for 2 ns. The high temperature allows the DHI monomers to reach the most stable configurations much faster than at room temperature (300 K) and removes the ordering of the DHI monomers in the initial lattice conformation. The system is then cooled down and equilibrated with the NPT ensemble at a constant temperature of 300 K and pressure of 1.013 bar for another 2 ns to study the mechanical properties at room temperature and standard atmosphere pressure.

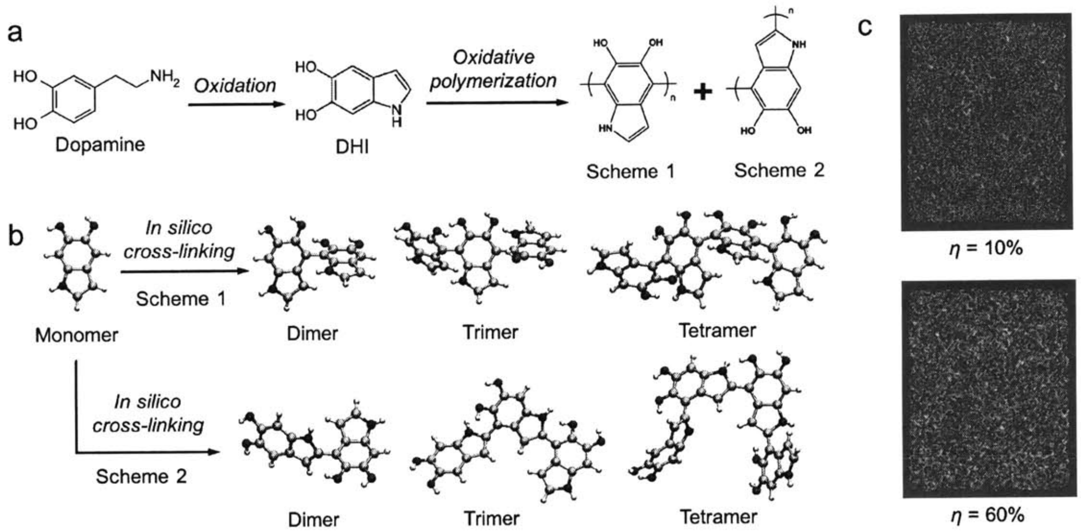

Figure 4-1: Schematic outline of DHI polymerization mechanism. (a) Intermediate oxidized product of dopamine, DHI, and two most possible schemes for oxidative polymerization of DHI at different cross-linking sites to form linear oligomers. (b) Representative simulation snapshot of DHI monomer and oligomers (dimer, trimer, and tetramer) formed after controlled cross-linking process under Schemes 1 and 2. (c) Simulation snapshots of simulated cross-linked DHI systems under lower (10%) and higher (60%) degrees of cross-linking. The covalent bonds added in both systems are highlighted using red lines. This figure is adopted from Ref. [11]. Reprinted with permission from Royal Society of Chemistry.

4.2.2 Cross-linked DHI oligomer simulations

Cross-links between two DHI monomers are introduced by adding covalent bonds between two aryl carbon atoms if their distance is within a specified cutoff. The added covalent bonds possess equilibrium bond length $r_0 = 1.33$ Å and spring constant $k_b = 655.2$ kcal mol^{-1}, which are the CVFF parameters corresponding to the C–C bonds connecting the DHI-like monomers. Different cutoff distances and simulation times are tested (trial-and-error) to generate the desired degrees of cross-linking. The two most probable polymerization schemes in Fig. 4-1a are both investigated. Under both schemes, the maximum number of covalent bonds that can be added is equal to the total number of DHI monomers in the system (in this case, $B_{max} = 840$), because each DHI monomer can only link to a maximum of two DHI monomers. The degree of cross-linking, η (in %), is defined as the number of bonds added, B, divided by $B_{max} = 840$ (i.e., $\eta = B/B_{max}$). The cutoff criteria for bond addition are fine-tuned to control the values of η to be within a range of 10% and 70%. The equilibrated configuration of the pure DHI aggregate system ($\eta = 0\%$) is used as the initial configuration for introducing cross-linking. After bond addition, the extra hydrogen atoms attached to the aryl carbons are removed, together with the associated bond, angle, and dihedral interactions. All the above bond addition and atom deletion functions are already implemented in LAMMPS. After energy minimization, the cross-linked DHI systems are equilibrated using the same method as for the pure DHI system.

4.2.3 Mechanical property assessment

Mechanical tensile tests are implemented to estimate the Young's moduli using the equilibrated configurations of the pure DHI system and covalently cross-linked DHI systems with different degrees of cross-linking. The systems are simulated at 300 K under a time-dependent semi-isotropic NPT ensemble. Specifically, one of the three normal stresses (diagonal stress tensors) of the simulation box is linearly increased during the simulations to mimic tensile pulling in the X, Y, or Z direction, while the other two normal stresses are kept at 1.013 bar. The equilibrium simulation box size and normal stress in each direction are recorded during the simulations to generate the stress-strain curves to compute the Young's moduli. The same mechanical tensile tests are also implemented to the large-scale systems consisting of 729 oligomers (i.e., tetramers, pentamers, and octamers) or 1,458 (729-set) monomers for comparison.

4.3 Results and discussion

4.3.1 *In silico* cross-linking process

The randomized non-covalently self-assembled monomeric DHI system is simulated first to serve as a reference system for the subsequent cross-linking study. To confirm the isotropy of the equilibrated DHI system, orientation analysis of the DHI monomers is performed by dealing with them as planar molecules. The orientation of each DHI monomer is defined by the normal vector of the planar indole ring. As shown in Appendix Fig. B-3, the X, Y, and Z components of the orientation vectors of DHI monomers are highly randomized, thus confirming the isotropy of the system. The isotropy of the cross-linked DHI systems is also confirmed by performing the same orientation analysis of the DHI monomers under both cross-linking schemes.

Representative simulation snapshots of the different oligomers (dimer, trimer, and tetramer) formed after the controlled cross-linking processes are shown in Fig. 4-1b for both cross-linking schemes in Fig. 4-1a. Due to steric hindrance between the two parallel indole rings in Scheme 1, the resulting oligomer structure exhibits an out-of-plane feature between each monomer. The angle formed between two neighboring indole rings is around 90 degrees (i.e., perpendicular to each other). In the case of Scheme 2, the steric hindrance is much less; thus, the two neighboring indole rings can locate on the same plane to form larger planar structures. In particular, the tetrameric molecular structure formed under Scheme 2 can almost reproduce the porphyrin-like tetrameric molecular structure proposed by Kaxiras et al. [5] if the two ends of the chain can get close enough to each other to form a covalent bond. However, the probability of forming the cyclic tetramers is very low in the *in silico* cross-linking process using the initially randomized DHI system. Fig. 4-1c shows simulation snapshots of two cross-linked DHI systems under 10% and 60% degrees of cross-linking. The added covalent bonds are highlighted by red lines to confirm their randomness across the simulation box, as well as easily to distinguish the lower (fewer red lines) and higher (more red lines) cross-linking cases.

The distribution of the number of repeated DHI units in the system, resulting from the cross-linking process, for each i-mer, P_i, is shown in Fig. 4-2a. The number distribution for cross-linking Scheme 2 is almost the same as for Scheme 1. The peak of the distribution (in %) shifts to a higher number of DHI units as the degree of cross-linking, η, increases. In other words, larger oligomers form *in silico* after more covalent bonds are added in the simulations. For $10\% \leq \eta \leq 60\%$, the majority of the cross-linked DHI system is still composed of monomers. However, for $\eta =$ 70%, the composition of monomers becomes less than most of the oligomers (dimers, trimers, tetramers, and pentamers) and the peak of the distribution is located at the trimer. The non-uniform distributions of the DHI oligomers in Fig. 4-2a illustrate the heterogeneous nature of eumelanin and PDA.

The polydispersity index (PDI) is an important measure of the heterogeneity of a polymeric system, which is defined traditionally as:

$$\mathrm{PDI} = \frac{M_w}{M_n} \tag{4.1}$$

where M_w is the weight-averaged molecular weight and M_n is the number-averaged molecular weight. The two different definitions of the averaged molecular weight result from different experimental methods used to measure them. In experiments, the value of M_w can be measured using static light scattering, small-angle neutron scattering, or X-ray scattering, while the value of M_n can be measured using gel permeation chromatography or proton nuclear magnetic resonance (NMR). The definitions of M_w and M_n are shown below:

$$M_w = \frac{\sum M_i^2 N_i}{\sum M_i N_i} \quad and \quad M_n = \frac{\sum M_i N_i}{N_i} \tag{4.2}$$

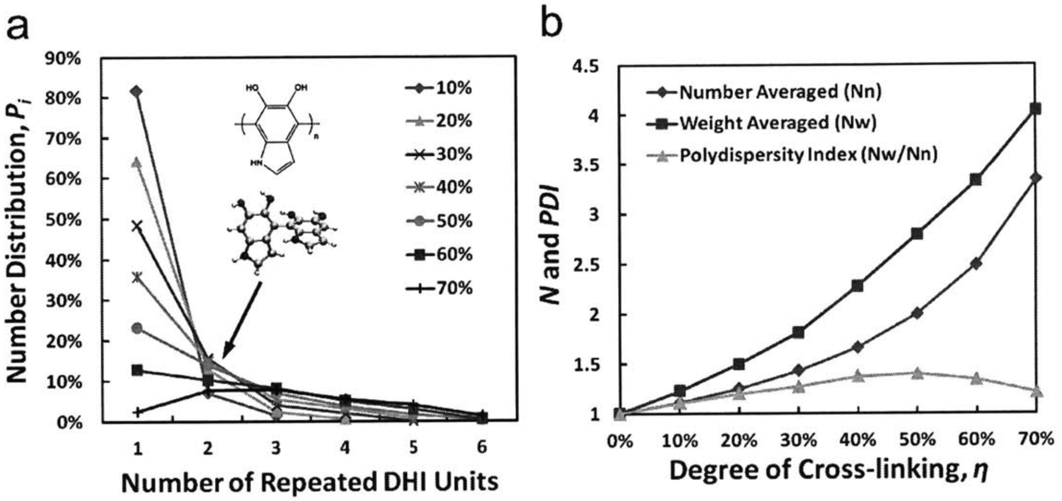

Figure 4-2: *In silico* cross-linking results. (a) Distribution, P_i, of number of repeated DHI units in oligomer formed from controlled *in silico* cross-linking process as function of degree of cross-linking, η. The structure of a dimer formed under cross-linking Scheme 1 is shown as an inset in the plot. (b) Number-averaged (N_n) and weight-averaged (N_w) number of monomeric units in *in silico* cross-linked DHI systems. The polydispersity index (PDI) is calculated as the ratio of the two averaged values as a function of the degree of cross-linking, η. This figure is adopted from Ref. [11]. Reprinted with permission from Royal Society of Chemistry.

where M_i is the molecular weight of an i-mer ($i = 1$ to 6, as shown in Fig. 4-2a) and N_i is the number of i-mers in each cross-linked DHI system, which can be directly obtained from the number distribution P_i (Fig. 4-2a) using the total number of DHI units (840) in the system: $N_i = 840\ P_i$. If we define constant m as the molecular weight of a DHI unit, then $M_i = im$ and Eq. 4.2 can be converted into:

$$M_w = m\frac{\sum i^2 N_i}{\sum iN_i} = mN_w \quad and \quad M_n = m\frac{\sum iN_i}{N_i} = mN_n \tag{4.3}$$

where N_w and N_n are the weight-averaged and number-averaged numbers of monomeric units of the cross-linked DHI system, respectively. Inserting Eq. 4.3 in Eq. 4.1 results in an alternative definition of the PDI, which is independent of the molecular weight of each DHI unit, m:

$$\text{PDI} = \frac{mN_w}{mN_n} = \frac{N_w}{N_n} \tag{4.4}$$

The values of N_w and N_n, as well as the resulting PDI of the cross-linked DHI systems, are shown in Fig. 4-2b, as a function of η. If there is only one type of DHI oligomer for a monodisperse system, then the summations in Eq. 4.3 can be removed. As a result, $N_w = N_n$ ($M_w = M_n$) and PDI = 1. For non-uniformly distributed systems, PDI > 1 always holds. As expected from the shift of peaks in number distributions in Fig. 4-2a, the values of both N_w and N_n increase as η increases in Fig. 4-2b. The maximum N_w and N_n values achieved at $\eta = 70\%$ are 4.0 and 3.3, respectively, which are very close to the proposed tetrameric (linear or cyclic) model of eumelanin and PDA [5, 53, 90]. The resulting PDI is between 1 (for the pure monomeric DHI system) and 1.4 (at $\eta = 50\%$) for a moderately heterogeneous system. It increases with η initially to the maximum value at $\eta = 50\%$ due to the emergence of oligomers from the cross-linking process. After the maximum is reached, PDI decreases with η due to the large decrease in monomers and the saturation of the size of the oligomers generated.

4.3.2 Simulated mechanical properties

The mechanical properties of the pure DHI and cross-linked DHI systems under both cross-linking schemes are studied using *in silico* tensile tests, with the stress-strain results shown in Fig. 4-3. The similarity of the stress-strain curves obtained in the X, Y, and Z directions confirms that the equilibrated systems are isotropic. A linear regression to the small strain data in all three directions gives an estimated value of the Young's modulus, E, and the associated standard error as a function of η, as shown in Fig. 4-4. The simulated Young's modulus of the pure DHI system is equal to 2.6 ± 0.1 GPa. In addition, no ring-stacking aggregate structure is observed for the pure DHI system due to thermal fluctuations and the small size of the individual indole ring. The large amount of hydrogen bonding enabled by the catechol groups in eumelanin-inspired DHI and other bio-inspired molecules, such as the mussel-inspired dihydroxyphenylalanine (DOPA), is one of the reasons for their strong surface adhesions to the underlying substrate as a robust coating material, as revealed by a recent simulation work [91].

The simulated Young's moduli, E, for both cross-linking schemes are similar (within 0.3 GPa) to each other over the entire η range considered, which implies a small impact from the different cross-linking schemes. Consequently, the number of covalent bonds added *in silico* into the DHI system, instead of the actual cross-linking sites selected, dictates this mechanical property. An overall linear behavior is observed for E as a function of η, showing that each covalent bond added contributes to the same enhancement in E. In previous simulation studies on non-covalently cross-linked biopolymers, the degree of cross-linking has only minor impact on the elastic constant of the system [92, 93], since non-covalent interactions between individual molecules are much weaker than the covalent bonding in the DHI systems. The E value reaches the maximum value of 4.4 ± 0.1 GPa for Scheme 1 and 4.1 ± 0.1 GPa for Scheme 2 at the highest η value considered (70%).

In addition to the DHI systems discussed above, the four different eumelanin molecular models discussed in Chapters 2 and 3 are also adopted to study their

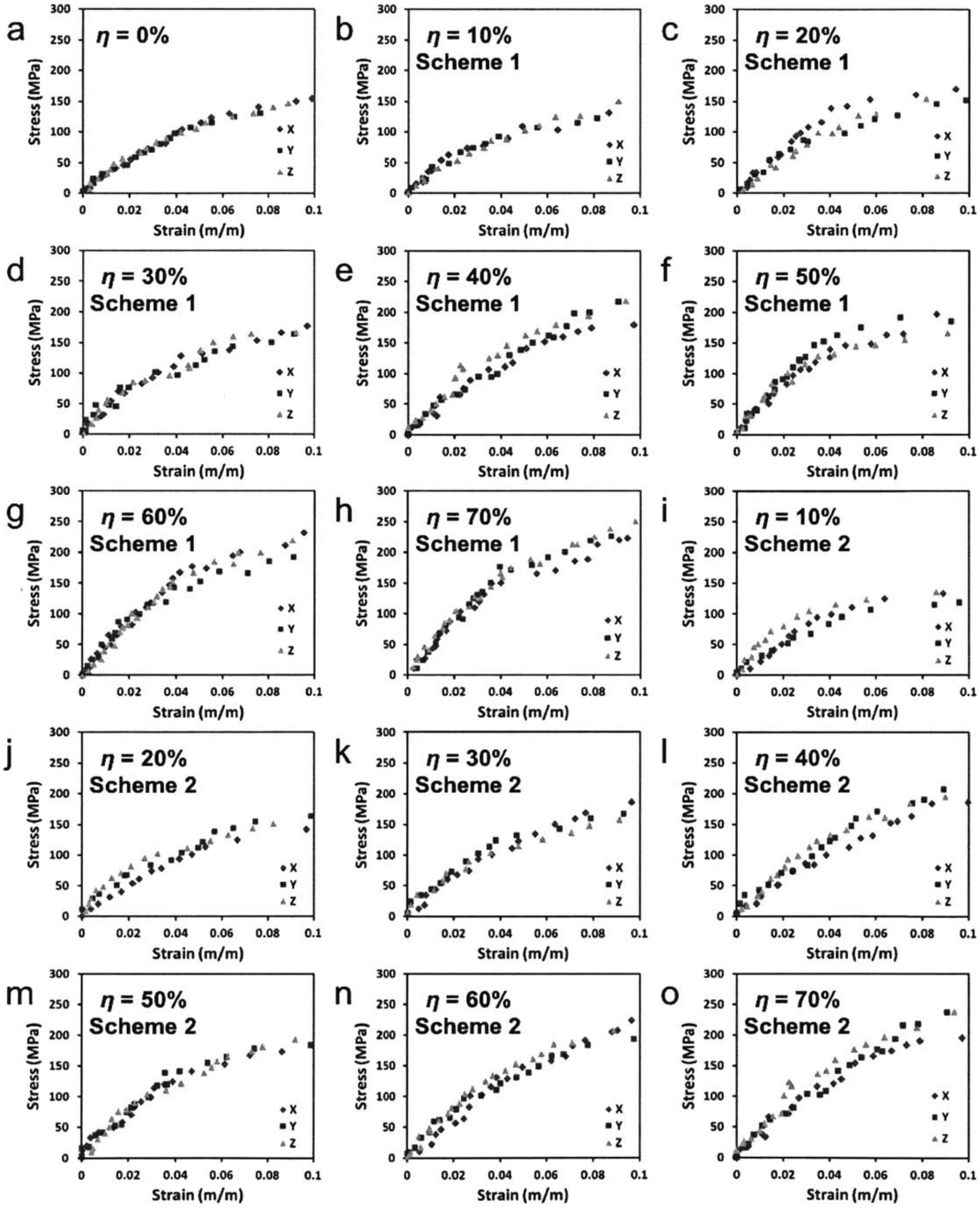

Figure 4-3: Stress-strain curves from mechanical tensile tests *in silico* using cross-linked DHI units. Stress-strain curves for (a) pure DHI aggregate system ($\eta = 0\%$), and (b)-(q) cross-linked DHI systems at various η values (10% to 70%) considered under cross-linking Schemes 1 and 2. This figure is adopted from Ref. [11]. Reprinted with permission from Royal Society of Chemistry.

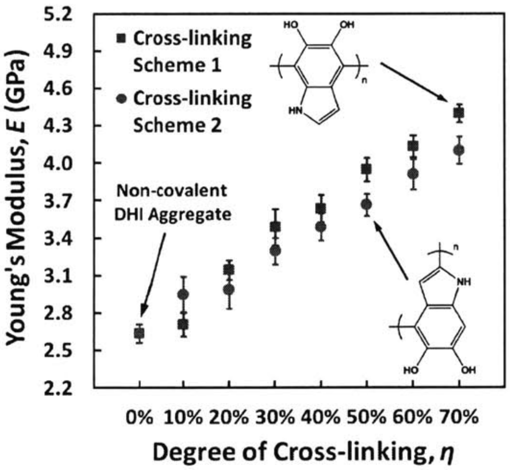

Figure 4-4: Young's modulus, E, of non-covalent DHI aggregate system and cross-linked oligomer DHI system as function of degree of cross-linking, η. The simulation results for both cross-linking schemes are plotted to illustrate the negligible impacts from the two different schemes. An overall linear behavior is observed for E as a function of η, showing that each covalent bond added contributes to the same enhancement in E. This figure is adopted from Ref. [11]. Reprinted with permission from Royal Society of Chemistry.

mechanical properties using the same *in silico* mechanical tensile tests. The stress-strain curves are shown in Fig. 4-5. The mass density calculated from the equilibrated large-scale systems is equal to 1.54 g/cm^3 for the tetrameric model, 1.61 g/cm^3 for the pentameric model, 1.56 g/cm^3 for the octameric model, and 1.26 g/cm^3 for the monomeric model. The mass densities of the oligomeric models are very close (1.54 to 1.61 g/cm^3) and are in good agreement with the experimental measurements (1.4 to 1.77 g/cm^3) [65, 88, 94]. However, the mass density of the monomeric model is significantly lower (1.26 g/cm^3). As with the DHI systems discussed above, the stress-strain curves obtained in the X, Y, and Z directions are very close, implying that the equilibrated systems are isotropic, in agreement with the random distribution of the eumelanin protomolecules Appendix B-2. The simulated Young's moduli are calculated from the stress-strain curves shown in Fig. 4-5, and are equal to 5.4 GPa for the tetrameric model, 7.8 GPa for the pentameric model, 7.4 GPa for the octameric model, and 4.2 GPa for the monomeric model.

In the cross-linked DHI systems, the maximum values of N_w and N_n achieve at

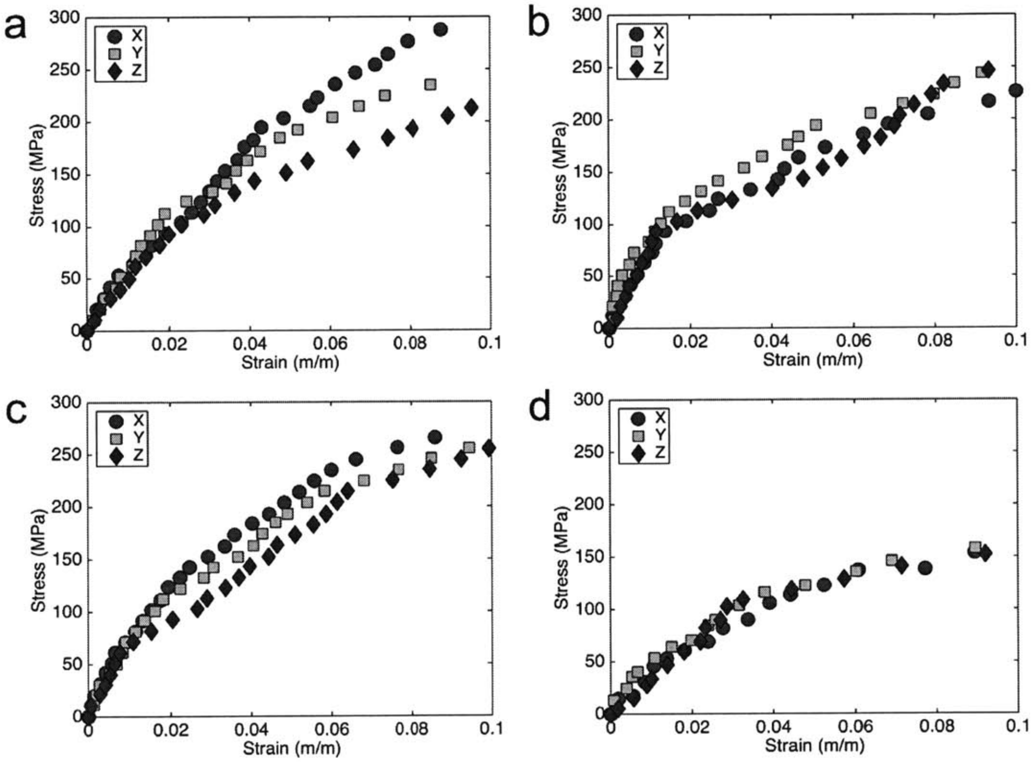

Figure 4-5: Stress-strain curves from mechanical tensile tests *in silico* using the four eumelanin molecular models. The stress-strain curves for the (a) tetrameric, (b) pentameric, (c) octameric, and (d) monomeric model, respectively. This figure is adopted from Ref. [9]. Reprinted with permission from Nature Publishing Group.

η = 70% are 4.0 and 3.3, respectively. As a result, PDI is equal to 1.2, which implies that different sizes of cross-linked DHI oligomers exist in the systems, and the average size of the oligomers is between trimer and tetramer. On the other hand, in the system consisting of 729 tetramers, both N_w and N_n values are equal to 4.0, and PDI is equal to 1.0. These values show that tetramer is the only size of the oligomers existing in the system. The average size (tetramer) is slightly larger than that in the cross-linked DHI systems at η = 70%. As discussed above, an overall linear behavior is observed for E as a function of η (Fig. 4-4), which suggests that the more covalent bonds added in a system (larger oligomers formed), the higher the Young's modulus of the system. This result might explain the higher Young's modulus (5.4 GPa) obtained in the system consisting of 729 tetramers compared to the Young's modulus (4.4 ± 0.1 GPa for Scheme 1 and 4.1 ± 0.1 GPa for Scheme 2) obtained in the cross-linked DHI systems at η = 70%. In the case of the system consisting of 729 pentamers, an even higher Young's modulus (7.8 GPa) is found, probably also due to the larger size of the oligomers. However, in the case of the system consisting of 729 octamers, the Young's modulus (7.4 GPa) is slightly lower than that obtained from the system consisting of 729 pentamers. This result implies there exists an optimal size of the oligomers to maximize the Young's modulus. Note that the pentameric and octameric models are adopted from literature. The authors created these two molecular models merely based on the probable sizes of eumelanin protomolecules. The covalent bonds connecting the DHI units in the molecular models were randomly added (not derived from rigorous studies). Accordingly, these two molecular models (e.g., pentameric and octameric models) do not follow the two probable polymerization schemes (e.g., Schemes 1 and 2) discussed in this chapter. The Young's modulus (4.2 GPa) obtained from the system consisting of 1,458 (729-set) monomers is considerably higher than the Young's modulus (2.6 0.1 GPa) obtained from the pure DHI system. A possible explanation for this difference is that the monomeric model proposed by Dreyer et al. [8] includes two redox forms, providing strong hydrogen bonding between oxidized and unoxidized DHI monomers. In the pure DHI system, the intermolecular interactions might be weaker, since all the DHI monomers are un-

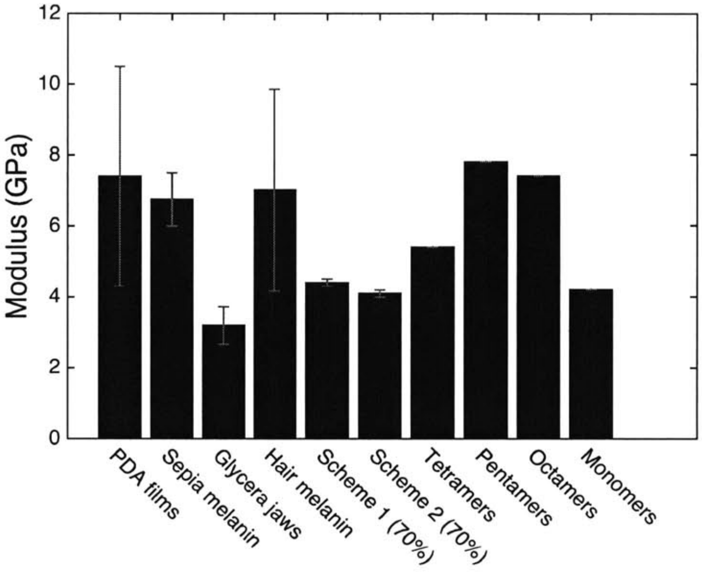

Figure 4-6: Young's modulus of eumelanin and PDA comparison between simulation predictions and experimental measurements.

oxidized. The Young's modulus (2.6 to 7.8 GPa) obtained from the cross-linked DHI systems and the systems consisting of 729 eumelanin protomolecules is of the same order as the Young's modulus (3.2 to 7.4 GPa) of eumelanin and PDA measured in the experiments (Fig. 4-6) [11, 88, 95].

4.4 Conclusions

In this chapter, a computational model of the heterogeneous DHI system is presented by mimicking the polymerization mechanism of DHI via controlled *in silico* covalent cross-linking between DHI monomers. The resulting distribution of the number of monomeric units in an oligomer, polydispersity index, and simulated Young's moduli of the generated DHI systems, as a function of the degree of cross-linking, are found consistent with previous experimental and simulation studies. These polydisperse DHI systems nicely complement the monodisperse eumelanin systems discussed in Chapters 2 and 3, to addresses the polydisperse nature of eumelanin and PDA. At the highest degree of cross-linking considered (η = 70%), the DHI system mimics and supports the proposed averaged tetrameric structures for eumelanin and PDA [5, 53, 90], and the simulated Young's moduli (4.1to 4.4 GPa) is in good agreement with experimental measurements of eumelanin and PDA (3.2 to 7.4 GPa).

The simulation results of the cross-linked DHI systems show the possibility of tuning the molecular structures and mechanical properties of eumelanin and PDA by controlling the extent of polymerization *in silico*, which suggests that in order to synthesize more mechanically robust eumelanin-like materials, one can use longer reaction time or more oxidative agents to introduce more cross-links in the system. Although the *in silico* model used in this chapter is simplified compared to the real complex polymerization mechanism, it provides new computational tools to study the mechanical properties of eumelanin-like materials. It also leads to a more in-depth understanding of the structure–property relationship for exploring practical applications of eumelanin-like materials by controlling polymer size, polydispersity, and aggregation for the engineering of tailored bio-inspired functional materials.

Chapter 5

Molecular structures of eumelanin

This chapter presents a description of the publication, Chun-Teh Chen, Francisco Martin-Martinez, Gang Seob Jung, and Markus J. Buehler. Polydopamine and eumelanin molecular structures elucidated from *ab initio* calculations (*in preparation*).

5.1 Introduction

The structural investigations of eumelanin are challenging due to its amorphous character and insolubility in water and most organic solvents. Therefore, it is currently not possible to provide an accurate picture of eumelanin structure beyond a description of its fundamental building blocks, which are DHI and DHICA [2]. In addition, very little information is available about the further evolution of these building blocks to eumelanin, and the exact polymerization mechanism is also unclear. The absence of proper molecular models for eumelanin and PDA implies a fundamental drawback that hampers a better understanding, fast development, and property optimization of eumelanin-like materials. Although the science and applications of PDA-based materials have rapidly advanced in recent years, most studies in this field were based on empirical approaches instead of a solid framework of structure-function relationships due to this structural controversy. In this chapter, a set of computational modeling methods, which includes a brute-force algorithmic generation of chemical isomers, MD simulations, and DFT calculations, is implemented to investigate the molecular structures of eumelanin and PDA. The investigation starts with analyzing the reactivity of a DHI monomer, and its related radical species that lead to the formation of eumelanin and PDA. The most reactive positions of a DHI monomer are identified, and an explanation of the polymerization of different redox forms of DHI based on spin density calculations is provided.

Early studies showed that the size of eumelanin protomolecules is around 15–20 Å, suggesting that the tetramers and pentamers formed by covalently bonded DHI are the most probable molecular structures of eumelanin [3, 6, 7, 42]. In addition, a recent study based on mass spectroscopic results of DHI-melanin also suggested that the major constituents of the material are the tetramers and pentamers of DHI [96]. As a result, this chapter is narrowed down to DHI oligomers up to tetramers. Within the framework of this bottom-up approach, and the locations of the most reactive positions of DHI, all probable early-polymerized DHI oligomers, ranging from dimers to tetramers, are systematically generated and analyzed, in order to provide fundamental explanations to some important structural features of eumelanin and PDA, as well as to propose a set of molecular models that represents the chemically diverse nature of these materials.

5.2 Methods

5.2.1 Reactivity and spin density

The reactivity of different molecules is characterized using the Fukui function dual descriptor, within the framework of conceptual DFT calculations [97]. The Fukui function describes how the electron density changes in response to increasing or decreasing in the number of electrons. Accordingly, it is employed to predict the preferred site for either nucleophilic or electrophilic attacks. The population of unpaired electrons for different sites in the radicals is quantified with electron spin densities, for which unrestricted open shell DFT calculations are performed.

5.2.2 Brute-force algorithmic generator

DHI oligomers are composed of various numbers of DHI units with different configurations. In this chapter, multi-layers of checkerboard plates are used to represent different polymerization degrees of DHI oligomers. For example, a tetramer can be generated by using four layers of checkerboard plates (Fig. 5-1a). To create all probable molecular structures, an algorithm using eight different orientations of a DHI monomer is proposed (Fig. 5-1b). Orientation 1 is the default orientation; Orientation 2 is a flipped structure of Orientation 1; Orientation 3 is a 90-degree clockwise-rotated structure of Orientation 1; Orientation 4 is a flipped structure of Orientation 3; Similarly, Orientation 5 is an 180-degree clockwise-rotated structure of Orientation 1; Orientation 6 is a flipped structure of Orientation 5; Orientation 7 is a 270-degree clockwise-rotated structure of Orientation 1; Orientation 8 is a flipped structure of Orientation 7. With these eight different orientations, DHI oligomers by assembling two or more DHI monomers with different orientations on checkerboard plates can be generated. Take dimers for an example, the first monomer in the brute-force algorithmic generator is set to the default orientation, Orientation 1, on the first layer of a checkerboard plate. Note that it makes no difference which orientation of a DHI monomer is selected to be the first monomer. The brute-force algorithmic generator can generate all probable DHI oligomers no matter which orientation of a DHI monomer is chosen as a starting point. According to DFT results on reactivity and spin density, which will be discussed in Results and Discussion section, the most reactive positions of a DHI monomer are the 2-, 4-, and 7-position. Thus, there are three reactive positions in a DHI monomer. The first reactive position considered in the brute-force algorithmic generator is the 7-position, and there are six orientations of a DHI monomer (i.e., Orientation 1, 2, 5, 6, 7, and 8) can form a covalent bond with Orientation 1 at the 7-position; The second reactive position is the 2-position, and there are also six orientations of a DHI monomer (Orientation 3, 4, 5, 6, 7, and 8) can form a covalent bond with Orientation 1 at the 2-position; The third reaction position is the 4-position, and there are also six orientations of a DHI monomer

(Orientation 1, 2, 3, 4, 5, and 6) can form a covalent bond with Orientation 1 at the 4-position. Consequently, a total of 18 combinations of positions and orientations can be generated on the second layer of a checkerboard plate. Combining the first and second layers of checkerboard plates, a total of 18 dimers will be generated. Appendix Fig. B-9 shows the checkerboard representations of these 18 dimers. The numbers on the checkerboard plates indicate the orientations of each DHI monomer, where the corresponding molecular structures are shown in Appendix Fig.B-10. While generating trimers, the third layer of a checkerboard plate is added to connect the third DHI monomer with the second DHI monomer. Since the second DHI monomer already formed a covalent bond with the first DHI monomer, there are only two reactive positions available to form a covalent bond with the third DHI monomer. As a result, a total of 12 combinations of positions and orientations can be generated on the third layer of a checkerboard plate for each dimer. Combining the first, second, and third layers of checkerboard plates, a total of 216 trimers will be generated. The molecular structures of these 216 trimers are shown in Appendix Fig. B-11 to B-22. Similarly, a total of 2,592 tetramers will be generated in the brute-force algorithmic generator. Fig. 5-1c shows the molecular structure of a tetramer that is generated according to the four layers of checkerboard plates shown in Fig. 5-1a. Finding the lowest energy conformation of an oligomer is essential for comparing its energy with other oligomers. Note that the brute-force algorithmic generator can not only generate all probable structural unique oligomers but also can generate different conformations, which oligomers can adopt due to rotation about sigma bonds. Thus, the conformational analysis is done at the same time as the energies of different conformations of oligomers are evaluated.

5.2.3 Atomistic modeling and equilibration

Full atomistic MD simulations are performed to relax and equilibrate the initial molecular structures of DHI oligomers generated from the brute-force algorithmic generator. As with Chapters 2, 3, and 4, full atomistic MD simulations are implemented using LAMMPS [57] with CVFF [58, 59] in this chapter. After energy minimization using

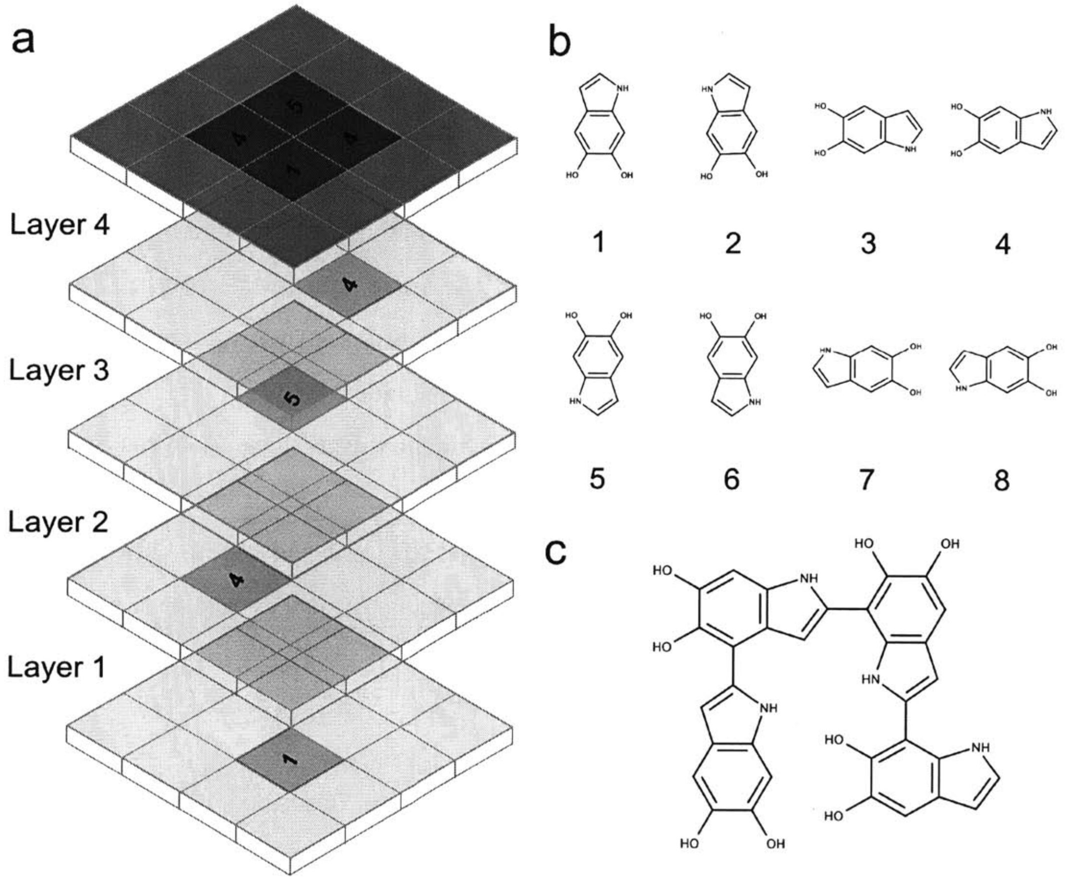

Figure 5-1: Brute-force algorithmic generator using multi-layers of checkerboard plates to generate different DHI oligomers. (a) Four layers of checkerboard plates for generating DHI tetramers. The red blocks represent the elements that are used for generating a DHI tetramer, and the blue blocks represent the available elements. The numbers on the red blocks represent the orientations of a DHI monomer. (b) Eight different orientations of DHI monomer considered. (c) Molecular structure of tetramer generated according to four layers of checkerboard plates shown in (a).

the CG algorithm, MD simulations are performed to equilibrate the molecular structures further. The MD equilibration includes ten iterations of equilibration to find the most stable geometry of a molecule. Each iteration contains four steps of the NVT ensembles. In the first step, a molecule is equilibrated with the NVT ensemble at the temperature starting from 1.0 K and increasing linearly to 300 K in 1.0 ps. In the second step, the molecule is equilibrated with the NVT ensemble at 300 K for 1.0 ps. In the third step, the molecule is equilibrated with the NVT ensemble at the temperature starting from 300 K and decreasing linearly to 1.0 K in 1.0 ps. In the final step, the molecule is equilibrated with the NVT ensemble at 1.0 K for 1.0 ps. A Langevin thermostat is performed to control the temperature. When the fourth step of MD equilibration is finished, the molecule is then relaxed with energy minimization again to calculate its energy. Thus, its geometry and the corresponding energy are recorded. This MD equilibration is repeated ten times. As a result, a total of ten geometries and the corresponding energies are recorded for each molecule. The geometry with the lowest energy is then selected for further geometry optimizations with DFT. The MD equilibration scheme is shown in Appendix Fig. A-5.

5.2.4 Geometry optimization

The geometries obtained from the MD equilibrations described above are further optimized using DFT calculations implemented in ORCA [71]. The B3LYP functional [72, 73] is adopted for optimizing the molecular structures, together with the 6-31G* basis set. The energies obtained in DFT calculations are used to benchmark the molecular structures of DHI oligomers.

5.2.5 Self-assembly modeling

In the initial configuration, eight tetramers are separated by a distance more than 40 Å to ensure that there are no intermolecular interactions. After energy minimization, the system is equilibrated with the NVT ensemble at 300 K for 10 ns. A Langevin thermostat is performed to control the temperature.

5.3 Results and discussion

5.3.1 DHI radical polymerization

The Fukui function gives an indication of the formation of the radicals while the spin density shows the delocalization of the unpaired electrons that control the radical reaction. Fig. 5-2a shows the dual descriptor of the Fukui function for DHI tautomers (i.e., HQ, NQ, MQ, and IQ). The colored surfaces represent those molecular regions suitable of undergoing either nucleophilic (purple) or electrophilic (green) attack. The results indicate that the reactivity of DHI is mainly concentrated in the catechol functional group. Therefore, an eventual electrophilic attack over the oxygen positions of DHI would be responsible for the formation of the following radical species in the oxygen atoms, while a nucleophilic attack over the carbon positions of the catechol ring would form the subsequent carbon radicals. Despite the uncertainty on the actual mechanism of radical generation, it is clear that four possible radical species can be formed in the catechol functional group.

Fig. 5-2b shows the spin density for these four HQ radical species, where the yellow surfaces indicate the probability density for the unpaired radical electron. HQ-o_{10} and HQ-o_{11} are the species where a hydrogen atom is removed from one of the hydroxyl functional groups, while HQ-c_4 and HQ-c_7 are the species where the unpaired electron is generated in one of the carbon atoms of the catechol ring. HQ-o_{10} and HQ-o_{11} are highlighted in a red box since these are the species that would initially form. As a result, they might be responsible for the initiation of the radical reaction. Within this context, HQ-o_{10} and HQ-o_{11} would potentially attack HQ, NQ, MQ and IQ to form more racial species through hydrogen abstraction mechanisms, therefore generating all radicals shown in Fig. 5-2c, 5-2d and 5-2e. Those species in which the radical is generated by hydrogen abstraction in the hydroxyl group present higher delocalization of the unpaired electron, which is located not only in the oxygen but also in some of the carbons of HQ. On the contrary, when the radical species are generated in the carbon atoms of the catechol, the unpaired electron remains mainly localized in the carbon. Fig. 5-2f summarizes the atomic positions that are most likely

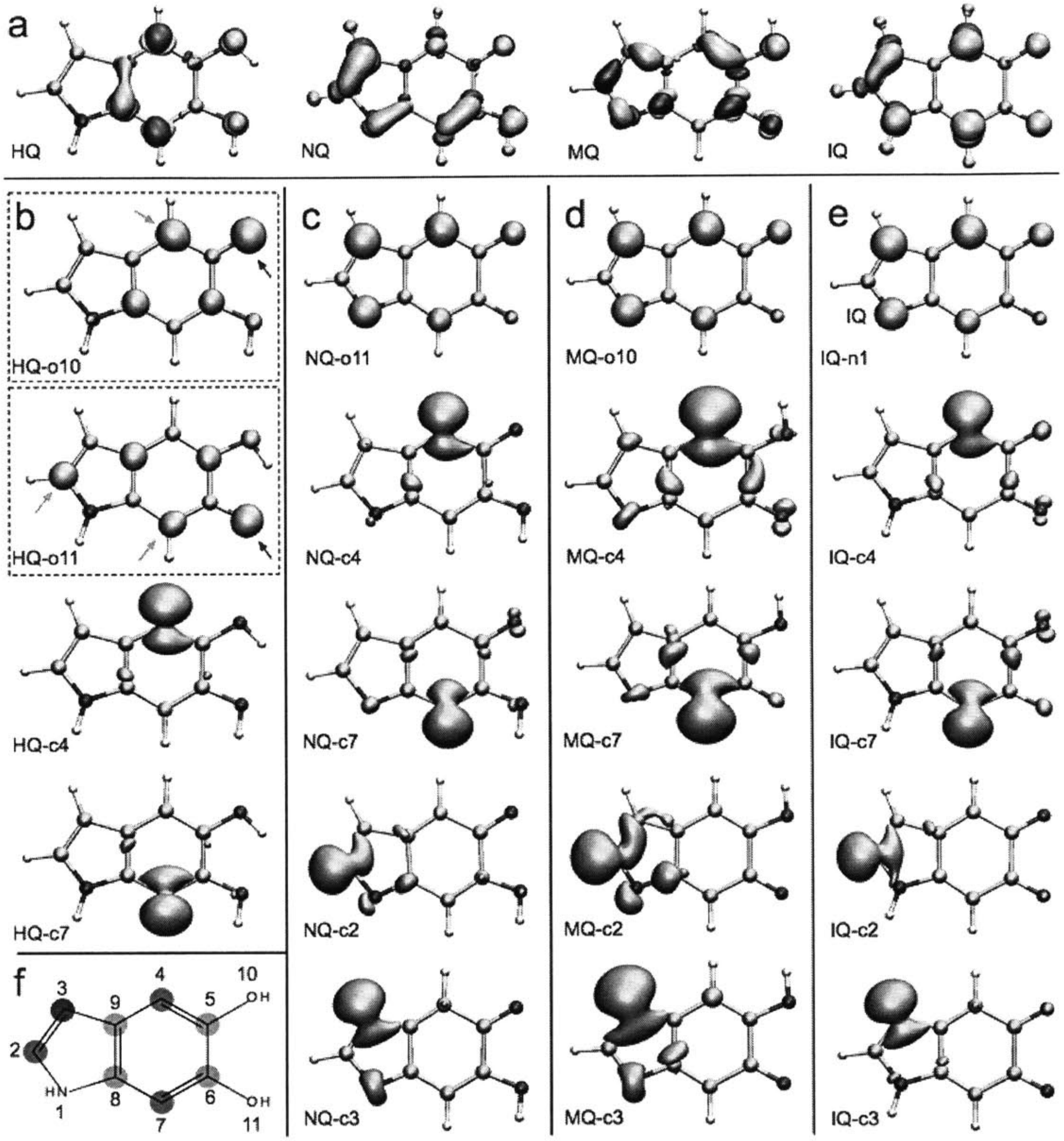

Figure 5-2: Reactivity of DHI and spin densities of its radical species. (a) Dual descriptor of Fukui function for all DHI tautomers. (b) Spin densities of possible radical species derived from HQ. The red dashed box indicates the two main radicals generated by the accepted reaction mechanism. (c) Spin densities of possible radical species derived from NQ. (d) Spin densities of possible radical species derived from MQ. (d) Spin densities of possible radical species derived from IQ. (f) Summary of most probable atomic positions for polymerization.

to polymerize based on the spin density analysis of all possible radical species. The position highlighted in red corresponds to the carbon in which the spin density is lower among all different structures. As a result, the unpaired electron in this carbon is less likely to appear. Accordingly, less number of cross-linking through this position is expected. The positions highlighted in orange (i.e., 5-, 6-, 8-, and 9-position) present localization of the spin density, but these are positions that are more difficult to access due to steric effects. On the contrary, the atomic positions highlighted in green (i.e., 2-, 4-, and 7-position) are easy to access during polymerization, and also present higher spin density in most of the cases, and more importantly in the main radical species generated from HQ (i.e., HQ-o_{10} and HQ-o_{11}). These three positions are indeed in agreement with the most stable connections in DHI oligomers, and even though there are four carbon positions in DHI that are suitable for polymerization, only these three are likely to polymerize in the radical reaction.

5.3.2 Proposed molecular structures for dimers

According to the results shown in the previous section, the unpaired electron in the radical species, which is a key player in the polymerization of DHI, is mainly localized in 2-, 4-, and 7-position. The results imply that the covalent bonds connecting DHI monomers to generate DHI oligomers are more likely to form at these positions. As a result of this specificity, there are 6 structural unique dimers (constitutional isomers), which are made through 2,2'-, 2,4'-, 2,7'-, 4,4'-, 4,7'-, and 7,7'-bonding positions. Nevertheless, to evaluate the stability of all different possible connections, a total of 18 dimers are generated with a brute-force algorithmic generator. Appendix Fig. B-10 shows the molecular structures of these 18 dimers. Note that this set of dimers not only covers all 6 structural unique dimers but also includes 12 redundant dimers with different conformations find the most stable conformation of each structural unique dimer. Appendix Table B.3 shows the relative energies compared to the most stable dimer as well as the covalent bonding positions of these 18 dimers. After discarding higher energy conformations, the more stable dimers are those made through 2,4'-position, 2,2'-position (+0.37 kcal/mol), 2,7'-position (+0.62 kcal/mol), and 4,7'-

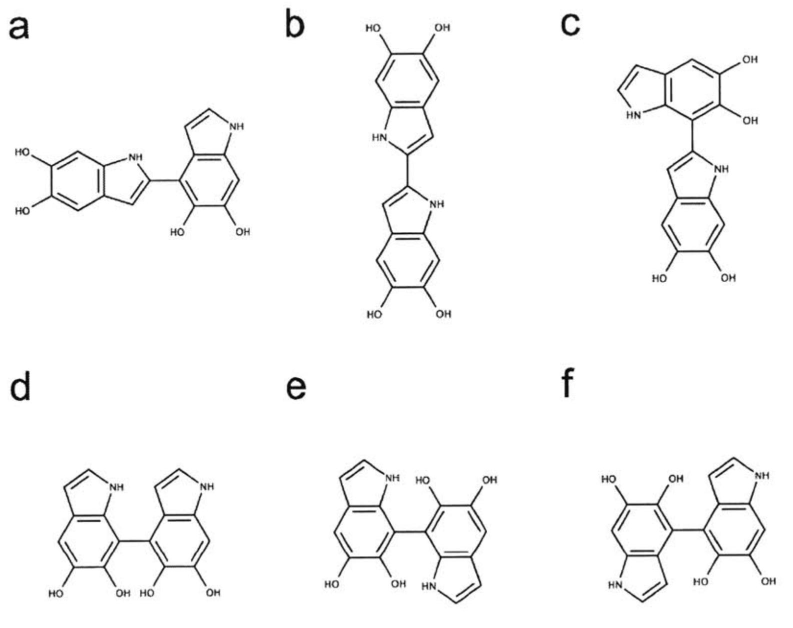

Figure 5-3: Molecular structures of 6 structural unique dimers. The more stable dimers are those made through (a) 2,4'-position, (b) 2,2'-position (+0.37 kcal/mol), (c) 2,7'-position (+0.62 kcal/mol), and (d) 4,7'-position (+0.63 kcal/mol). The less stable dimers are those made through (e) 7,7'-position (+0.94 kcal/mol), and (f) 4,4'-position (+1.14 kcal/mol).

position (+0.63 kcal/mol). On the contrary, the less stable dimers are those made through 7,7'-position (+0.94 kcal/mol), and 4,4'-position (+1.14 kcal/mol). Fig. 5-3 shows the molecular structures of these 6 structural unique dimers in the order of their relative energies.

The activation energies for DHI monomers to form various DHI oligomers are difficult to estimate without knowing the detailed reaction mechanism. However, the equal chemical functionalities and the similar structural conformations between the different species involved in the polymerization suggest similar energy barriers be expected. Furthermore, considering that it has been experimentally proven that the polymerization of DHI occurs, it is reasonable to assume that despite the energy barriers, the formation of oligomers is kinetically possible in most of the cases. As a result, it is the energy of the final structure that determines the prevalence of some oligomers with respect to others. Additionally, those oligomers with relative energy higher than the thermal energy (KE), which is 0.593 kcal/mol at room temperature, compared to the most stable molecular structure might be less likely to exist. These assumptions define a theoretical framework that allows us to evaluate different oligomers that contribute to the overall chemical structure of eumelanin and PDA. In Fig. 5-3, the last two dimers, which are made through 7,7'-position (Fig. 5-6e) and 4,4'-position (Fig. 5-6f), have relative energy considerably higher than the KE. Based on the assumptions, these two dimers are less likely to exist. Actually, the top 3 most stable dimers in this work, which are made through 2,4'-position (Fig. 5-3a), 2,2'-position (Fig. 5-3b), and 2,7'-position (Fig. 5-3c), has been identified in experiments by oxidation of DHI [12]. In addition, the simulations show that forming covalent bonds through 4,7'-position (Fig. 5-3d) is also possible. This bonding arrangement has also been verified in experiments [50]. The good agreement between the simulations and experiments supports the assumption that the molecular structures with lower energies are more likely to be found.

5.3.3 Proposed molecular structures for trimers

Following the same strategy applied for dimers, 216 trimers are generated using the brute-force algorithmic generator. Appendix Fig. B-11 to B-22 show the molecular structures of these 216 trimers. This set of trimers covers all 27 structurally unique trimers and also include 189 redundant trimers with different conformations to find the most stable conformation of each structural unique trimer. After discarding those structures with higher energy conformations, the top 9 most stable trimers are those made through 2,4'- & 2,2'-positions, 2,4'- & 2,7'-positions (+0.20 kcal/mol), 2,4'- & 7,4'-positions (+0.30 kcal/mol), 7,4'- & 7,2'-positions (+0.34 kcal/mol), 7,4'- & 2,2'-positions (+0.43 kcal/mol), 7,4'- & 7,4'-positions (+0.48 kcal/mol), 7,4'- & 2,7'-positions (+0.67 kcal/mol), 2,7'- & 4,2'-positions (+0.74 kcal/mol), and 2,2'- & 7,4'-positions (+0.95 kcal/mol). Fig. 5-4 shows the molecular structures of the top 9 most stable trimers in the order of their relative energies. These top 9 most stable trimers are made through the combinations of 2,2'-, 2,4'-, 2,7'-, and 4,7'-position.

A simple explanation is that these covalent connections are more stable according to the simulation results for dimers shown in Fig. 5-3. In Fig. 5-4, only the last trimer, which is made through 2,2'- & 7,4'-positions (Fig. 5-4i), has relative energy considerably higher than the KE. Based on the assumptions, the other 8 trimers are all likely to exist. Actually, the second most stable trimer in this work, which is made through 2,4'- & 2,7'-positions (Fig. 5-4b), has been identified by oxidation of DHI [12]. Once again, this result supports the assumption that the molecular structures with lower energies are indeed more likely to be found.

5.3.4 Proposed molecular structures for tetramers

The number of molecular structures that need to be considered increases exponentially as the oligomer size increases. 2,592 tetramers are generated from the brute-force algorithmic generator. This set of tetramers covers all 162 structural unique tetramers as well as 2,430 redundant tetramers that account for different conformations to find the most stable conformation of each structural unique tetramer. After removing the results of higher energy conformations, the systematic search of the global energy minimums for tetramers is completed. Following the same strategy, the top 9 most stable tetramers are those made through 2,4'- & 2,7'- & 2,7'-positions, 2,7'- & 2,2'- & 7,2'-positions (+0.30 kcal/mol), 2,2'- & 7,2'- & 4,2'-positions (+0.56 kcal/mol), 4,2'- & 7,7'- & 2,7'-positions (+0.91 kcal/mol), 7,2'- & 7,7'- & 2,7'-positions (+0.96 kcal/mol), 2,7'- & 2,2'- & 4,2'-positions (+1.13 kcal/mol), 4,7'- & 2,4'- & 2,2'-positions (+1.20 kcal/mol), 2,7'- & 2,4'- & 2,4'-positions (+1.35 kcal/mol), and 2,4'- & 2,7'- & 2,4'-positions (+1.77 kcal/mol). Fig. 5-5 shows the molecular structures of the top 9 most stable tetramers in the order of their relative energies. These top 9 most stable tetramers are basically made through the more stable combinations of 2,2'-, 2,4'-, 2,7'-, and 4,7'-position found in the simulation results for dimers shown in Fig. 5-3. However, a less stable covalent connection forming through 7,7'-position is also found in the 4-th and 5-th stable tetramers (Fig. 5-5d and 5-5e). This result is probably due to the existence of hydrogen bonding between the first and fourth DHI units in these two tetramers, which reduces the energy, stabilizes the structure, and improves

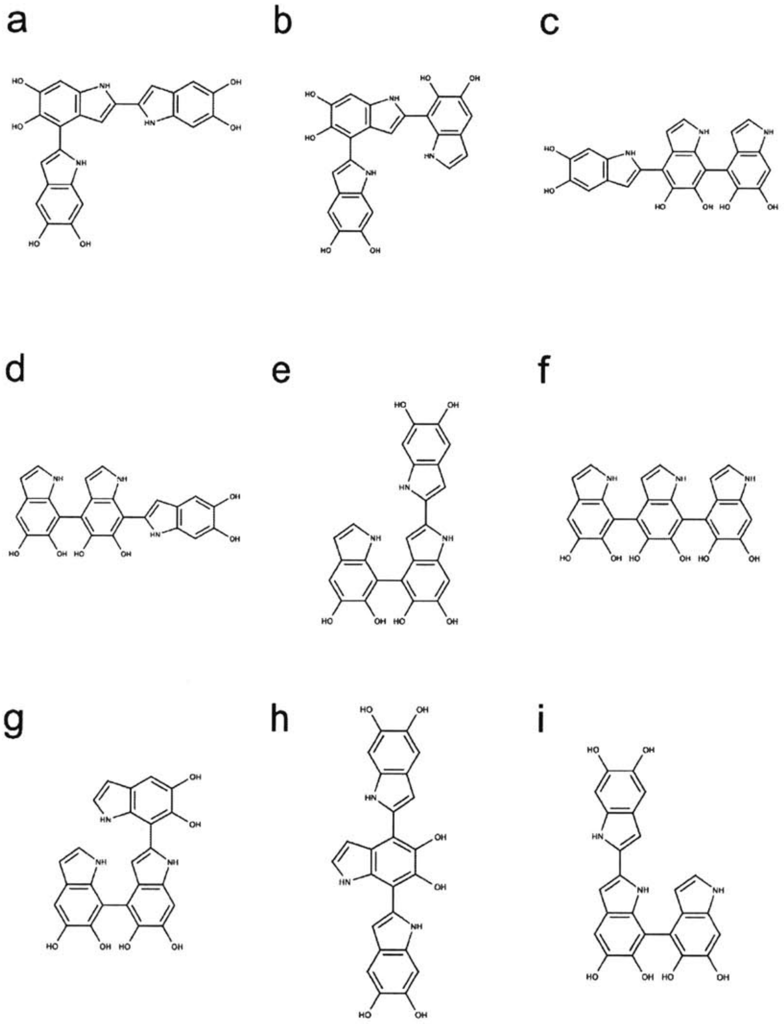

Figure 5-4: Molecular structures of top 9 most stable trimers. Those trimers are made through (a) 2,4'- & 2,2'-positions, (b) 2,4'- & 2,7'-positions (+0.20 kcal/mol), (c) 2,4'- & 7,4'-positions (+0.30 kcal/mol), (d) 7,4'- & 7,2'-positions (+0.34 kcal/mol), (e) 7,4'- & 2,2'-positions (+0.43 kcal/mol), (f) 7,4'- & 7,4'-positions (+0.48 kcal/mol), (g) 7,4'- & 2,7'-positions (+0.67 kcal/mol), (h) 2,7'- & 4,2'-positions (+0.74 kcal/mol), and (i) 2,2'- & 7,4'-positions (+0.95 kcal/mol).

their ranks. Interestingly, only the top 3 stable tetramers have relative energy lower than the KE, which implies that only a few tetramers are energetically favorable.

Evidence of porphyrin-like tetramers has been found recently in natural eumelanin pigment as well as in PDA by using electrochemical fingerprinting [98]. These tetramers, which are made through 2,7'- & 2,7'- & 2,7'-positions, create an interior ring where all the nitrogen atoms are in the center. Such arrangement is consistent with the tetrameric model proposed by Kaxiras et al. [5]. However, this particular kind of molecular structures in which a covalent bond is formed between the first and fourth DHI units is not considered in this chapter. Although these porphyrin-like tetramers are not evaluated directly, the most stable tetramer identified in this work (Fig. 5-5a), which is made through 2,4'- & 2,7'- & 2,7'-positions, shows a similar structural arrangement to these porphyrin-like tetramers.

5.3.5 Statistical characteristics

Fig. 5-6a shows the relative energies and ranks of the 216 trimers, depending on their relative energies, from the most to least stable one. Note that the relative energy increases dramatically as the rank goes up, and only a small number of trimers have a relative energy lower than or close to the KE as indicated by the red dashed line. Fig. 5-6b plots the projection products against the relative energies of all trimers. The projection product quantifies the planarity of a DHI oligomer, ranging from zero to one. A DHI oligomer with the projection product of 1.0 means it has a completely planar structure (see Appendix A.2 for details). The distribution of points in the cloud shows a trend that the projection product decreases as the relative energy increases. The result implies that those trimers with more planar molecular structures tend to have lower energy. Fig. 5-6c shows the probability of finding particular trimers in a molecular mixture of all trimers based on the Boltzmann distribution. Thus, the top 9 most stable trimers in Fig. 5-4 represent 67% of the population of all trimers. The curve is calculated with the Boltzmann distribution function shown below:

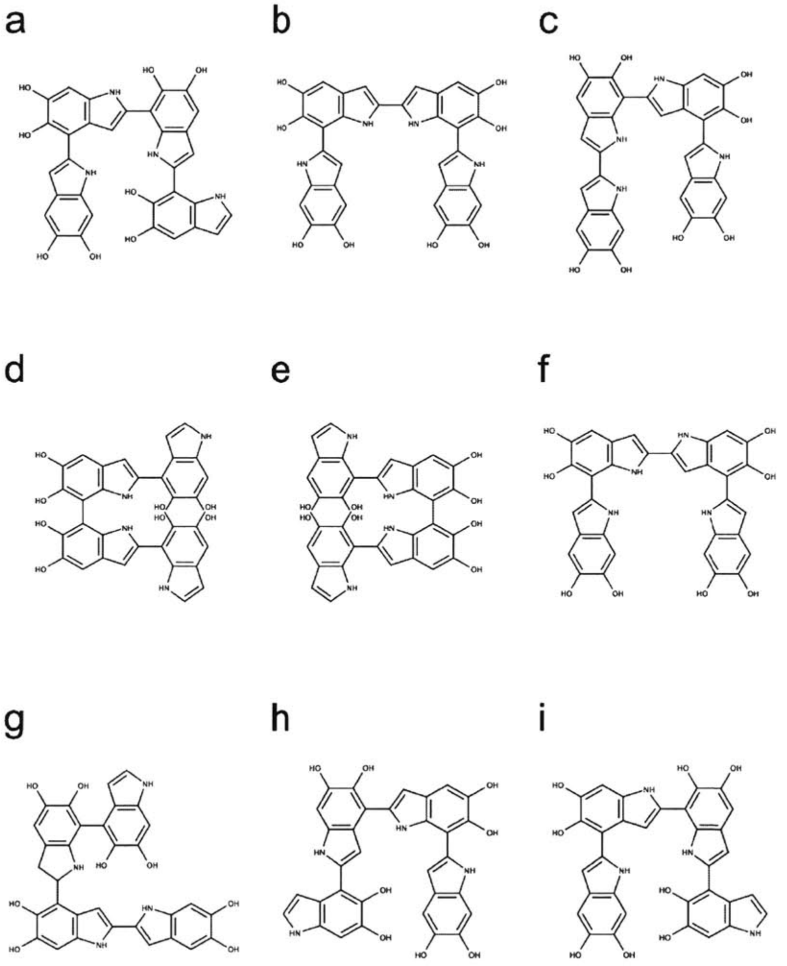

Figure 5-5: Molecular structures of top 9 most stable tetramers. Those tetramers are made through (a) 2,4'- & 2,7'- & 2,7'-positions, (b) 2,7'- & 2,2'- & 7,2'-positions (+0.30 kcal/mol), (c) 2,2'- & 7,2'- & 4,2'-positions (+0.56 kcal/mol), (d) 4,2'- & 7,7'- & 2,7'-positions (+0.91 kcal/mol), (e) 7,2'- & 7,7'- & 2,7'-positions (+0.96 kcal/mol), (f) 2,7'- & 2,2'- & 4,2'-positions (+1.13 kcal/mol), (g) 4,7'- & 2,4'- & 2,2'-positions (+1.20 kcal/mol), (h) 2,7'- & 2,4'- & 2,4'-positions (+1.35 kcal/mol), and (i) 2,4'- & 2,7'- & 2,4'-positions (+1.77 kcal/mol).

$$p_n = \frac{\sum_{i=1}^{n} \exp\left(-\varepsilon_i/kT\right)}{\sum_{i=1}^{m} \exp\left(-\varepsilon_i/kT\right)} \tag{5.1}$$

where p_n is the probability of finding the molecular structures that are made of the top n most stable molecules, the term m is the total number of molecules, the term ε_i is the energy (relative energy is adopted) of the molecule i, the term k is the Boltzmann constant, and the term T is the temperature (300 K).

Fig. 5-6d shows the relative energies and ranks of the 2,592 tetramers. Note that the relative energy increases much more dramatically in the beginning compared to that in the case of trimers (Fig. 5-6a). The inner figure in Fig. 5-6d zooms in the relative energies of the top 20 ranked tetramers. Only very few tetramers have relative energies lower than 1.0 kcal/mol, which is about two times of the KE. Consequently, even though there are 162 structural unique tetramers, the majority species of tetramers in eumelanin and PDA could be only a few. A possible explanation is that there are higher energy barriers for adding DHI monomer to larger oligomers. For example, when a new monomer is trying to add to a trimer to form a tetramer, it is not only interacting with the terminal monomer to which it is attaching but also interacting with the other two monomers via non-covalent interactions. Therefore, the degree of freedom for a new monomer to approach an oligomer is decreased as the number of DHI units in the oligomer is increased based on steric effects. This result can explain the existence of relatively small degrees of polymerization in eumelanin and PDA. Fig. 5-6e shows the projection products and relative energies of all tetramers. The figure shows a trend that more planar tetramers have lower relative energy. As a result, more planar tetramers are more stable and more likely to exist compared to less planar tetramers. This finding agrees with the fact that eumelanin and PDA are composed of near planar oligomers. Note that only if the oligomers are near planar, layered aggregates made of stacked oligomers via π-π interactions can be observed in experiments [10, 40]. Furthermore, as discussed in Chapter 3, only if the oligomers can stack together closely to form the secondary structures, the

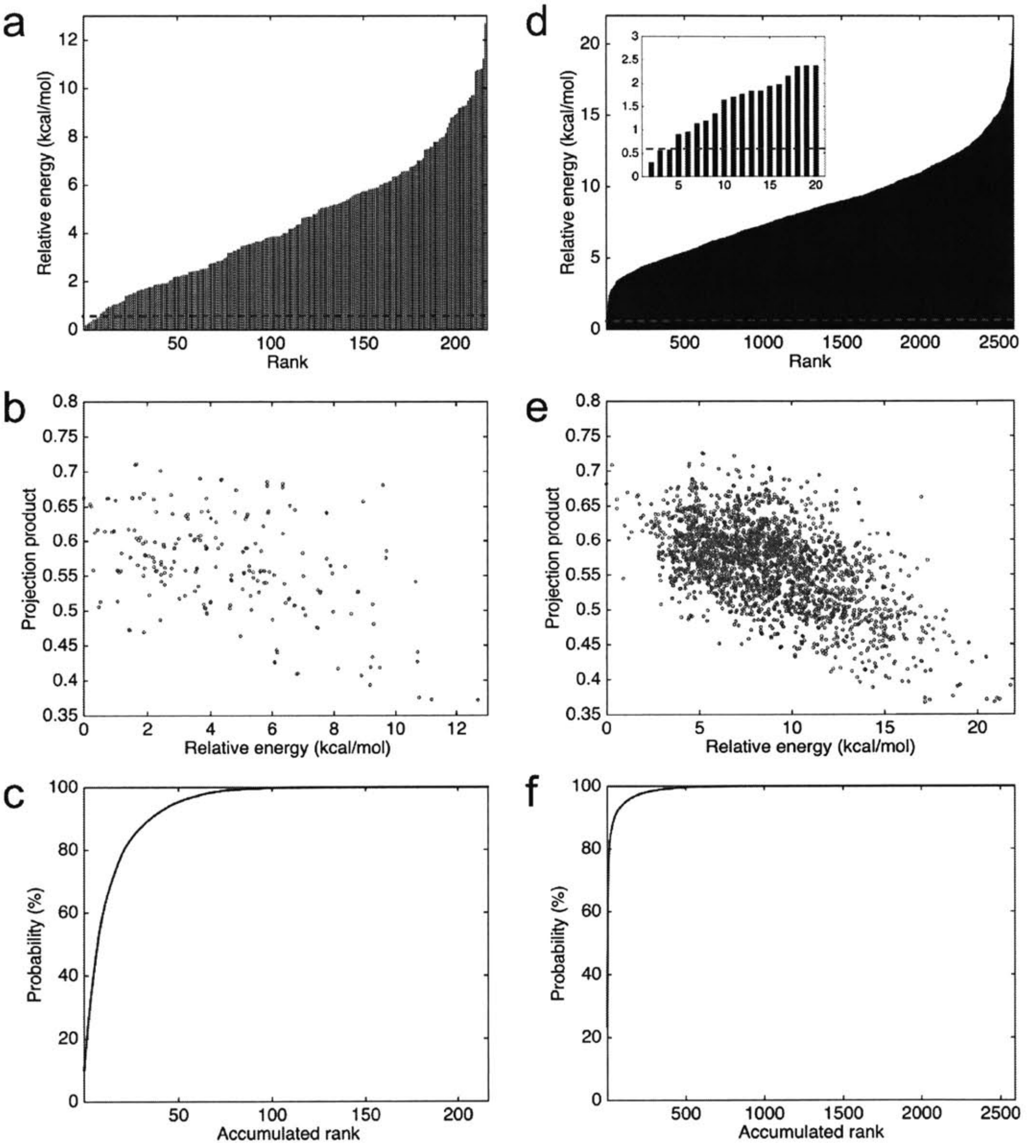

Figure 5-6: Statistical characteristics of data for trimers and tetramers. (a) Relative energies and ranks of 216 trimers, depending on their relative energies, from most to less stable one. The red dashed line indicates the thermal energy (KE), which is 0.593 kcal/mol at room temperature. (b) Projection products against relative energies of all trimers. (c) Cumulative Boltzmann distribution function for all trimers. (d) Relative energies and ranks of 2,592 tetramers, depending on their relative energies, from most to less stable one. The inner figure zooms in the relative energies of the top 20 tetramers. The red dashed lines indicate the thermal energy (KE). (e) Projection products against relative energies of all tetramers. (f) Cumulative Boltzmann distribution function for all tetramers.

excitonic effects among the oligomers will be strong enough to produce the broadband absorption spectrum of eumelanin [9]. Fig. 5-6f shows the probability of finding certain tetramers in a molecular mixture of all tetramers. Based on the Boltzmann distribution, the top 9 most stable tetramers shown in Fig. 5-5 represent 77% of the population of all tetramers. This result suggests that the majority species of tetramers could be quite repetitive even though the number of probable tetramers is large.

5.3.6 Self-assembly of tetramers

Fig. 5-7a shows the DFT optimized geometry of the most stable tetramer (Fig. 5-5a). This tetramer has not only the lowest energy compared to the others but also a high projection product of 0.68 (Fig. 5-6e). While eight of the tetramers are placed in a simulation box, they quickly stack together to form a layered aggregate during the simulation shown in Fig. 5-7b (see Methods section for details). This kind of layered aggregates is one of the most important structural features of eumelanin-like materials. Note that only planar tetramers can form such aggregated structures. For example, Fig. 5-7c shows the DFT optimized geometry of the tetramer with the lowest projection product of 0.37 (Fig. 5-6e). Interestingly, this tetramer is also one of the least stable tetramers, which ranks 2,588 of 2,592. While eight of the tetramers are placed in a simulation box, they also quickly aggregate together during the simulation. However, they do not stack together to form a layered aggregate. Instead, they form an amorphous structure shown in Fig. 5-7d. This result clearly demonstrations that choosing more realistic molecular models of eumelanin and PDA for simulations is crucial to get meaningful results.

5.4 Conclusions

A set of computational modeling methods is proposed to generate and evaluate probable molecular structures of eumelanin and PDA systematically. The most reactive positions in a DHI monomer are identified. For the first time, a first principles ap-

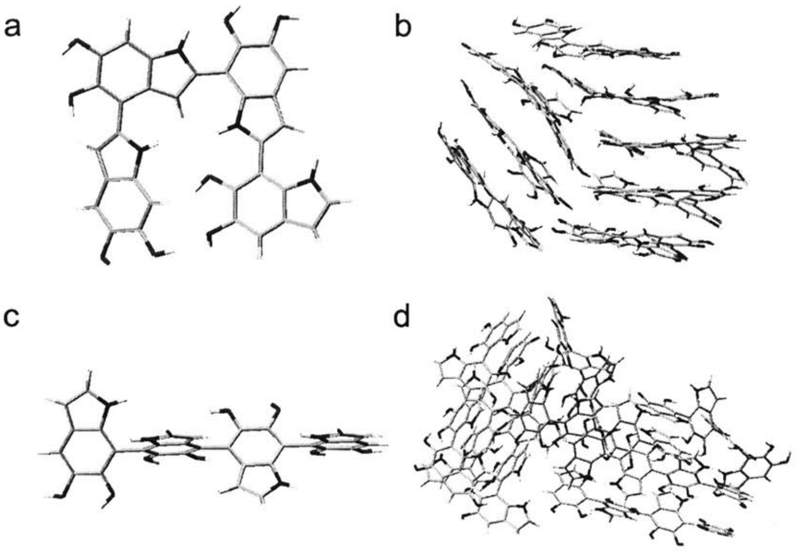

Figure 5-7: Molecular and aggregated structures of most and least stable tetramers. (a) Molecular structure of most stable tetramer. (b) Layered aggregate formed by eight of most stable tetramers shown in (a). (c) Molecular structure of least stable tetramer. (d) Amorphous aggregate formed by eight of least tetramers shown in (c).

proach is used to provide a quantum-chemical explanation of the existence of certain preferential connections between DHI monomers. These results are then used as an input for the brute-force algorithmic generator that creates all probable chemical isomers for DHI oligomers. From a total number of nearly 3,000 isomers, the most stable dimers, trimers, and tetramers of DHI are identified, to propose molecular models that will aid more accurate modeling of eumelanin and PDA. The relative energies between molecular models reported in this work can be applied to estimate a proper ratio of these molecules in simulations. In addition, fundamental explanations of some important structural features of eumelanin and PDA, such as the structural planarity and small size of oligomers, are provided in this work. It is important to remark that this chapter only evaluates DHI oligomers up to tetramers, and does not consider different redox forms, due to computational limitations. However, the theoretical framework described here and the brute-force algorithmic generator presented in this chapter can be easily applied to larger DHI oligomers and different redox forms of DHI in future studies.

Chapter 6

Graphene oxide – polydopamine nanocomposites

This chapter presents a description of the publication, Chun-Teh Chen, Francisco Martin-Martinez, Shengjie Ling, Zhao Qin, and Markus J. Buehler. Bio-inspired Graphene oxide – polydopamine nanocomposite with enhanced mechanical strength and shrinking ability (*in preparation*).

6.1 Introduction

Creating composite materials with high mechanical properties and multi-functionalities is an ultimate goal towards superior engineering applications. Graphene is one of the most promising candidates for developing such new materials due to the remarkable high mechanical strength and electrical conductivity that arise from its two-dimensional sp^2 carbon atoms' honeycomb structure. A defect-free graphene has been proven the strongest known material with a tensile strength of 130 GPa [99], which is about 200 times stronger than steel. Despite this potential, graphene still has a long way to go before it reaches large-scale commercial utilization since it is considerably expensive and difficult to be produced in mass quantity. An alternative material for certain applications is GO, for which a homogeneous colloidal suspension can be readily prepared in aqueous media for versatile mass production and further treatment. GO has rich oxygen-containing functional groups including epoxy and hydroxyl groups on its graphene basal plane and carboxylic groups along the edges. Consequently, GO sheets are hydrophilic and can be quickly dispersed in water under mild ultrasonic treatment [100]. Although the strength of GO (63 GPa) [101] is weaker than that of graphene, it is still much stronger than conventional engineering materials. The applications of GO are limited due to the small size of GO sheets, which is on the scale of micrometers. Assembling GO sheets into so-called GO paper consisting of several hundred layered GO sheets in the thickness direction and with the size up to a few centimeters in the in-plane directions, is essential for expanding the range of applications of GO. However, after the assembly, the strength of GO paper (76-293 MPa) [102, 103, 104, 105, 106, 107, 108] is much inferior to that of an individual GO sheet. The reason for this relative weakness relies on the weak interlayer interactions provided by a hydrogen-bonding network formed between oxygen-containing functional groups on adjacent GO sheets and water molecules. The interlayer interactions are not strong enough to hold GO sheets together during stretching. As a result, the failure mechanism of GO paper is sliding of adjacent GO sheets but not breaking of strong carbon-carbon bonds on its graphene basal plane, which is the source of the strength in graphene and GO sheets.

To improve the mechanical properties of GO paper, one strategy is to increase interlayer interactions. PDA is a suitable candidate to achieve this mechanical reinforcement. Utilizing its outstanding adhesive ability, PDA can be used as an efficient mechanical reinforcing agent. In addition to this, PDA also plays a role as a reducing agent due to its oxidative self-polymerization ability. In the case of GO paper, this oxidative process implies the reduction of GO, which is of interest due to the enhanced electrical conductivity arising from the reduction. Graphene has extremely high electrical conductivity, but GO is a near electrical insulator due to the disruption of its sp^2 bonding. Consequently, a reduction process is desirable to recover its electrical conductivity. Among common reduction methods, the hydrazine-based reduction is one of the alternatives. However, it is less desirable to be applied to mass production because of its high toxicity. In addition to this, high-temperature annealing techniques may deteriorate the well-stacked paper structure and lead to a decrease in the mechanical properties. On the contrary, beyond enhancing the strength of composite materials, PDA is also able to reduce GO to reduced-GO (rGO) and provide a versatile, functional route for further derivation. As a result, PDA can be an alternative to the hazardous hydrazine for deoxygenation of GO. Recent research efforts have been devoted to embedding PDA to GO paper to produce so-called GO–PDA paper with enhanced mechanical properties and electrical conductivity [106, 107, 108].

In addition to GO–PDA paper, other types of GO-based paper have also been fabricated for achieving higher mechanical properties, such as GO-poly(vinyl alcohol) (PVA) paper [64, 109, 110], and GO-poly(methyl methacrylate) (PMMA) paper [109]. However, what makes GO–PDA paper unique is that it does not only provide better mechanical properties compared to GO paper but also brings additional functionalities. Besides enhancing the electrical conductivity already mentioned above, another fascinating function that GO–PDA paper exhibits is the humidity-caused self-folding ability. Most materials swell during wetting and shrink during drying. It is typical behavior, especially for porous materials such as wood and clay, since the volume expands while water molecules fill the porous space and shrink while water molecules are removed. For non-porous materials, the swelling/shrinking mechanism is much more complicated. GO–PDA paper, a non-porous 2-D material, has been found to absorb water rapidly to swell and lose water to shrink. Accordingly, GO–PDA paper is a highly efficient actuator and has been fabricated as a humidity sensor [111], worm-like walking device [34, 111], self-folding box [34], robotic hand [34], and micro robot [34]. Although the physicochemical properties of GO–PDA paper have been widely studied in experiments, some fundamental questions regarding the reduction mechanism that transforms GO to rGO, the detailed molecular structure of the GO–PDA paper, the source of the enhanced mechanical strength, and the shrinking/swelling mechanism of its 2-D layered structure are still unclear. Most previous studies on GO–PDA paper were based on empirical approaches instead of a solid framework of structure–function relationships. In this chapter, a computational study of GO–PDA paper is reported to elucidate some of these fundamental questions.

6.2 Methods

6.2.1 GO and GO–PDA models

In this chapter, GO sheets with an empirical formula of $C_{12}O_2(OH)$ are created. This 4:1 carbon-to-oxygen ratio is commonly found in experiments [112, 113]. Two different sizes of GO and GO–PDA models are generated: small-scale and large-scale. The small-scale GO and GO–PDA models consist of four GO or GO–PDA sheets with a dimension of 50 Å by 100 Å; the large-scale GO and GO–PDA models also consist of four GO or GO–PDA sheets but with a dimension of 50 Å by 1,000 Å.The initial interlayer spacing is set to 45 Å to prevent interactions between adjacent GO or GO–PDA sheets in the initial configuration. Hydroxyl and epoxide groups are randomly added on either side of the graphene basal plane. Five different amounts of water (e.g., 0 wt%, 8 wt%, 15 wt%, 27 wt%, and 35 wt%) are added to the small-scale GO and GO–PDA models, to study water effects on the structural and mechanical properties. The water content in a model is calculated by $M_{water}/(M_{GO} + M_{water})$, where M_{water} is the mass of water and M_{GO} is the mass of GO. Note that the molecular structure of PDA is still controversial even after significant experimental and theoretical efforts over past years. This chapter only considers DHI, the fundamental building block of PDA, to simplify the problem. Based on the DFT calculations (see Results and discussion section for details), the most stable structure is adopted to generate GO–PDA models. The only difference between the GO and GO–PDA models is the existence of DHI units in the GO–PDA models. These DHI units are randomly added on either side of the graphene basal plane in the GO–PDA models. The mass ratio of DHI units in the GO–PDA models is about 23 wt% in the dry condition.

6.2.2 Atomistic modeling and equilibration

Full atomistic MD simulations are implemented using LAMMPS [57] with ReaxFF, which is a first principle-based general bond-order dependent force field that provides a description of bond breaking and bond forming [4]. The existing version of

ReaxFF for hydrocarbons described by van Duin et al. [4] and extended to hydrocarbon oxidation by Chenoweth et al. [114] is adopted in this chapter. This version of ReaxFF has been widely applied for studying graphene oxidation and GO-based materials [63, 64, 115]. However, to simulate GO–PDA paper, force field parameters for nitrogen–carbon–hydrogen are required. The force field parameters for nitrogen–carbon–hydrogen in the study of Kamat et al. [116] are also adopted in this chapter. These parameters were optimized against quantum and experimental data and can reproduce the physical and chemical reactions between nitrogen–carbon and nitrogen–nitrogen [116], as well as the complex chemistry involved in char combustion [117].

After energy minimization with the CG algorithm, the GO and GO–PDA models are first simulated with the NPT ensemble at a constant temperature of 10 K and pressure of 1.013 bar in the X and Y directions, and 1,013 bar in the Z direction for 100 ps. The low temperature in the simulations prevents the water molecules from forming water clusters, and the high pressure in the Z direction allows the GO and G-PDA sheets to form layered nanocomposites much faster than at low pressures. The MD models are then simulated in the NPT ensemble at a constant temperature of 300 K and pressure of 1.013 bar in all directions for another 100 ps. PBCs are applied in all directions for these two steps of MD simulations. The interlayer spacing of the MD models is calculated after the second step of MD simulations is finished.

The small-scale GO and GO–PDA models are used to study the mechanical strength of GO and GO–PDA paper. The equilibrium structures obtained from the MD equilibrations described above are adopted in pulling tests for evaluating their mechanical strength. To perform pulling tests to simulate the tension-shear behavior, the PBC in the pulling direction (Y direction) is eliminated by adding a vacant space with the length of 20 Å. The left edges of the first and third sheets and the right edges of the second and fourth sheets are fixed during pulling tests. These edges are only fixed in the Y direction and are free to move in the other two directions. During pulling tests, the simulation boxes are stretched in the Y direction at around 1.25% every 25 ps. The stress is derived from the center region with a length of 50 Å to limit the effects of the boundaries and averaged over a time interval of the last 5.0 ps in each pulling step to reduce stress fluctuations.

The large-scale GO and GO–PDA models are used to study of the shrinking ability of GO and GO–PDA paper. The large-scale GO and GO–PDA models in a wet condition (35 wt%) is equilibrated with the MD equilibrations described above. The water molecules in the models are then removed to simulate the dehydration progress. The models are simulated in the NPT ensemble at a constant temperature of 400 K and pressure of 1.013 bar in all directions for 1.0 ns. The high temperature accelerates the equilibration speed in the simulation, thus reducing the simulation time for the equilibration. In the final step, the GO–PDA model is then simulated in the NPT ensemble at a constant temperature of 300 K and pressure of 1.013 bar in all directions for 100 ps. The stresses measured in the pulling tests are averaged over a time interval of each 25 ps to reduce stress fluctuations.

6.3 Results and discussion

6.3.1 Proposed reactions between DHI and GO

The investigation in this work starts with DFT calculations to find the most probable chemical reactions between DHI and GO (see Methods section in Chapter 5 for details). Note that the chemical reaction mechanism between DHI and GO is a complex process that goes beyond the scope of this work. GO contains three main oxygen-containing functional groups, namely epoxy, hydroxyl, and carboxylic groups. Epoxy group is known to be especially reactive, and therefore we consider this one as the most probable reaction site on GO. In the first approach, assuming that the chemical reaction occurs between an epoxy group on a GO flake and DHI. As a result, a new covalent bond is added to connect an epoxy group on a GO flake and DHI. One of the possible initial structures is shown in Fig. 6-1a. After the system is relaxed with DFT geometry optimization, all possible connections explored converge to a non-binding structure such as the one shown in Fig. 6-1b. These structures might imply the extraction of an oxygen atom from the GO flake, which leads to a possible

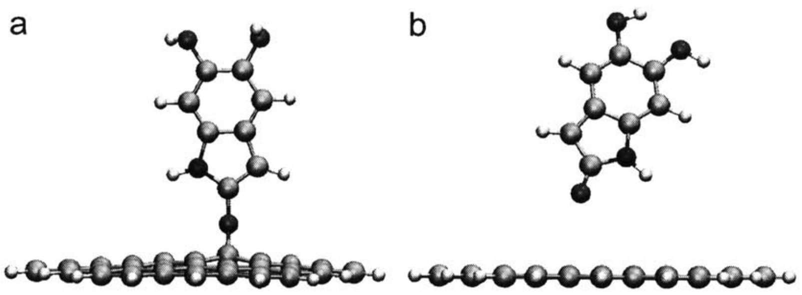

Figure 6-1: Bonding of epoxy group on GO flake and DHI. (a) Initial geometry of one of possible bonding sites. (b) Converged geometry in which oxygen is removed and GO is reduced to rGO.

reduction process from GO to rGO, in agreement with the experimental observation of PDA-driven GO reduction.

In the second step, assuming that the chemical reaction occurs between a carbon atom on a GO flake and DHI. Four different systems that cover the possible reactive positions for this connection are explored. Unlike the previous case in which the connection is made to an oxygen atom, these four systems converge to bonded structures. The optimized geometries and relative energies of these four systems compared to the lowest energy system are shown in Fig. 6-2. The most stable structure (Fig. 6-2d) from these results is then adopted for generating the GO–PDA models.

6.3.2 Interlayer spacing of GO and GO–PDA paper

Due to the computational limitation, the length-scale of GO and GO–PDA models in MD simulations cannot match the real size of these materials in experiments, which is usually on a scale of several micrometers in the thickness direction and a few centimeters in the in-plane directions. As mentioned in Methods section, the small-scale GO and GO–PDA models consist of four GO or GO–PDA sheets with a dimension of 50 Å by 100 Å. Similar models were used to study GO and GO-PVA paper in the work of Compton et al. [64]. Fig. 6-3 shows the snapshots of the GO and GO–PDA models with different water content after the MD equilibrations (see Methods section for details).

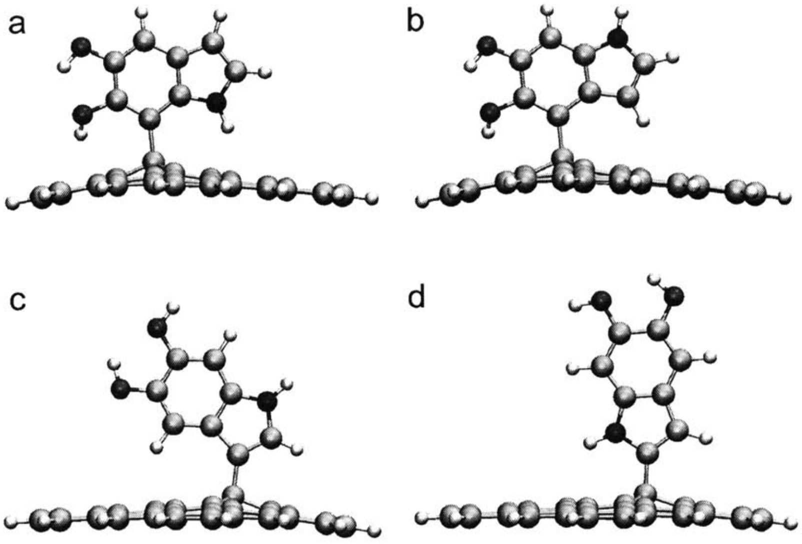

Figure 6-2: Bonding of carbon atom on GO flake and DHI. Four different systems for this connection are explored. The relative energies with respect to the most stable structure in (d), are +16.52 kcal/mol for structure in (a), +19.51 kcal/mol for structure in (b), and +5.94 kcal/mol for structure in (c).

Fig. 6-4 shows that the interlayer spacing of GO models are 5.35 Å, 5.83 Å, 6.28 Å, 7.19 Å, and 8.10 Å, corresponding to the water content of 0 wt%, 8 wt%, 15 wt%, 27 wt%, and 35 wt%, respectively. The interlayer spacing of the GO models increases as the water content increases. The result is consistent with previous computational studies [63, 64], but smaller than experimental measurements (7.6–9.7 Å) [102, 106, 107, 108, 118, 119]. The reason for this mismatching comes from the difficulty of archiving low-water containing GO paper in experiments. GO paper is synthesized in water solution; thus it contains a large amount of water in between GO sheets when it is produced. Even after dehydration, there is still an approximately one-molecule-thick layer of water tightly bonded to GO sheets via hydrogen bonding. This water monolayer is extremely difficult to remove without damaging GO paper [120]. Consequently, the GO models in the dry (0 wt%) and near-dry (8 wt%) conditions, which have much smaller interlayer spacing, are unlikely to be observed in experiments. On the other hand, the GO models in wet (15 wt%, 27 wt% and 35 wt%) conditions are closer to the actual interlayer spacing of GO paper in

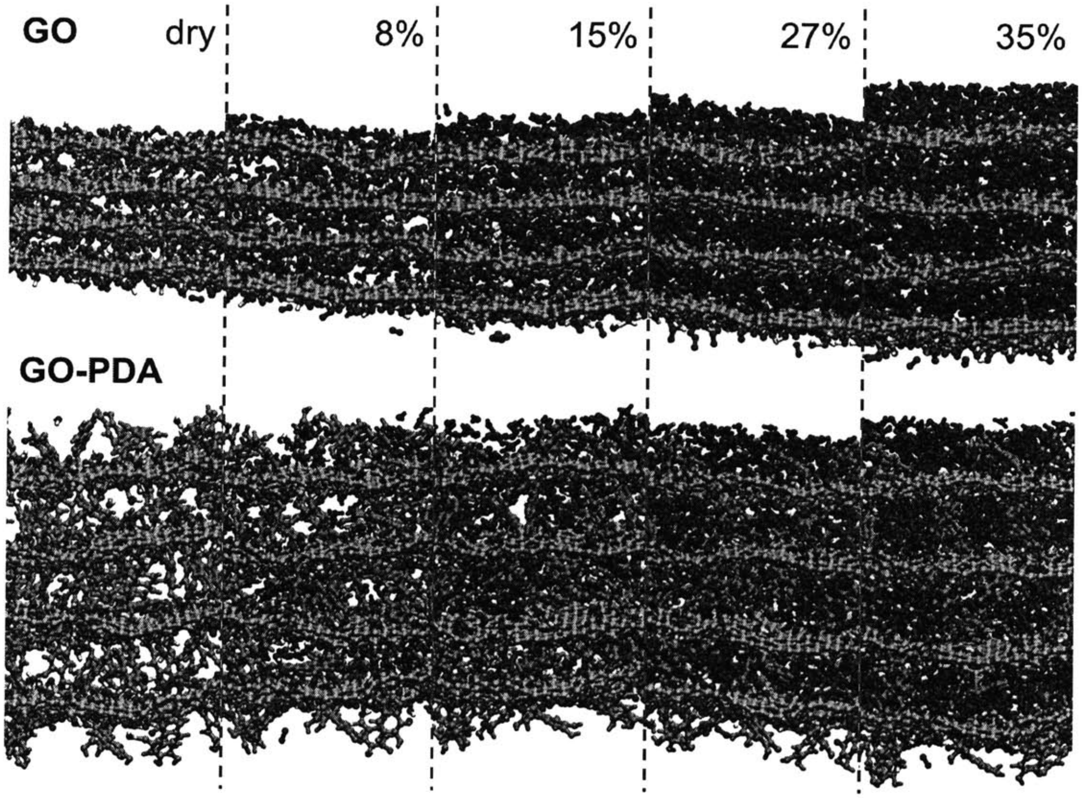

Figure 6-3: Snapshots of GO and GO–PDA models with different water content (e.g., 0 wt%, 8 wt%, 15 wt%, 27 wt%, and 35 wt%).

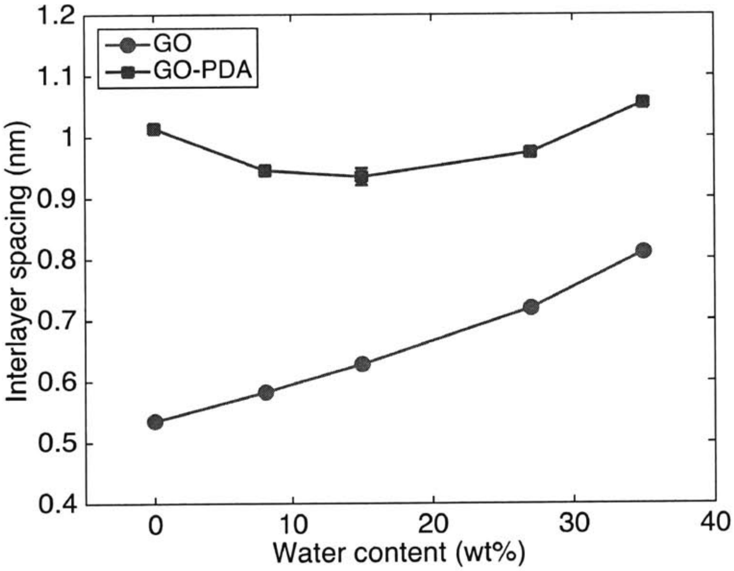

Figure 6-4: Interlayer spacing of GO and GO–PDA models with different water contents (e.g., 0 wt%, 8 wt%, 15 wt%, 27 wt%, and 35 wt%).

experiments.

In the GO–PDA models, the interlayer spacing is 10.14 Å, 9.45 Å, 9.34 Å, 9.74 Å, and 10.55 Å, corresponding to the water content of 0 wt%, 8 wt%, 15 wt%, 27 wt%, and 35 wt%, respectively. The result is consistent with experimental measurements (9.5–10.3 Å) [106, 107, 108]. Compared to the GO models, the interlayer spacing of the GO–PDA models is less sensitive to water content (Fig. 6-4). Unlike GO models, for which the interlayer spacing increases monotonically as the water content increases, the interlayer spacing of GO–PDA models decreases when a small amount of water (8 wt% and 15 wt%) is added. In dry condition, the oxygen-containing functional groups on adjacent GO–PDA sheets cannot interact with each other due to the large interlayer spacing, which is presumably caused by the existence of DHI units (Fig. 6-3). When a small amount of water is added, there is sufficient space between GO–PDA sheets for hosting water molecules without increasing the interlayer spacing. Furthermore, these water molecules act as bridges that form hydrogen bonds with the oxygen-containing functional groups on adjacent GO–PDA sheets; thus, these water molecules pull adjacent GO–PDA sheets closer. However, once a large amount of water (27 wt% and 35 wt%) is added, there is no space available between GO–PDA sheets for hosting additional water molecules. As a result, the interlayer spacing has to increase to enable additional water storage.

6.3.3 Mechanical strength of GO and GO–PDA paper

The small-scale GO and GO–PDA models used to study the interlayer spacing are adopted to estimate the mechanical strength. As mentioned before, the failure mechanism of GO-based papers is mainly the sliding of adjacent sheets. Therefore, the adhesive strength between adjacent sheets determines the strength of the material. To estimate the adhesive strength between adjacent sheets, constant tensile strains are applied to pull the first and third sheets to the right and the second and fourth sheets to the left in the simulations (Fig. 6-5a). Only the stresses in the center regions of the models are measured during the pulling tests to eliminate the boundary effects (Fig. 6-5a). This kind of mechanical behavior can also be described with analytical models, such as tension-shear (TS) or deformable tension-shear (DTS) models if all required parameters are known [121]. Based on the pulling test results shown in Appendix Fig. B-23 and B-24, the adhesive force provided by the GO and GO–PDA models with different water content are shown in Fig. 6-5b. In the figure, the adhesive force increases in the GO and GO–PDA models as the water content increases mainly due to the existence of more hydrogen bonds provided by water molecules. Furthermore, the adhesive force of the GO–PDA models is higher than that of the GO models with the same water content. This result is due to the additional adhesive force provided by DHI units in the GO–PDA models. Fig. 6-5c shows the adhesive strength of the GO and GO–PDA models with different water content based on the pulling test results shown in Appendix Fig. B-23 and B-24. In the dry (0 wt%) condition, the GO model is stronger than the GO–PDA model. However, when a small amount of water (8 wt% and 15 wt%) is added, the GO–PDA model has similar adhesive strength compared to the GO model. When more water (27 wt% and 35 wt%) is added, the GO–PDA model becomes stronger than the GO model. Unlike the adhesive force, the adhesive strength of the GO–PDA models is not always higher

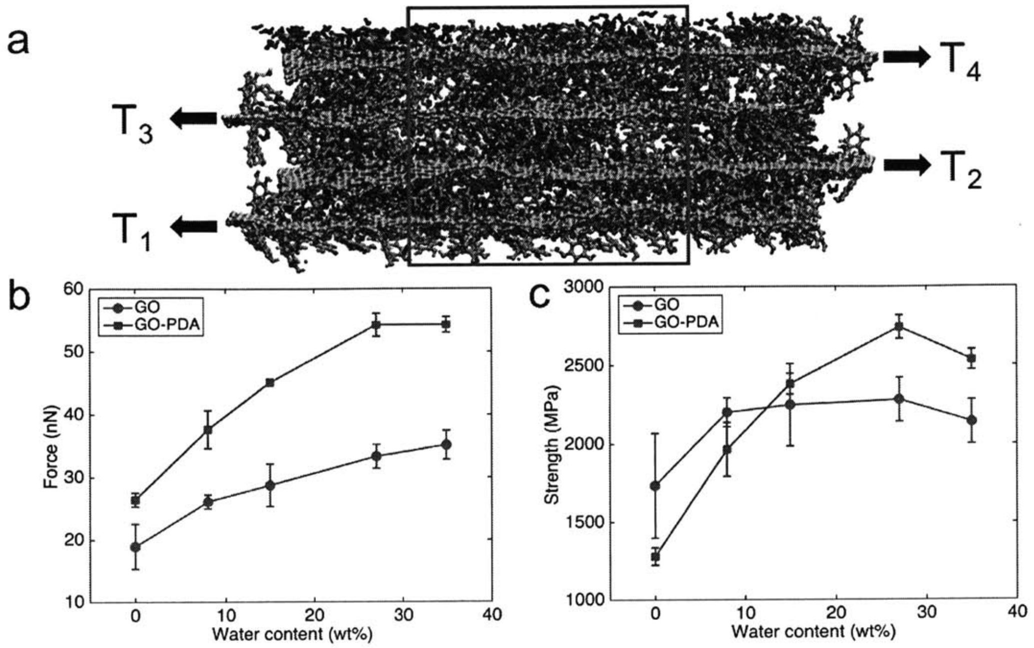

Figure 6-5: Pulling tests on GO and GO–PDA models. (a) Snapshot of GO–PDA model with 15 wt% water content during pulling test. The stress is derived from the center region (red box) with a length of 50 Å to eliminate the boundary effects. (b) Adhesive force provided by GO and GO–PDA models with different water content. (c) Adhesive strength provided by GO and GO–PDA models with different water content. The simulation results are the averaged results obtained from three sets of the GO and GO–PDA models, which are created with different random distributions of hydroxyl and epoxide groups and DHI units.

than that of the GO models with the same water content. The GO–PDA models have larger interlayer spacing compared to the GO models (Fig. 6-4). The adhesive strength is defined as the adhesive force divided by the cross-section area, and larger interlayer spacing means a larger cross-section area. As mentioned above, GO paper in the dry (0 wt%) and near-dry (8 wt%) conditions is unlikely to be observed in experiments. Consequently, based on the simulation results, GO–PDA paper should be stronger than GO paper in normal conditions.

Since the size of GO and GO–PDA models is much smaller than the real size of these materials in experiments, there are some intrinsic differences between simulations and experiments. Unlike the small GO and GO–PDA sheets in the simulations, larger GO and GO–PDA sheets are difficult to stack perfectly to form GO or GO–

PDA paper in experiments. Therefore, wrinkled and rippled structures are often observed experimentally in a GO-based material but are absent in the simulations. In addition, to simplify the problem, defects are not considered in this work; while defect-free GO and GO–PDA paper do not exist in the real world, one should be aware of the fact that defects can significantly reduce the mechanical properties of materials. Consequently, the adhesive strength predicted in the simulations is much higher than experimental measurements. In this regard, this work does not aim to reproduce the exact mechanical strength of GO and GO–PDA paper in the macroscale but rather to describe the interactions between GO and PDA at the nanoscale for understanding the source of improved mechanical strength.

Moreover, some experimental studies on GO–PDA paper suggest that the enhanced mechanical strength of GO–PDA paper comes from covalent cross-links between adjacent sheets when embedding PDA [108]. Although it seems like a rational explanation, since covalent cross-links are much stronger than hydrogen bonds, there is no clear evidence showing that covalent cross-links are formed in GO–PDA paper. In fact, even though this work does not include any covalent cross-link in the GO–PDA models, higher adhesive strength is still observed compared to the GO models in the simulations. Furthermore, it was found that the mechanical strength of GO–PDA paper is about 35% stronger than that of GO paper [107], which is in good agreement with the simulation results (Fig. 6-5c). Therefore, even though there are cross-links formed between adjacent GO–PDA sheets, the ratio might be negligible. A possible explanation for this behavior is that as DHI monomers form covalent bonds with GO sheets, they get fixed to the GO sheets, limiting their mobility and ability for further reaction. As a result, as two GO–PDA sheets stack together, the probability for the DHI monomers on the adjacent sheets to reach each other and react to form cross-links should be low.

6.3.4 Shrinking ability of GO and GO–PDA paper

The shrinkages of GO and GO–PDA models during dehydration in simulations are less than 1%. To show that this value does not correspond to a numerical error associated with the size of the model, the large-scale GO and GO–PDA models are used for this study (see Methods section for details). The large-scale GO and GO–PDA models are first equilibrated in a wet condition with the water content of 35 wt% and then equilibrated in the dry (0 wt%) condition where the water molecules are removed. Two different boundary conditions are applied to simulate a relaxed and fixed boundary situations to study actual shrinking and associated stress, respectively. In the relaxed condition, the GO and GO–PDA models can freely shrink or swell to relax the internal stresses. Accordingly, the amount of shrinkage or swelling can be observed and measured in the simulations. In the fixed condition, the lengths of GO and GO–PDA models are fixed after the water molecules are removed, and the stresses associated to shrinkage/swelling can be calculated. The changes in the lengths and stresses of the GO and GO–PDA models during dehydration in the relaxed and fixed boundary conditions are shown in Fig. 6-6. In the GO model, a shrinkage of 0.1% in the in-plain longitudinal direction and corresponding shrinking stress of around 200 MPa are measured. In the GO–PDA model, the shrinking stress is similar to that of GO model, which is around 200 MPa. However, the shrinkage in the GO–PDA model (0.6%)is much larger than that of GO model (0.1%). The result is in good agreement with experiments showing that GO–PDA paper shrinks more than GO paper during dehydration [34].

The snapshots of the GO–PDA model in the wet and dry conditions are shown in Fig. 6-7. In the wet condition (6-7a), the DHI units on the GO–PDA model are surrounded by the interlayer water molecules. As a result, the DHI units have low probability to interact with each other, and they stay in their positions while interacting with the water molecules. On the contrary, in the dry condition (Fig. 6-7b), the DHI units interact with each other since the water molecules are removed. Nevertheless, these DHI units have a low mobility compared to water molecules since they are fixed on the graphene basal plane; thus they generate nonuniform stresses on the graphene basal plane when they interact with each other. These nonuniform stresses ripple the GO–PDA model and shrinks the length.

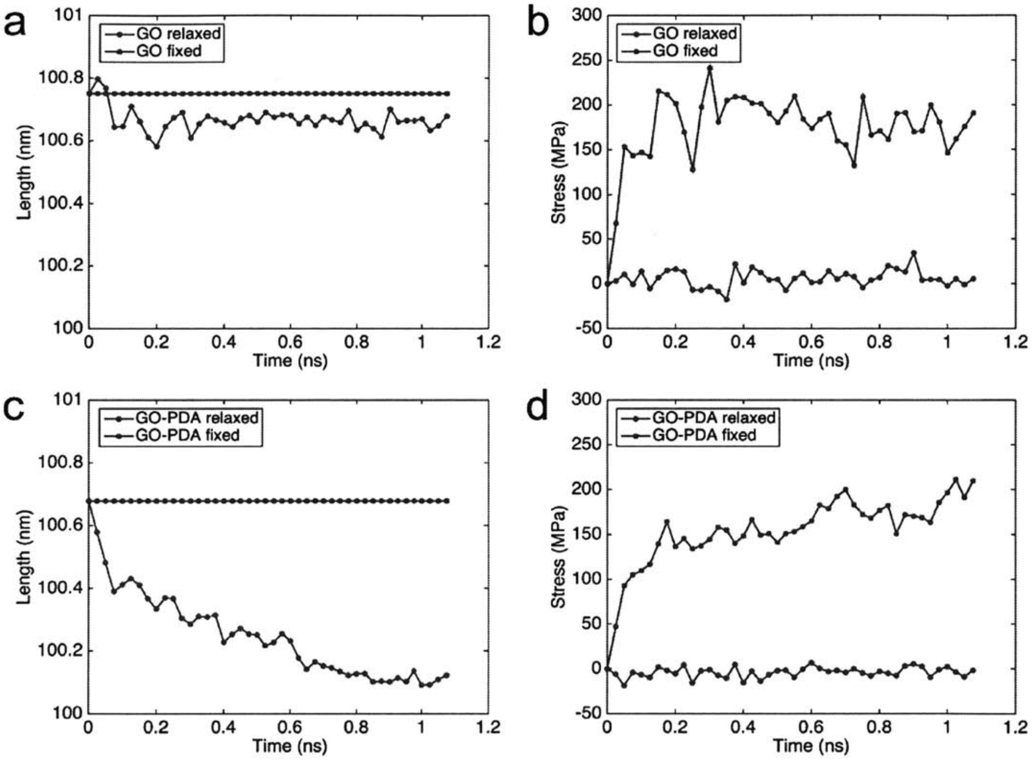

Figure 6-6: Changes of lengths and stresses of GO and GO–PDA models during dehydration. (a) Changes of length of GO model. (b) Changes of stress of GO model. (c) Changes of length of GO–PDA model. (d) Changes of stress of GO–PDA model.

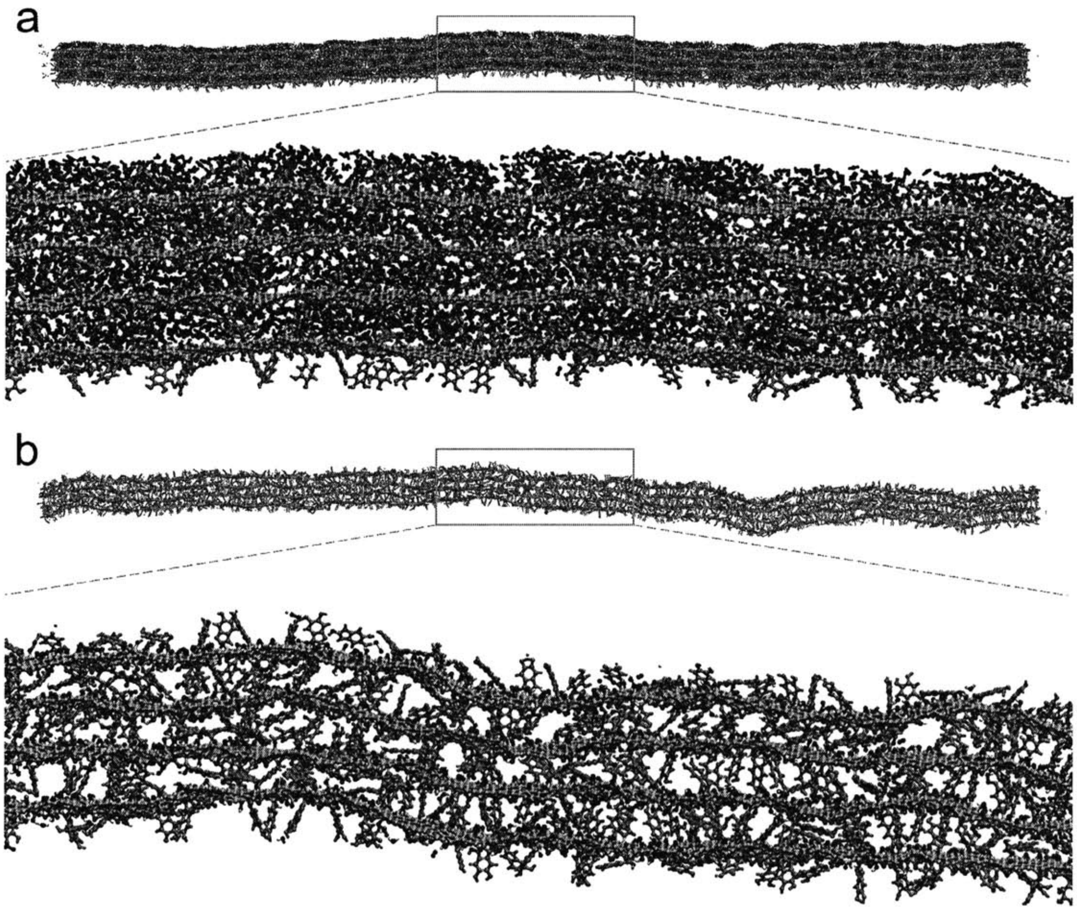

Figure 6-7: Snapshots of GO–PDA model in wet and dry conditions.

6.4 Conclusions

Numerous GO-based nanocomposites are fabricated to achieve improved mechanical properties in experiments. GO–PDA paper has been shown with improved mechanical strength, electrical conductivity, and shrinking ability. In this chapter, probable chemical reaction mechanisms between DHI and GO are proposed, which might explain the chemical reduction ability of PDA to reduce GO to rGO and how DHI monomers attach to GO. The simulated pulling tests reveal that the enhanced strength of GO–PDA might merely come from the additional non-covalent interactions provided by PDA, and not from covalent cross-linking that was suggested from other studies. This finding implies an opportunity to increase the mechanical properties of GO–PDA paper further if a large amount of covalent cross-linking can form to connect GO–PDA sheets together with covalent bonds. The shrinking mechanism of GO–PDA during dehydration is also discovered in the simulations, which might apply to other 2-D materials.

Chapter 7

Discussion, conclusions, and future research

7.1 Summary of key findings and their significances

In this thesis, a detailed hierarchical structure of eumelanin and PDA is provided by making an assumption that eumelanin and PDA protomolecules are near planar oligomers (oligomer-based approach), The primary, secondary, tertiary (aggregate) structures are clearly defined and shown in the simulations. For the first time, the gap between primary, secondary, and aggregate structures has been bridged to describe the formation of eumelanin-like materials containing a reasonable number (hundreds) of protomolecules. The hierarchical structure contains secondary structures (geometric order) made of stacked protomolecules and higher order aggregate structures (geometric order) made of the secondary structures with different sizes and orientations. Here, a new explanation of the optical properties of eumelanin-like materials has been proposed. The interplay of geometric order and disorder characteristics of the hierarchical structure results in significant and random excitonic couplings among the molecules. Consequently, these couplings broaden the spectrum and give rise to a relative enhancement of absorption intensity at the higher-energy end, which is proportional to the cube of the absorption energy. The concept uncovered here has implications beyond the specific microscopic models of eumelanin and PDA, and provides a significant advancement in the understanding of the optical properties of other materials with similar chemical and structural characteristics.

Unlike the oligomer-based approach (assuming the molecular structures of protomolecules), which is hard to capture the heterogeneous nature of eumelanin and PDA, a monomer-based approach (assuming the fundamental building blocks and reaction schemes) is studied in this thesis. A computational model of the heterogeneous DHI system by mimicking the polymerization mechanism of DHI via controlled *in silico* covalent cross-linking between DHI monomers is presented. The simulation results of the cross-linked DHI systems show the possibility of tuning the molecular structure and mechanical property of eumelanin-like materials by controlling the extent of polymerization *in silico* and provides a more in-depth understanding of the structure–property relationships for exploring practical applications of PDA as a universal coating material by controlling polymer size, polydispersity, and aggregation for the engineering of tailored bio-inspired functional materials.

The oligomer-based and monomer-based approaches are both studied here. The oligomer-based approach can easily reproduce the aggregate structure of eumelanin and PDA observed in experiments by using near planar molecular structure for the simulations. However, since there is no complete set (e.g., dimers, trimers, and tetramers) of eumelanin molecular models proposed in the literature, the oligomer-based approach applied here can not capture the heterogeneous nature of eumelanin-like materials. On the other hand, the monomer-based approach can easily generate different kinds of protomolecules via controlled *in silico* covalent cross-linking between DHI monomers. However, the drawback of this approach is that it does not guarantee the protomolecules generated in the simulations will be near planar structures. As a result, layered structures (secondary structures) made of stacked protomolecules are difficult to reproduce in the simulations using the monomer-based approach.

One of the ultimate goals of this thesis is to propose better molecular models for eumelanin and PDA, which can capture both the heterogeneous nature of these materials as well as the structural planarity of protomolecules.To achieve this goal, a set of computational modeling methods has been proposed to generate and evaluate probable molecular structures of eumelanin and PDA. From a total number of nearly 3,000 probable molecular structures, the most stable dimers, trimers, and tetramers of DHI have been identified using the brute-force algorithm. The results show that more planar molecular structures have a tendency to be more stable; thus, they are more likely to exist. Combining these molecular models, the heterogeneous nature of eumelanin-like materials as well as the structural planarity of protomolecules can both be satisfied at the same time, which will aid more accurate modeling of these materials. The results also provide fundamental explanations of some important structural features of eumelanin-like materials, such as the planar and small size of protomolecules.

One of the most extensively studied applications of PDA is in the form of a component in GO-based nanocomposites. In this thesis, explanations of the enhanced mechanical properties and shrinking ability of GO–PDA paper have been proposed. The results show that the enhanced strength of GO–PDA might merely come from the additional non-covalent interactions provided by PDA, and not from covalent cross-linking that was suggested from other studies. This finding implies an opportunity to increase the mechanical properties of GO–PDA paper further if a large amount of covalent cross-linking can form to connect GO–PDA sheets together with covalent bonds. The shrinking mechanism of GO–PDA during dehydration discovered here might apply to other 2-D materials.

7.2 Opportunities for future research

This thesis provides an essential framework to study the macroscopic properties of eumelanin and PDA using multi-scale modeling methods. Possible opportunities for future research are discussed in this section.

One direction is to extend the investigation on the molecular structure of DHI oligomers to consider larger molecules (e.g., pentamers, hexamers). This future work will need to consider many more molecular structures compared to those used in this thesis. As a result, the conventional DFT calculations performed in this thesis

(Chapter 5) is not suitable to calculate the energy of such significant amount of molecules. Using semi-empirical methods such as PM6 and PM7 might be a possible solution to reduce the computational cost. This future work will provide more details on the molecular structures of eumelanin and PDA as well as provide better molecular models for these materials.

Another direction is to consider environmental effects (e.g., pH value and temperature) on the polymerization mechanism of eumelanin and PDA. By understanding environmental effects on the polymerization mechanism, tuning the properties of eumelanin-like materials can be achieved by controlling the molecular structures of protomolecules. Since conventional DFT calculation is hard to consider environmental effects and non-reactive MD simulation is not able to model the polymerization mechanism, a possible solution is to develop a new version of ReaxFF which is trained to solve this particular problem.

Regarding GO–PDA paper, one possible direction to extend the current study (Chapter 6) is to use a coarse-grained model to simulate much larger systems, which can mimic the actual sizes (up to100 μm) of GO sheets in experiments. Since the GO and GO–PDA models used in the thesis are defect-free due to their small sizes, the simulated mechanical strengths are much higher than those measured in experiments. More reasonable values for the mechanical properties of GO-based nanocomposites can be simulated by using a well-trained coarse-grained model with a proper amount of defects. Besides, computational time can be significantly reduced by using a coarse-grained model, which implies that tuning the mechanical properties (e.g., strength, toughness, and Young's modulus) of GO-based nanocomposites becomes feasible.

Appendix A

Supplementary methods

A.1 Criteria to define secondary structures

Both experimental and computational studies suggested that eumelanin protomolecules could form stacked aggregates via π-π stacking and van der Waals interaction. The stacked aggregates are referred to as eumelanin secondary structures. To define whether two adjacent eumelanin protomolecules stack together and belong to the same secondary structure in the simulations, two criteria are adopted in this thesis (Criteria 1 and 2). The geometry showing the criteria is depicted in Fig. A-1, where two eumelanin protomolecules are represented in a direction perpendicular to the average plane of the molecular structure. Although the tetrameric model is used to illustrate the concepts of the criteria, the same criteria are also applied to other eumelanin molecular models considered in this thesis.

The interlayer spacing between two stacked eumelanin protomolecules was found to be around 3–4 Å in both experimental and computational studies. However, the distance between the centers of two stacked eumelanin protomolecules in the simulations is usually larger than this distance range due to interlayer shifting. In general, the shifting distance depends on the size of the molecular structure. For larger molecular structures, the shifting distance is usually larger; thus the distance between the centers of two stacked eumelanin protomolecules is also larger. For the oligomeric models, Criteria 1 defines that if two eumelanin protomolecules are considered belong to the same secondary structure, the distance between the centers should be smaller than 8 Å. For the monomeric model, since the molecular size is much smaller than that of the oligomeric models, Criteria 1 defines that the distance between centers should be smaller than 6 Å for two monomers to be considered belong to the same secondary structure.

In addition to the distance requirement (Criteria 1) as mentioned above, an orientation requirement is also adopted. If the distance between two adjacent eumelanin protomolecules satisfies the distance requirement (Criteria 1), then their orientation vectors are calculated. The orientation vector of a eumelanin protomolecule is defined in Fig. A-2. If the absolute value of the dot product of the two orientation vectors is larger than 0.8 (Criteria 2) for the oligomeric models, which means that these two eumelanin protomolecules are almost in parallel to each other, they are considered stack together and belong to the same secondary structure. For the monomeric model, the absolute value of the dot product should be larger than 0.9 (Criteria 2). These two criteria that are used to define the secondary structures are empirical. The parameters in the distance and orientation requirements are tuned to produce correct statistical results in small-scale systems, in which the secondary structures can be identified manually. The definition of the reference atoms for the tetrameric model is shown in Fig. A-2. For the pentameric, octameric, and monomeric models, the definition is shown in Fig. A-3. Method to define orientation vectors are shown below:

1. Locate the coordinates of the four reference atoms.
2. Define central position as the averaged coordinate of the reference atoms.
3. Generate reference vectors, $V_{1,3}$ and $V_{2,4}$.
4. Define the orientation vector, $V_n = V_{1,3} \times V_{2,4}$.
5. Normalize V_n to a unit vector.

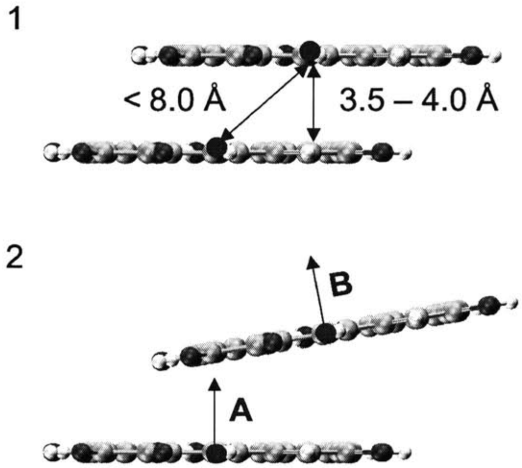

Figure A-1: Criteria to define secondary structures. This figure is adopted from Ref. [9]. Reprinted with permission from Nature Publishing Group.

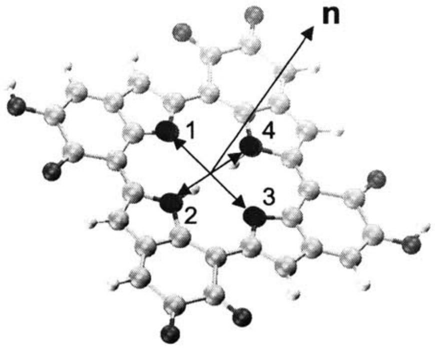

Figure A-2: Definition of orientation vector of eumelanin protomolecule. This figure is adopted from Ref. [9]. Reprinted with permission from Nature Publishing Group.

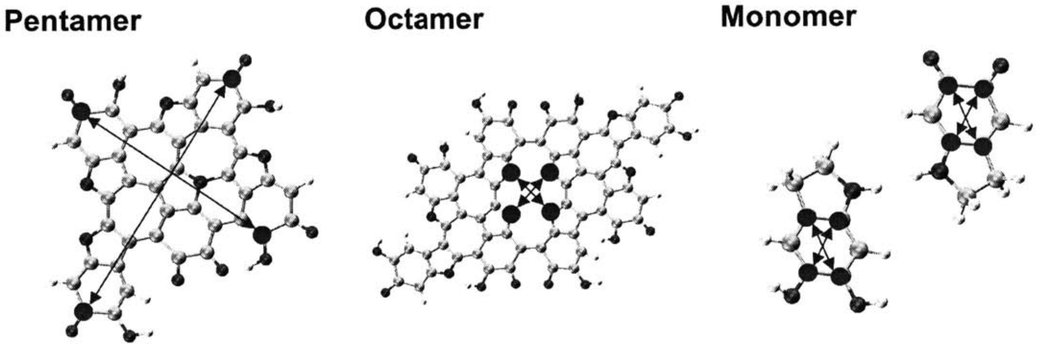

Figure A-3: Definitions of reference atoms for pentameric, octameric, and monomeric models. This figure is adopted from Ref. [9]. Reprinted with permission from Nature Publishing Group.

A.2 Projection product calculation

The definition of the orientation vectors discussed in the previous section is used to calculate the projection product of a DHI oligomer in Chapter 5. The projection product of a DHI oligomer made of m DHI units is defined as : $\sum_{i=1}^{m-1} |V_{n,i} \cdot V_{n,i+1}| \,/\, (m-1)$, where $V_{n,i}$ and $V_{n,i+1}$ are the orientation vectors of i-th and $(i+1)$-th DHI units in the DHI oligomer. The orientation vector of a DHI unit is defined in Fig. A-4.

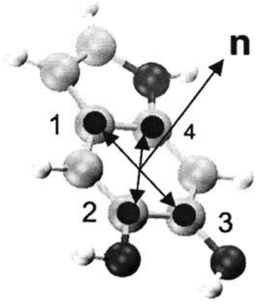

Figure A-4: Definition of orientation vector of DHI unit.

A.3 MD equilibration scheme

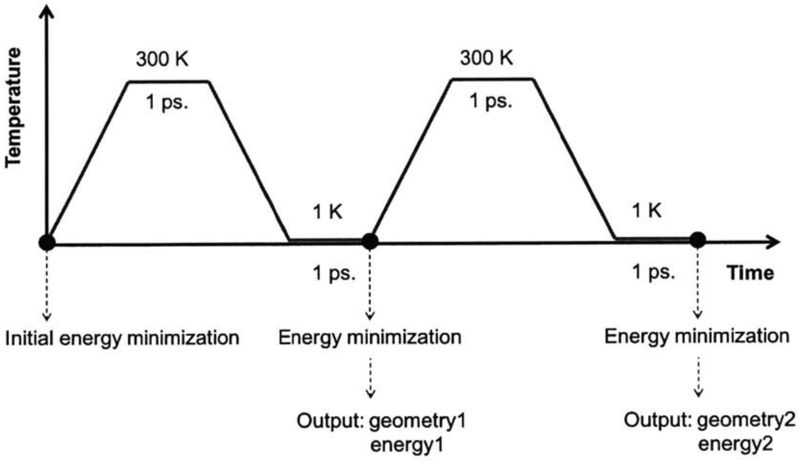

Figure A-5: MD equilibration scheme to find most stable geomatry. The MD equilibration includes 10 iterations. Each iteration generates a geometry and the corresponding energy.

Appendix B

Supplementary results and discussion

B.1 Comparison between DFT and MD

To verify that CVFF [58, 59] is a suitable force field for modeling eumelanin protomolecules, simulations results calculated using MD simulations with CVFF are compared to that calculated using DFT calculations. M1 monomer in the monomeric model (Fig. B-1) is used for the comparison since it has fewer atoms than the other eumelanin molecular models. The molecular structure of M1 monomer is optimized using DFT calculations implemented in an ab initio quantum chemistry program package, ORCA [71], with the B3LYP [72, 73] and the Ahlrichs-VDZ polarized basis set [74]. The same molecular structure is also equilibrated using MD simulations with CVFF. The comparisons of the bond lengths and angles obtained from both methods are shown in Table B.1 and B.2, respectively. The results show that the average difference between using the DFT calculations and MD simulations with CVFF is less than 0.8% for the bond lengths and 1.3% for the angles. Since the other eumelanin molecular models consist of molecular structures similar to M1 monomer, the difference between using both methods on these molecular models should also be small. The results suggest that CVFF is accurate enough in modeling eumelanin protomolecules.

	Bond	DFT (Å)	MD (Å)	Diff. (%)
1	C3–C9	1.5172	1.5084	–0.581
2	C3–C2	1.5636	1.5581	–0.35
3	C3–H15	1.1055	1.1052	–0.0296
4	C3–H16	1.1055	1.1052	–0.029
5	C2–N1	1.4569	1.4789	1.5081
6	C2–H13	1.1082	1.1079	–0.0265
7	C2–H14	1.108	1.1079	–0.0122
8	N1–C8	1.3811	1.4015	1.4711
9	N1–H12	1.0092	1.0266	1.7229
10	C8–C9	1.4043	1.4106	0.445
11	C8–C7	1.4008	1.4122	0.8141
12	C7–C6	1.4039	1.3966	–0.5185
13	C7–H20	1.0962	1.0789	–1.5745
14	C6–C5	1.4111	1.4063	–0.3366
15	C6–O11	1.3622	1.3722	0.7345
16	O11–H19	0.9711	0.9579	–1.3583
17	C5–O10	1.37	1.3724	0.1735
18	C5–C4	1.4019	1.3962	–0.4119
19	O10–H18	0.9707	0.9578	–1.3256
20	C9–C4	1.393	1.4139	1.4992
21	C4–H17	1.0975	1.0793	–1.6578

Table B.1: Comparison of bond lengths calculated using DFT and MD simulations. This table is adopted from Ref. [9]. Reprinted with permission from Nature Publishing Group.

	Angle	DFT (deg.)	MD (deg.)	Diff. (%)
1	C2–C3–C9	103.7938	103.2263	-0.5467
2	C9–C3–H15	112.1342	111.1485	-0.8791
3	C9–C3–H16	112.1272	111.1473	-0.8739
4	C2–C3–H15	111.2015	111.6368	0.3914
5	C2–C3–H16	111.2069	111.6364	0.3863
6	H15–C3–H16	106.4906	108.0535	1.4677
7	C3–C2–N1	104.3361	107.1878	2.7332
8	C3–C2–H13	111.3766	111.0935	-0.2542
9	C3–C2–H14	111.3823	111.0939	-0.2589
10	N1–C2–H13	111.4686	110.4347	-0.9275
11	N1–C2–H14	111.466	110.4356	-0.9244
12	H13–C2–H14	106.9015	106.6362	-0.2482
13	C2–N1–C8	112.3604	107.9425	-3.9319
14	C2–N1–H12	123.3564	126.6671	2.6838
15	C8–N1–H12	124.2823	125.3904	0.8916
16	N1–C8–C9	110.3711	112.7048	2.1144
17	N1–C8–C7	129.2486	127.1736	-1.6055
18	C9–C8–C7	120.3803	120.1217	-0.2148
19	C8–C7–C6	119.4059	118.9209	-0.4061
20	C8–C7–H20	121.1242	120.0451	-0.891
21	C6–C7–H20	119.4699	121.034	1.3092
22	C7–C6–C5	120.5039	120.8493	0.2866
23	C7–C6–O11	122.3509	118.4128	-3.2187
24	C5–C6–O11	117.1452	120.738	3.067
25	C6–O11–H19	109.0402	108.88	-0.1469
26	C6–C5–O10	117.4429	120.6924	2.7669
27	C6–C5–C4	119.1498	120.8803	1.4524
28	C4–C5–O10	123.4073	118.4273	-4.0354
29	C5–O10–H18	108.7279	108.9821	0.2338
30	C9–C4–C5	120.6856	118.6245	-1.7078
31	C5–C4–H17	118.9031	121.1484	1.8883
32	C9–C4–H17	120.4113	120.2271	-0.1529
33	C3–C9–C8	109.1383	108.9386	-0.1829
34	C3–C9–C4	130.9872	130.458	-0.404
35	C8–C9–C4	119.8745	120.6034	0.608

Table B.2: Comparison of angle degrees calculated using DFT and MD simulations. This table is adopted from Ref. [9]. Reprinted with permission from Nature Publishing Group.

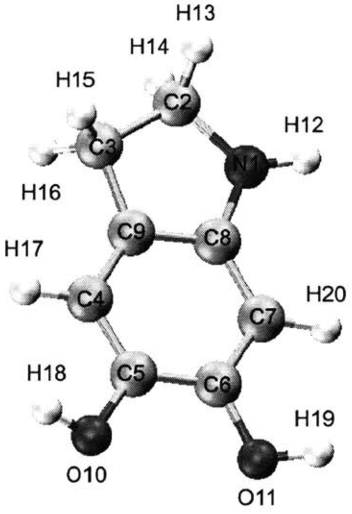

Figure B-1: Molecular structure and atom numbering of M1 monomer. This figure is adopted from Ref. [9]. Reprinted with permission from Nature Publishing Group.

B.2 Orientation of eumelanin protomolecules

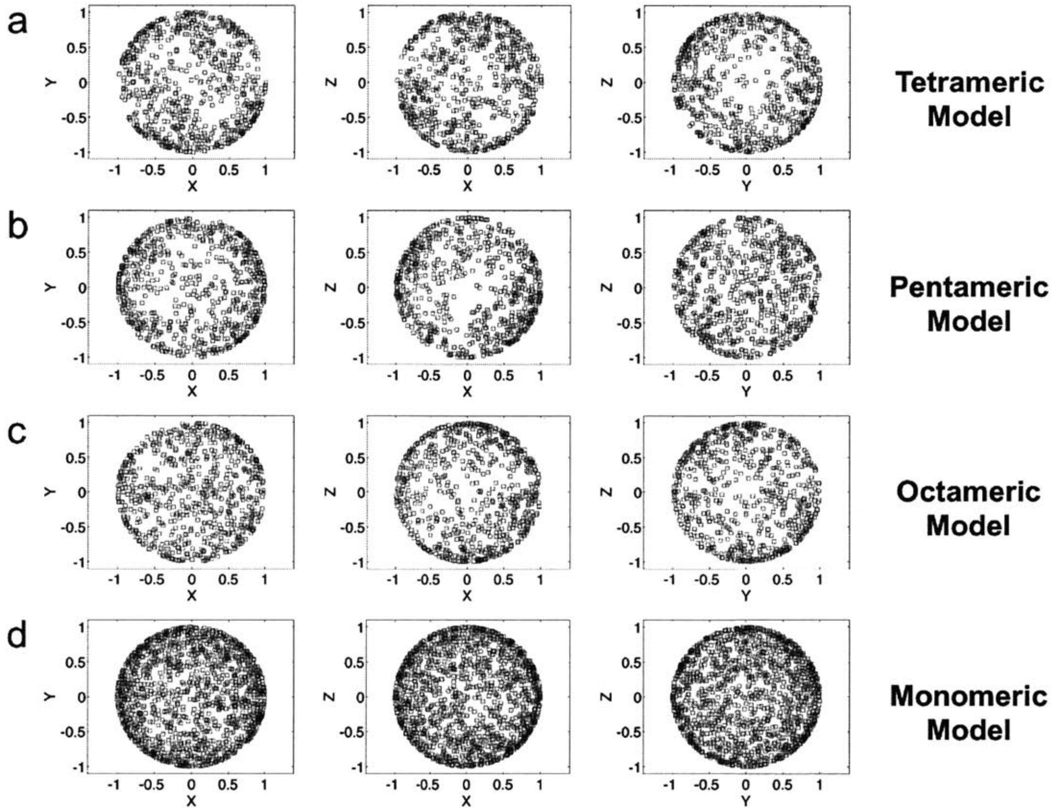

Figure B-2: Orientation of eumelanin protomolecules using tetrameric, pentameric, octameric, and monomeric models. The statistical results show the X, Y, and Z components of the orientation vector of each eumelanin protomolecule in the large-scale system consisting of (a) 729 tetramers, (b) 729 pentamers, (c) 729 octamers, and (d) 1,458 (729-set) monomers, respectively. This figure is adopted from Ref. [9]. Reprinted with permission from Nature Publishing Group.

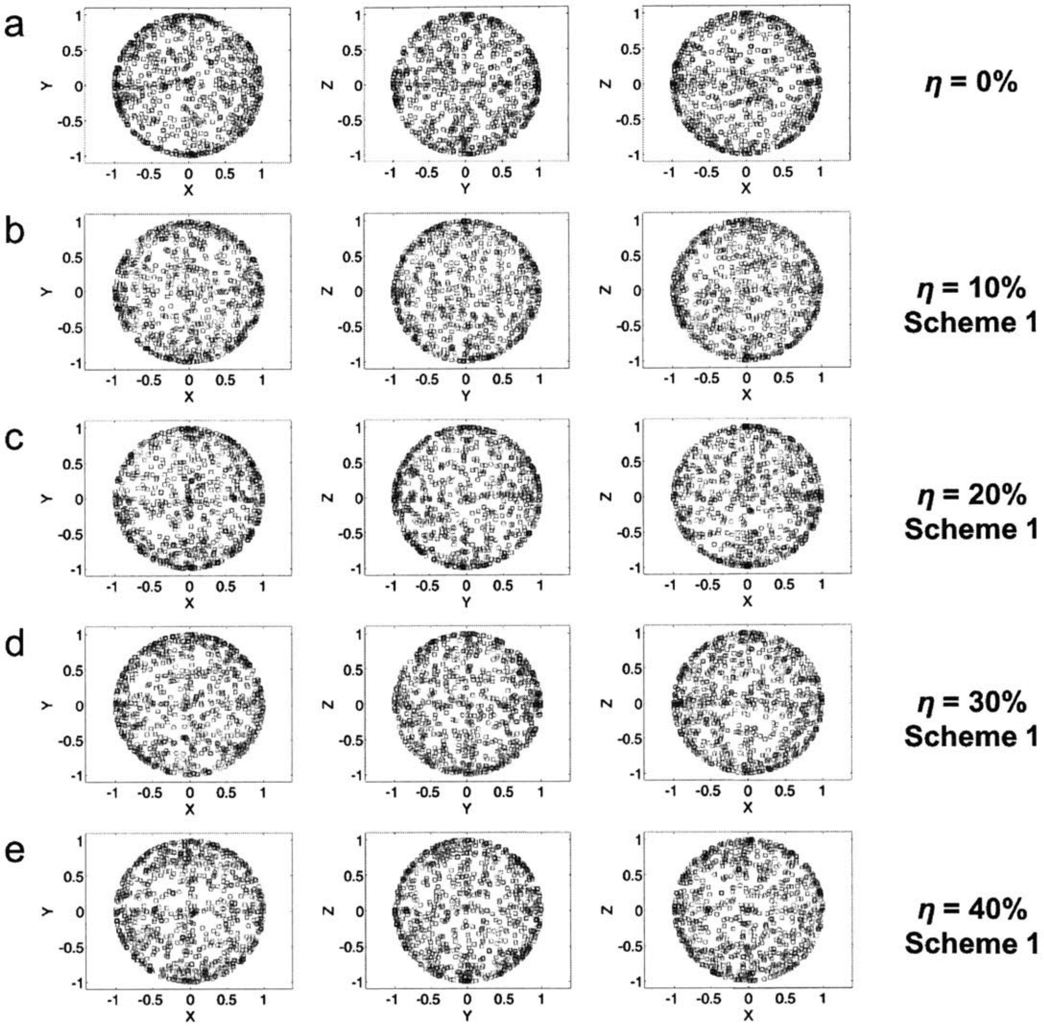
a
Y
X
Z
Y
Z
X
η = 0%
b
η = 10%
Scheme 1
c
η = 20%
Scheme 1
d
η = 30%
Scheme 1
e
η = 40%
Scheme 1
1
0.5
0
-0.5
-1

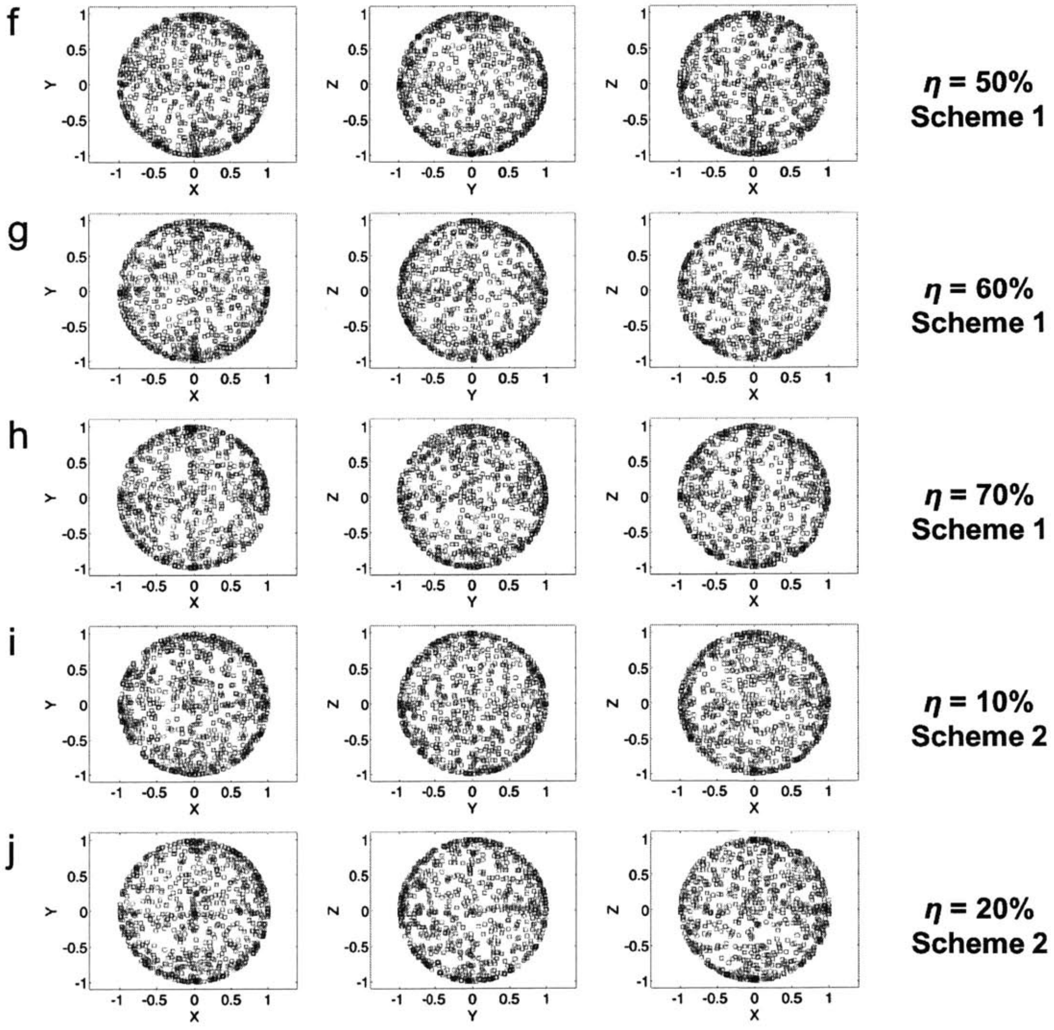
f
η = 50%
Scheme 1
g
η = 60%
Scheme 1
h
η = 70%
Scheme 1
i
η = 10%
Scheme 2
j
η = 20%
Scheme 2
X
Y
Z
-1
-0.5
0
0.5
1

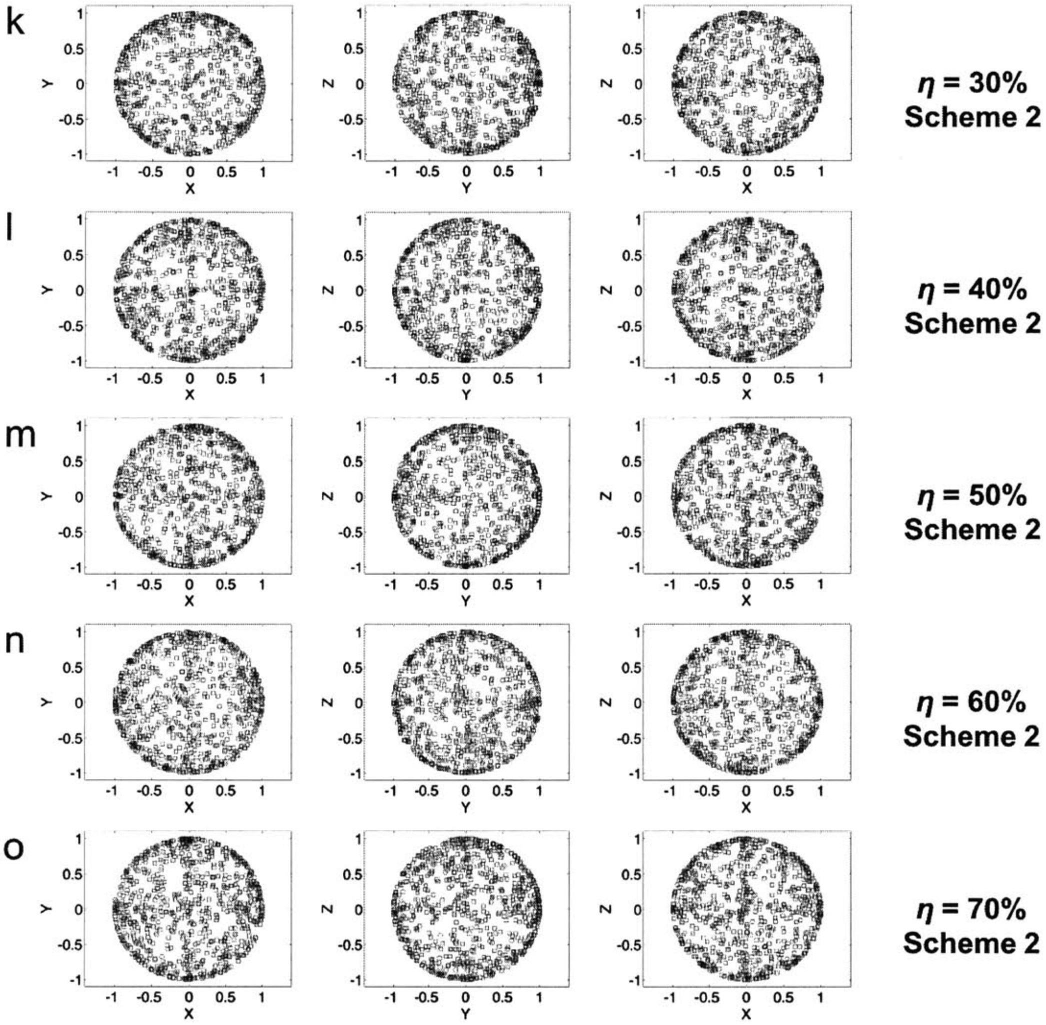

Figure B-3: Orientation of eumelanin protomolecules using cross-linked DHI oligomers. The statistical results show the X, Y, and Z components of the orientation vector of the DHI units for (a) the pure DHI aggregate system ($\eta = 0\%$), and (b)-(q) cross-linked DHI systems at the various η values (10% 70%) considered under cross-linking Schemes 1 and 2. This figure is adopted from Ref. [11]. Reprinted with permission from Royal Society of Chemistry.

B.3 Comparison between ZINDO/S and Frenkel exciton model

A semi-empirical quantum chemistry method, ZINDO/S, and the Frenkel exciton model are implemented to calculate the absorption spectrum of a simple system containing two stacked tetramers (i.e., the tetrameric model proposed by Kaxiras et al. [5]). The interlayer spacing between the two tetramers is adjusted to 4.0 Å, which is a typical interlayer distance between stacked eumelanin protomolecules. The results (Fig. B-4) show that the Frenkel exciton model is accurate enough in calculating the absorption spectra of the eumelanin protomolecules since these two methods both predict similar results.

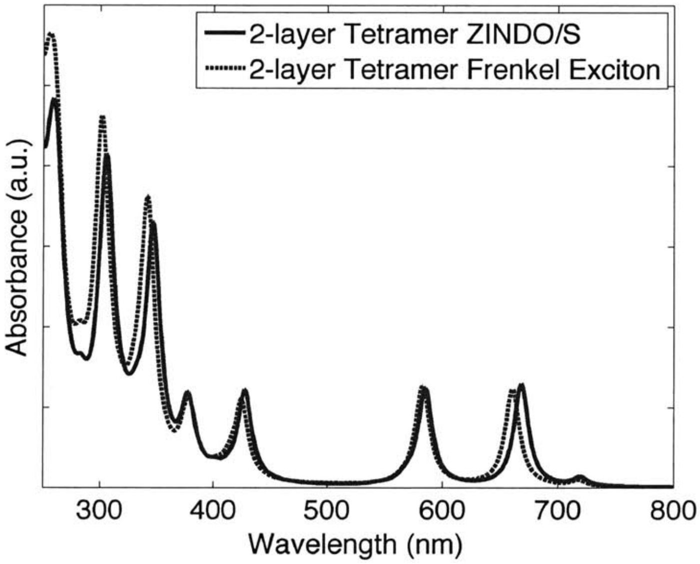

Figure B-4: Comparison between ZINDO/S method and Frenkel exciton model. The results obtained using both methods are very close. This figure is adopted from Ref. [9]. Reprinted with permission from Nature Publishing Group.

B.4 Absorption spectra for other eumelanin molecular models

Additional simulation results for other eumelanin molecular models including a tetrameric model proposed by Panzella et al. [12] and a pentameric model proposed by Arzillo et al. [13] are reported. In addition to the four different eumelanin molecular models discussed in Chapter 3, these two molecular models are also considered since they have been isolated and structurally characterized in the experiments [12, 13]. The molecular models and equilibrium structures of the small-scale systems made of these two models are shown in Fig. B-5. Since the tetrameric model proposed by Kaxiras et al. [5] and the pentameric model proposed by Cheng et al. [6, 7] are already considered in Chapter 3, the tetrameric model proposed by Panzella et al. [12] and the pentameric model proposed by Arzillo et al. [13] are referred to as the tetrameric model (D), and pentameric model (D), respectively.

The absorption spectra of these two models are shown in Fig. B-6. The results support the arguments and conclusions in Chapter 3; the excitonic couplings among the eumelanin protomolecules are strong enough to change the landscape of the absorption spectrum, and the superposition is invalid in this situation. In addition, as more molecules are considered in a system, the simulated spectrum of the system becomes more broaden and smooth, which is consistent with the eumelanin molecular models discussed in Chapter 3. However, these two molecular models are unlikely to be the dominant protomolecules of eumelanin. From the structural perspective, these two molecular models are not planar structures; thus, they do not form quasi-ordered secondary structures, which is in contrary to the recent experimental observations [10, 40]. From the optical perspective, since these two molecular models are not planar structures, the electrons on these molecules are less delocalized than other planar molecular models (e.g., the tetrameric model proposed by Kaxiras et al. [5] as well as the pentameric and octameric models proposed by Cheng et al. [6, 7]). As a result, these two molecular models do not absorb the visible light with longer wavelength (> 500 nm), which is in contrary to the absorption spectrum of eumelanin. Although

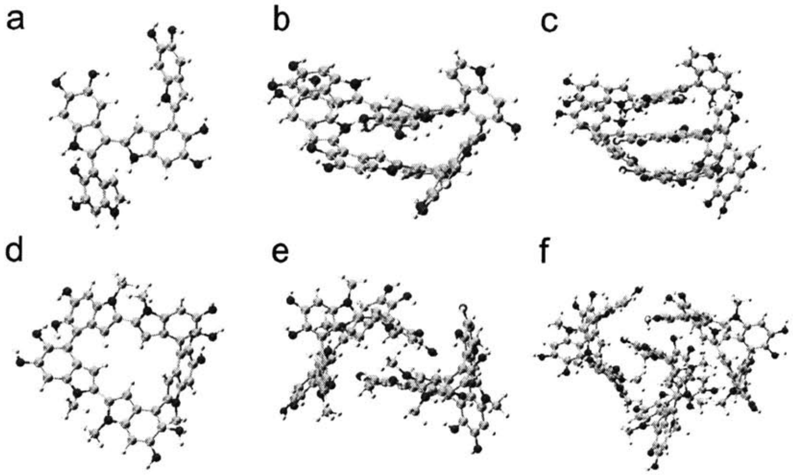

Figure B-5: Molecular models of eumelanin (other molecular models). (a) Tetrameric model proposed by Panzella et al. [12]. (b) Two-layer stacked structure of tetrameric model. (c) Three-layer stacked structure of tetrameric model. (d) Pentameric model proposed by Arzillo et al. [13]. (e) Two-layer stacked structure of pentameric model. (f) Three-layer stacked structure of pentameric model. This figure is adopted from Ref. [9]. Reprinted with permission from Nature Publishing Group.

these particular molecular models were found to exist in the experiments [12, 13], they might not constitute the majority of the chemically disordered mixture.

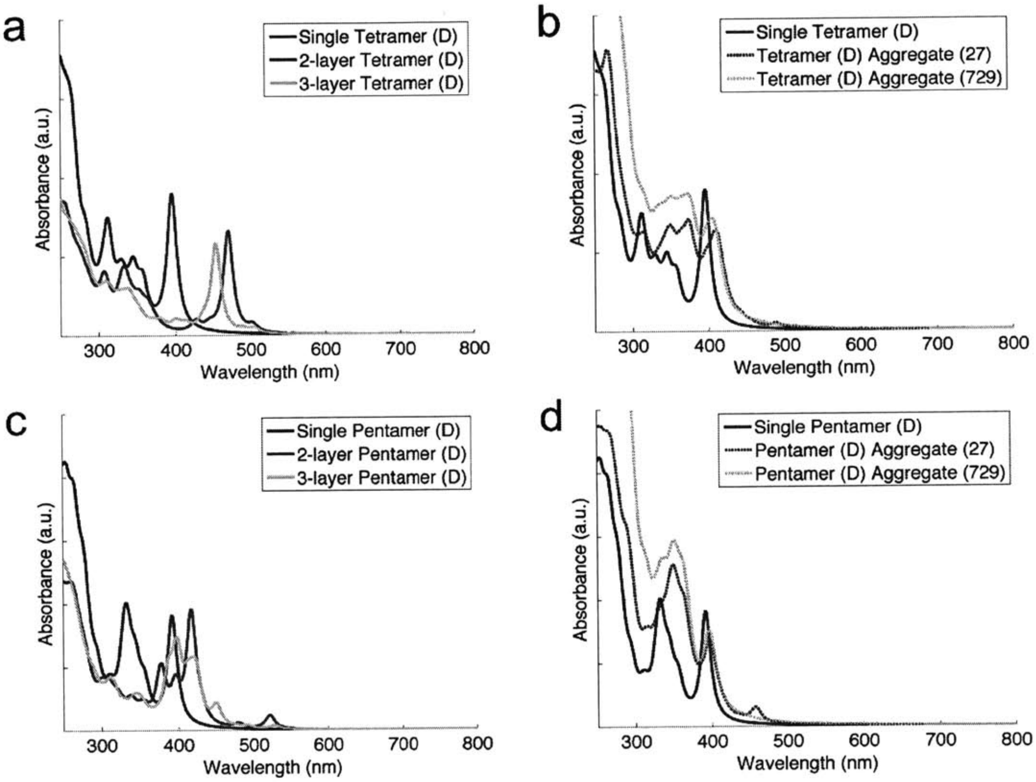

Figure B-6: Absorption spectra for other eumelanin molecular models. (a) and (c) are the respective spectra of the small-scale systems calculated directly with the ZINDO/S method. (b) and (d) are the respective spectra of the large-scale systems. The excitonic interactions are calculated using the Frenkel exciton model with the atomic transition charge distribution method. This figure is adopted from Ref. [9]. Reprinted with permission from Nature Publishing Group.

B.5 Absorption spectra for different redox forms

Eight different redox forms of the tetrameric model proposed by Kaxiras et al. [5] are considered. There are 21 possible redox forms in a tetramer, but only eight of them have large negative formation energy and are considered as the dominant tetramers. The molecular structures of these tetramers are shown in Fig. B-7. The molecular name of these tetramers are adopted from the work of Kaxiras et al. [5]. The tetrameric model discussed in Chapters 2, 3, and 4 is tetramer QIQI (Fig. B-7e), which is the most stable tetramer among these eight different redox forms.

The absorption spectra of the small-scale systems made of the tetramers in different redox forms are shown in Fig. B-8. These results show that considering different redox forms does not change the arguments and conclusions in Chapter 3. No matter what redox forms the eumelanin protomolecules are, as long as they are aromatic-conjugated oligomers, the arguments and conclusions are valid: the excitonic couplings among the eumelanin protomolecules are strong enough to change the landscape of the spectrum, and as more molecules are considered in a system, the spectrum of the system becomes more broaden and smooth.

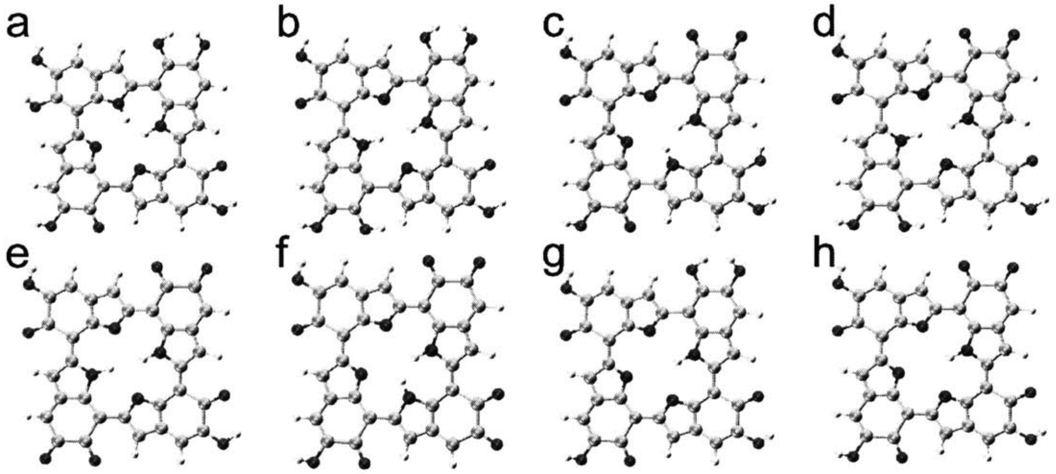

Figure B-7: Molecular structure of tetrameric model in different redox forms. The molecular structures of the eight dominant tetramers are (a) QQHH, (b) QHQH, (c) QQIH, (d) QHQI, (e) QIQI, (f) QQII, (g) QQQH, and (h) QQQI. This figure is adopted from Ref. [9]. Reprinted with permission from Nature Publishing Group.

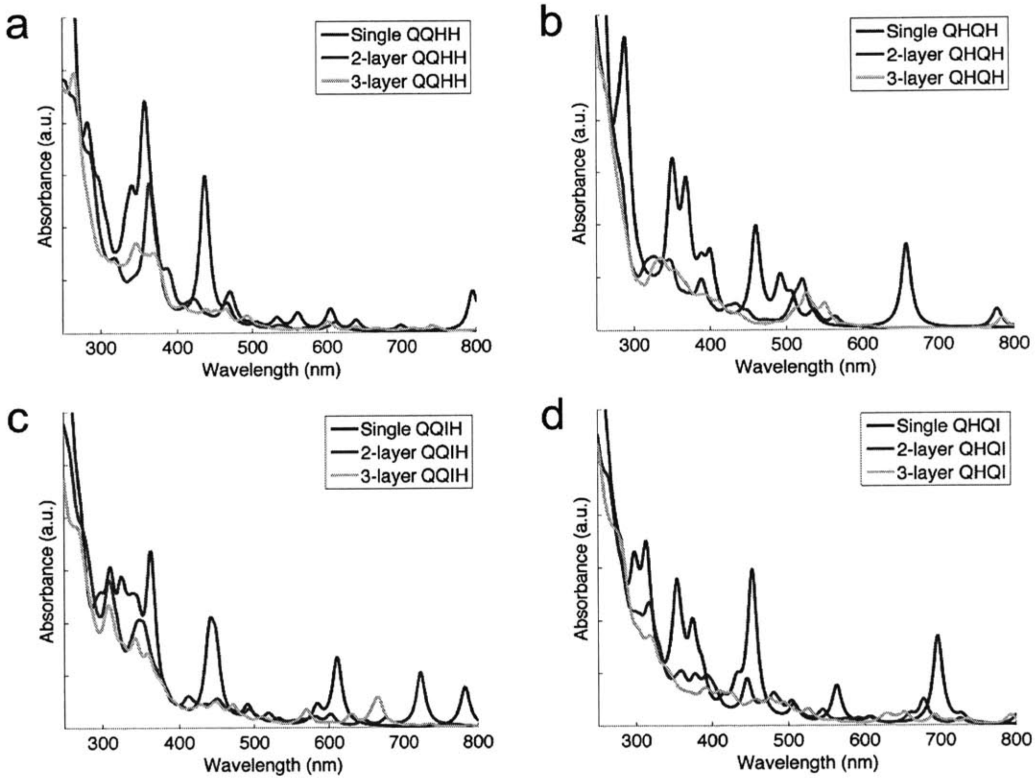
a
Single QQHH
2-layer QQHH
3-layer QQHH
Absorbance (a.u.)
Wavelength (nm)
300
400
500
600
700
800
b
Single QHQH
2-layer QHQH
3-layer QHQH
Absorbance (a.u.)
Wavelength (nm)
300
400
500
600
700
800
c
Single QQIH
2-layer QQIH
3-layer QQIH
Absorbance (a.u.)
Wavelength (nm)
300
400
500
600
700
800
d
Single QHQI
2-layer QHQI
3-layer QHQI
Absorbance (a.u.)
Wavelength (nm)
300
400
500
600
700
800

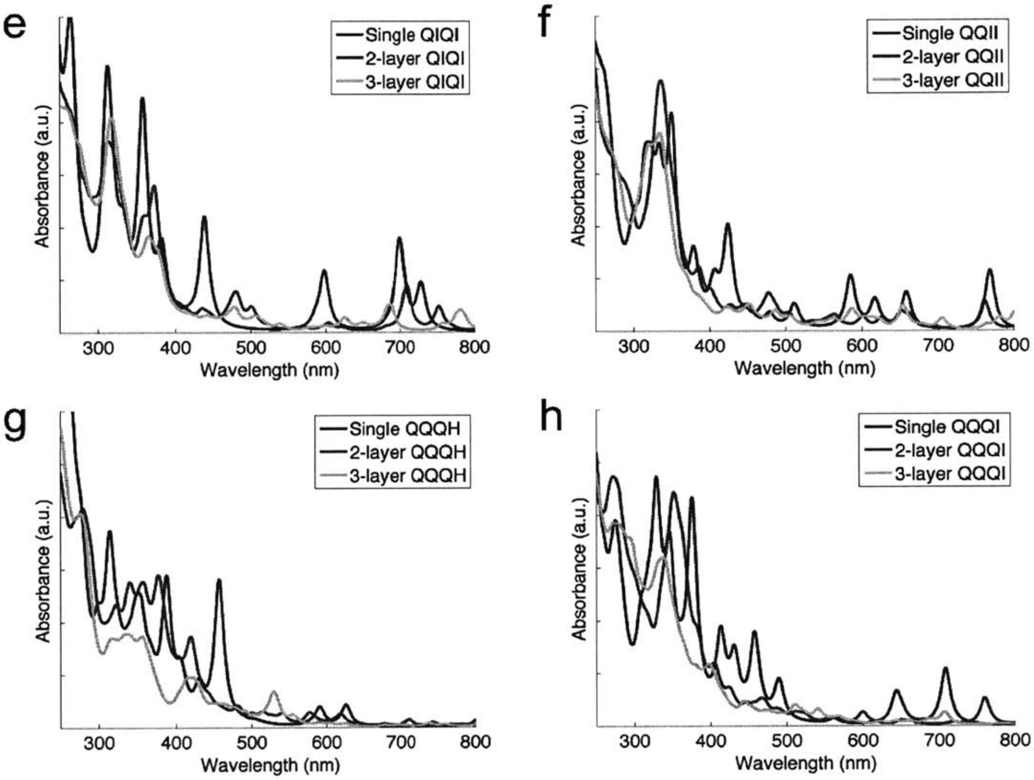

Figure B-8: Absorption spectra of tetrameric model in different redox forms. The respective spectra are calculated directly with the ZINDO/S method. Due to the proximity of the stacked eumelanin protomolecules, it can be seen that the significant excitonic interactions qualitatively change the landscape of the spectra. This figure is adopted from Ref. [9]. Reprinted with permission from Nature Publishing Group.

B.6 Checkerboard representations of dimers

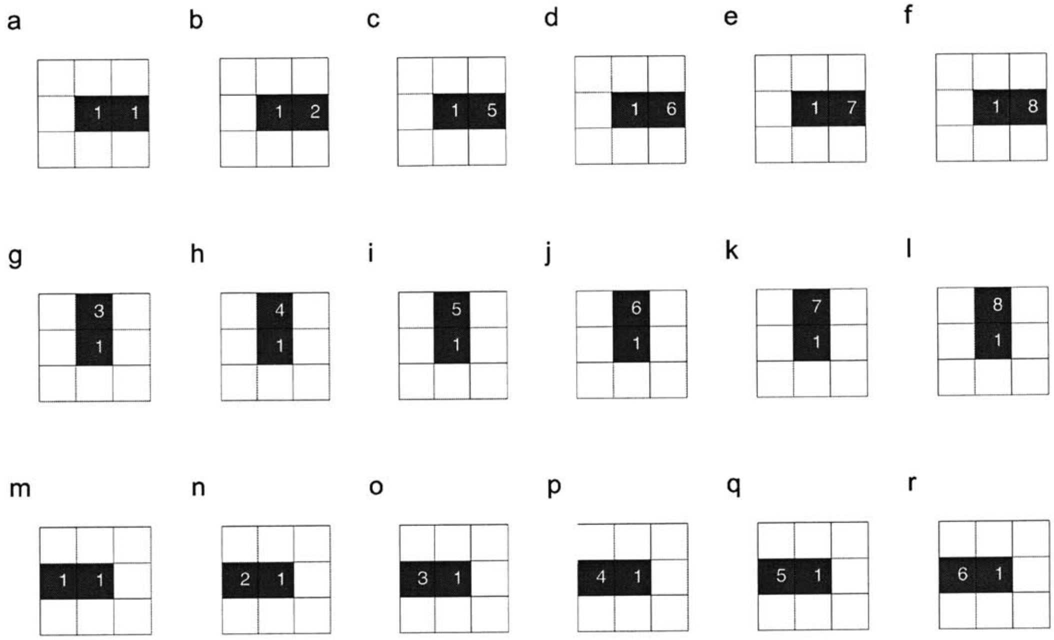

Figure B-9: Checkerboard representations of dimers. (a) to (r) show the checkerboard representations of Dimer-1 to Dimer-18, respectively.

B.7 Molecular structures and energies of dimers and trimers

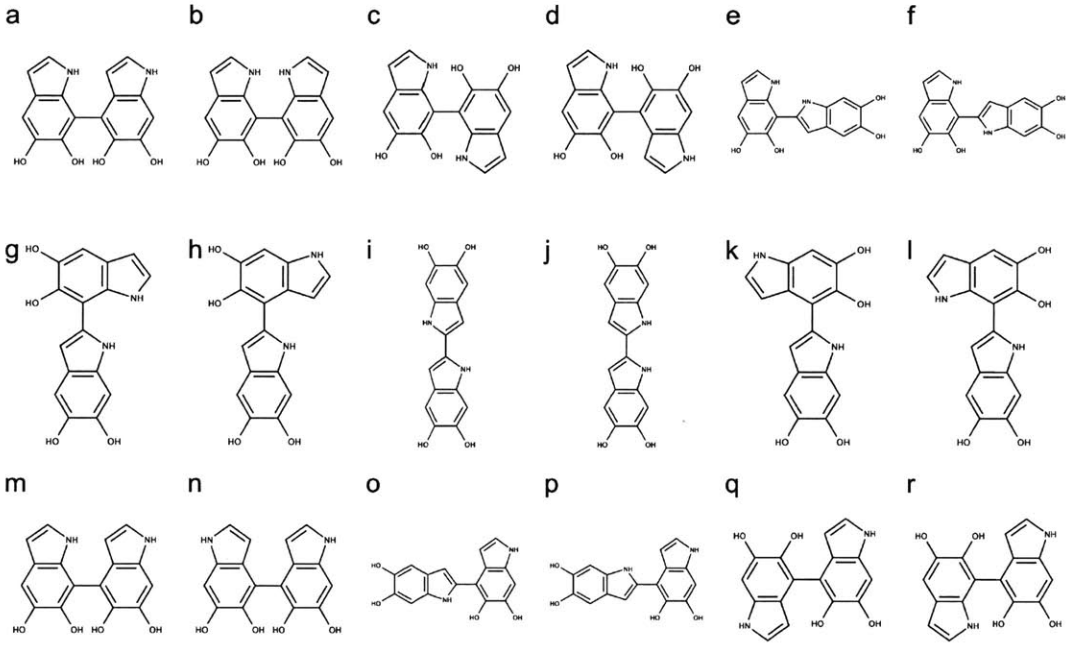

Figure B-10: Molecular structures of dimers. (a) to (r) show the molecular structures of Dimer-1 to Dimer-18, respectively.

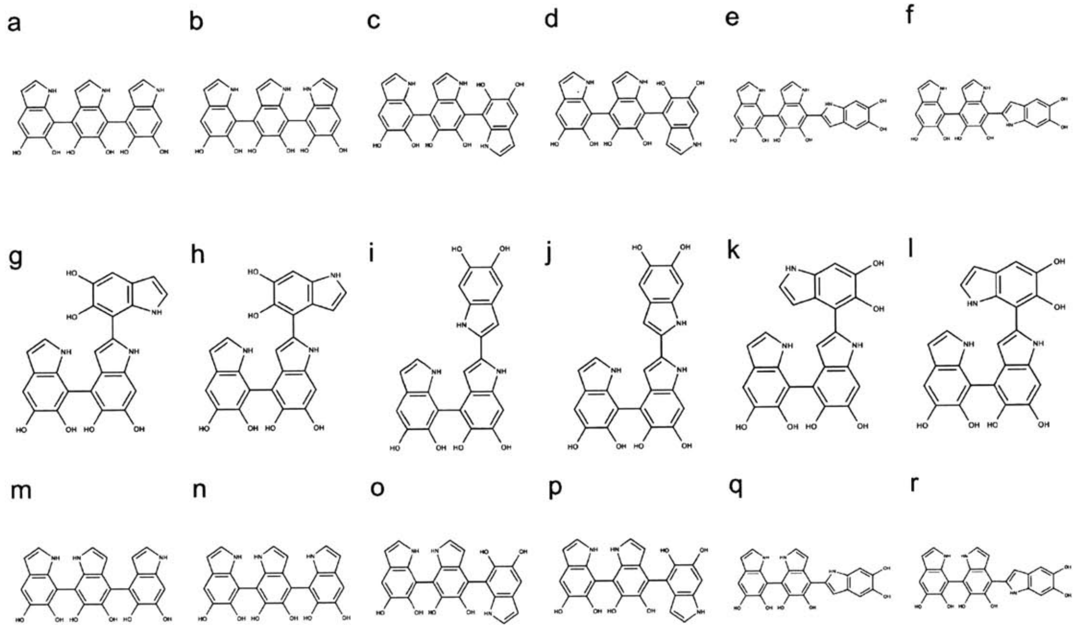

Figure B-11: Molecular structures of trimers. (a) to (r) show the molecular structures of Trimer-1 to Trimer-18, respectively.

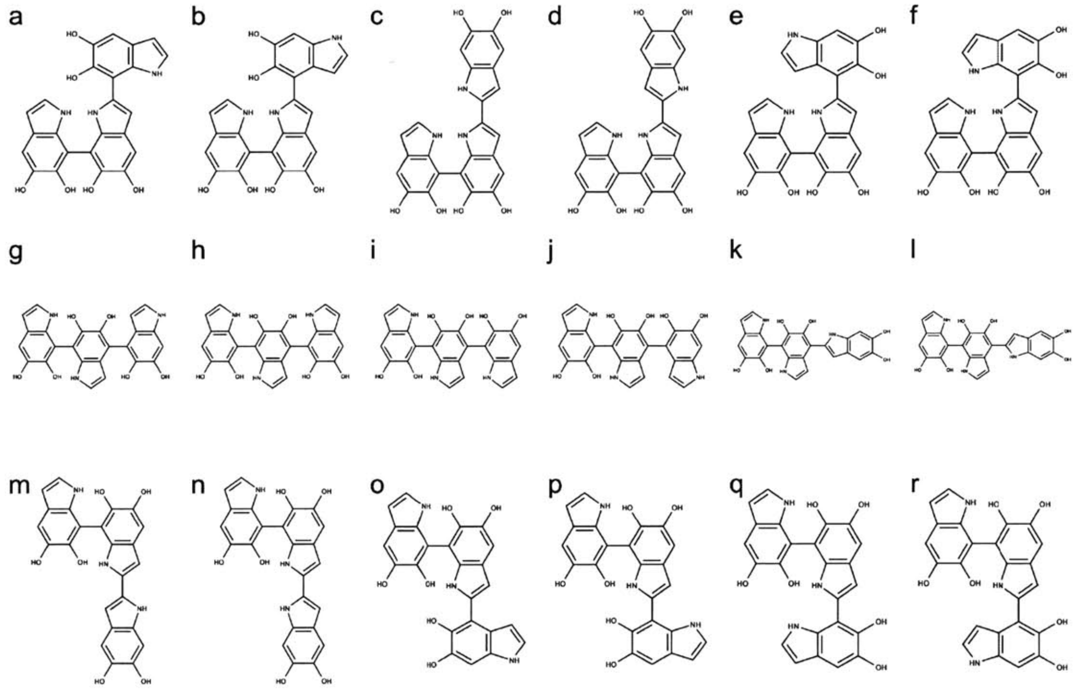

Figure B-12: Molecular structures of trimers. (a) to (r) show the molecular structures of Trimer-19 to Trimer-36, respectively.

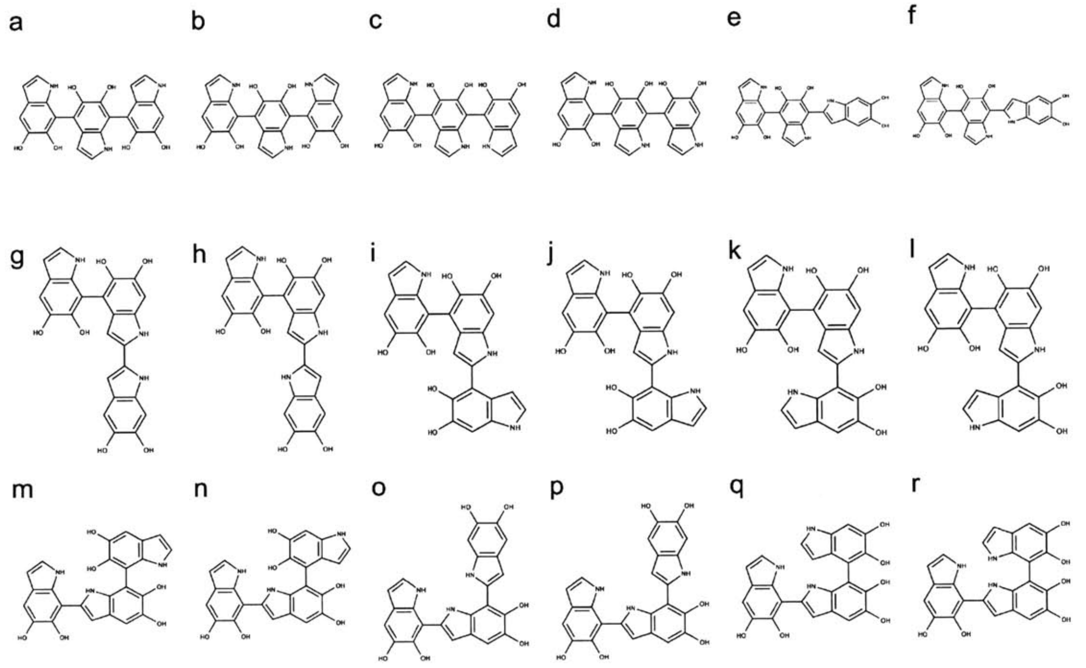

Figure B-13: Molecular structures of trimers. (a) to (r) show the molecular structures of Trimer-37 to Trimer-54, respectively.

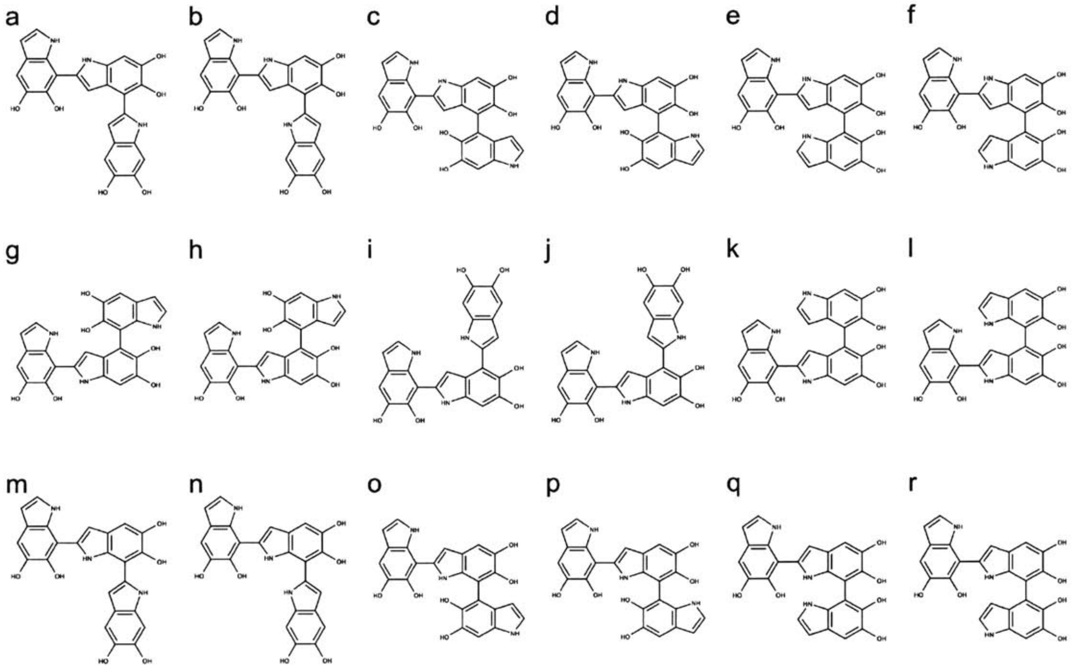

Figure B-14: Molecular structures of trimers. (a) to (r) show the molecular structures of Trimer-55 to Trimer-72, respectively.

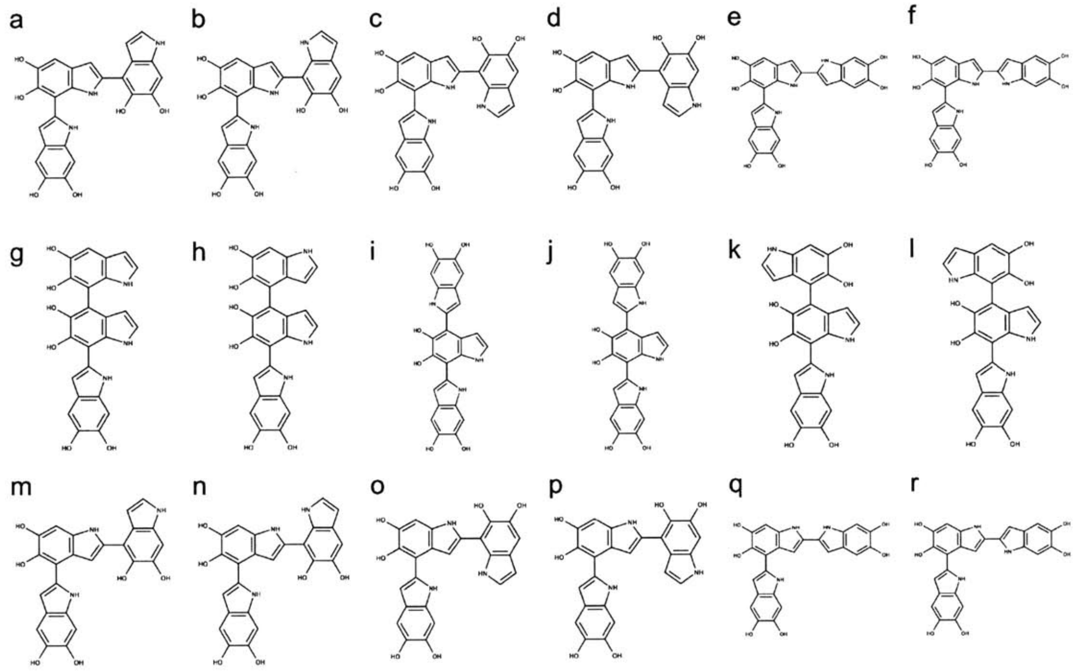

Figure B-15: Molecular structures of trimers. (a) to (r) show the molecular structures of Trimer-73 to Trimer-90, respectively.

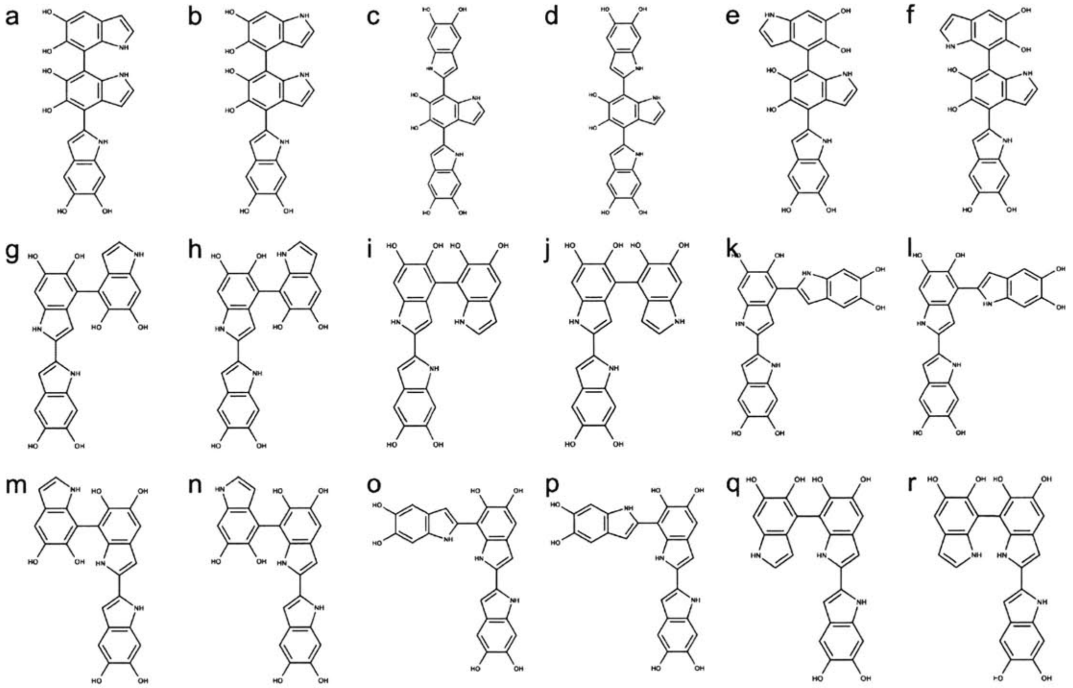

Figure B-16: Molecular structures of trimers. (a) to (r) show the molecular structures of Trimer-91 to Trimer-108, respectively.

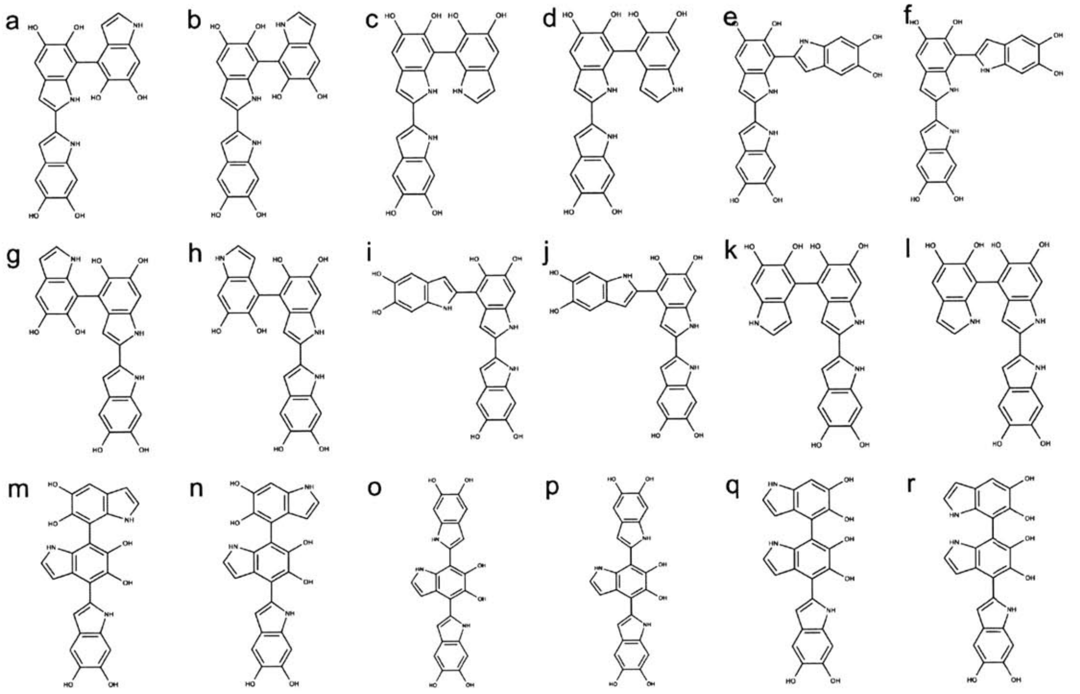

Figure B-17: Molecular structures of trimers. (a) to (r) show the molecular structures of Trimer-109 to Trimer-126, respectively.

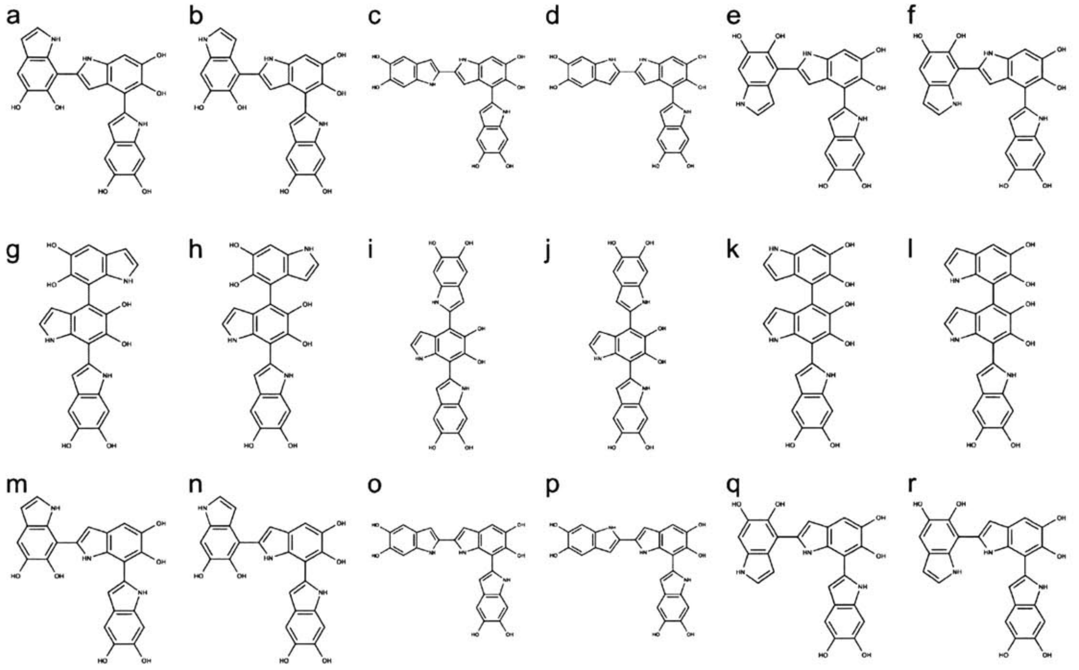

Figure B-18: Molecular structures of trimers. (a) to (r) show the molecular structures of Trimer-127 to Trimer-144, respectively.

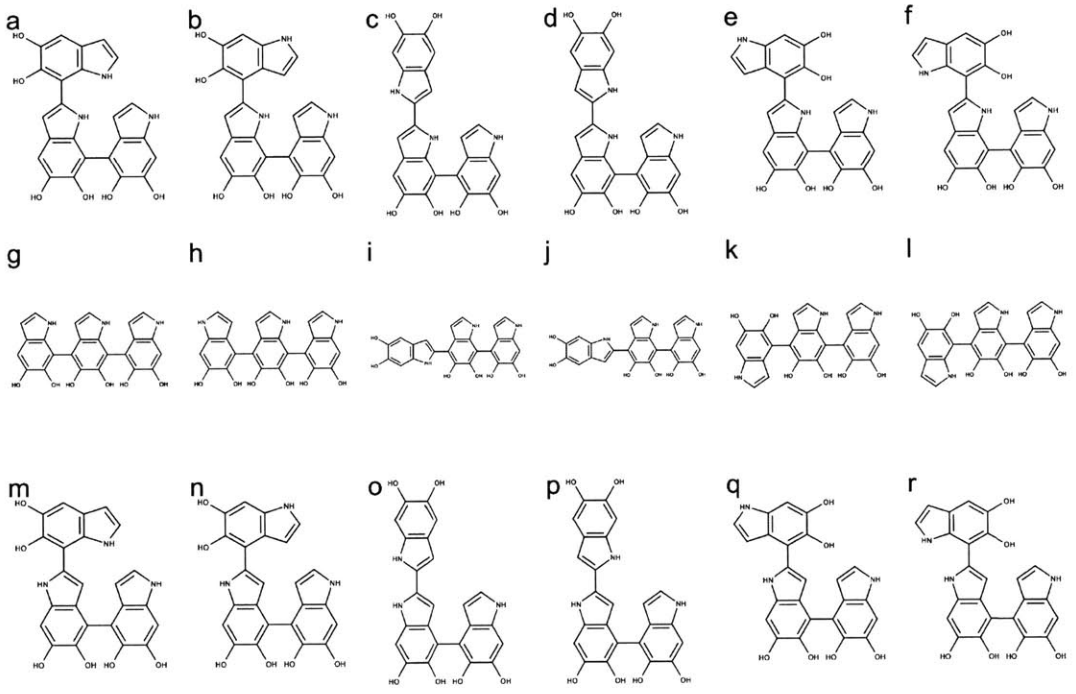

Figure B-19: Molecular structures of trimers. (a) to (r) show the molecular structures of Trimer-145 to Trimer-162, respectively.

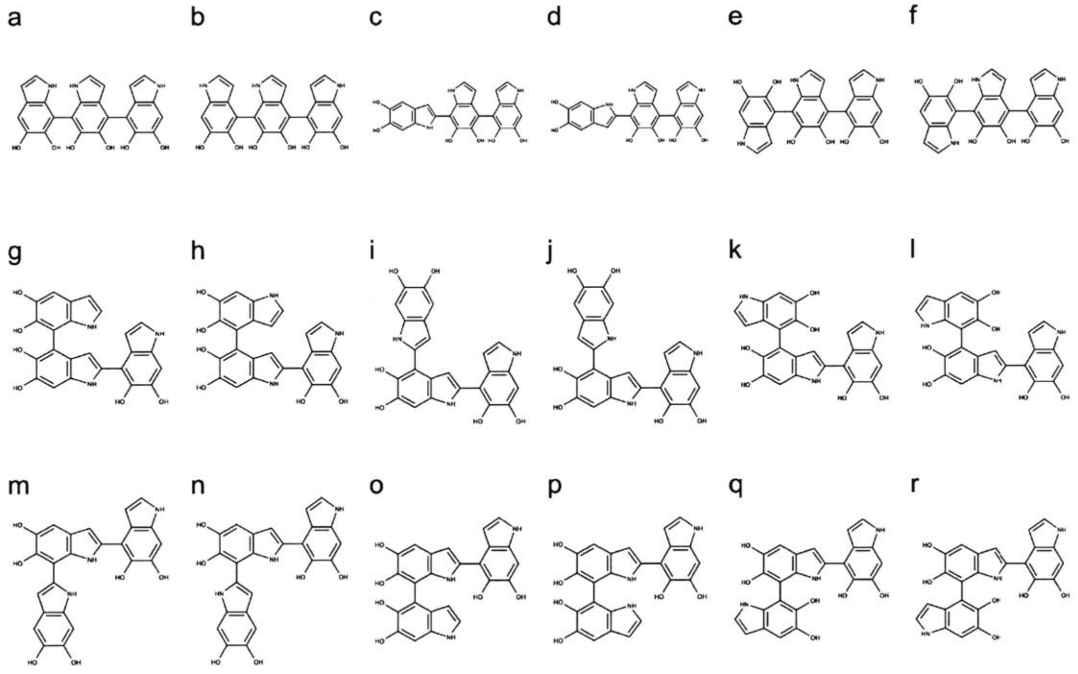

Figure B-20: Molecular structures of trimers. (a) to (r) show the molecular structures of Trimer-163 to Trimer-180, respectively.

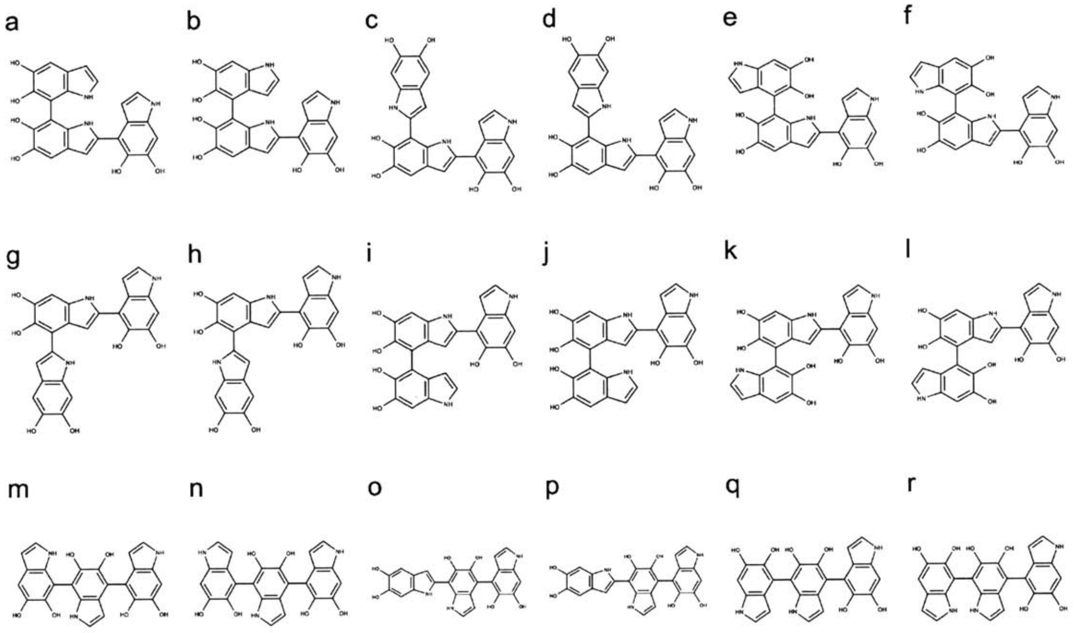

Figure B-21: Molecular structures of trimers. (a) to (r) show the molecular structures of Trimer-181 to Trimer-198, respectively.

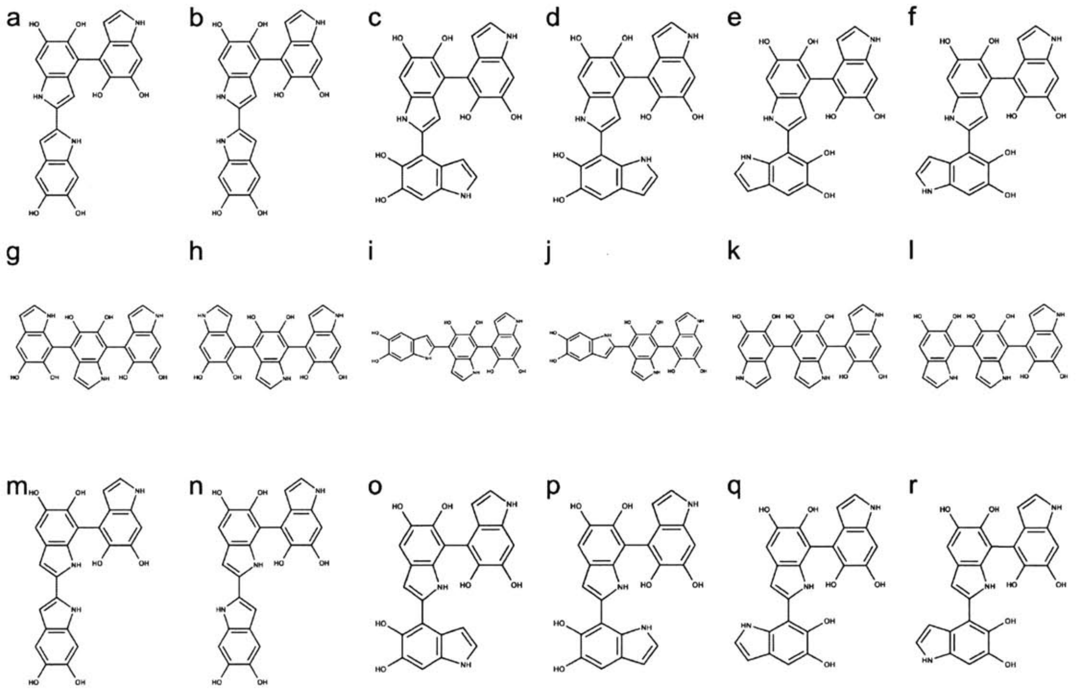

Figure B-22: Molecular structures of trimers. (a) to (r) show the molecular structures of Trimer-199 to Trimer-216, respectively.

ID	Bonding	Energy	ID	Bonding	Energy	ID	Bonding	Energy
1	4–7'	0.66*	7	2–7'	3.61*	13	4–7'	0.63
2	7–7'	5.27*	8	2–4'	0.85*	14	4–4'	4.07*
3	7–7'	0.94	9	2–2'	0.37	15	2–4'	1.61*
4	4–7'	5.56*	10	2–2'	3.00*	16	2–4'	0
5	2–7'	3.62*	11	2–4'	1.61*	17	4–4'	1.14
6	2–7'	0.63*	12	2–7'	0.62	18	4–7'	0.64*

Table B.3: Relative energies and covalent bonding positions of all dimers. The energies in the table are relative energies compared to the most stable dimer (Dimer-16). The energy unit is kcal/mol, and * indicates that the molecule is a higher energy conformation. The more stable dimers are those made through 2,4'-position, 2,2'-position, and 2,7'-position. The less stable dimers are those made through 4,7'-position, 7,7'-position, and 4,4'-position.

ID	Energy	ID	Energy	ID	Energy	ID	Energy	ID	Energy	ID	Energy
1	0.53	37	10.8	73	5.88	109	7.48	145	2.84	181	7.47
2	1.07	38	9.48	74	4.36	110	6.34	146	2.4	182	1.12
3	5.29	39	9.17	75	7.76	111	2.89	147	0.95	183	1.78
4	6.17	40	6.08	76	8.94	112	1.66	148	2.51	184	4.17
5	3.84	41	2.21	77	3.66	113	2.41	149	2.44	185	10.68
6	0.34	42	8.77	78	5.84	114	5.84	150	2.52	186	5.53
7	1.87	43	7.55	79	3.86	115	7.56	151	0.48	187	5.13
8	1.07	44	5.39	80	6.43	116	3.55	152	3.88	188	1.6
9	0.43	45	4.64	81	4.78	117	6.33	153	1.91	189	3.51
10	1.85	46	5.32	82	3.27	118	3.71	154	0.3	190	1.07
11	4	47	1.19	83	4.67	119	5.05	155	1.42	191	4.62
12	0.67	48	6.73	84	8.79	120	3.6	156	6.08	192	5.74
13	3.83	49	5.18	85	9.59	121	5.38	157	3.48	193	6.01
14	8.13	50	7.01	86	4.01	122	7.98	158	5.08	194	6.79
15	12.68	51	7.76	87	0.2	123	4.78	159	5.05	195	5.74
16	8.88	52	5.71	88	1.73	124	1.77	160	3.66	196	2.04
17	7.45	53	2.85	89	2.27	125	2.76	161	9.69	197	1.45
18	2.27	54	3.88	90	0	126	2.28	162	7.9	198	1.89
19	2.43	55	5.18	91	8.56	127	5.2	163	3.81	199	1.93
20	3.2	56	3.21	92	1.16	128	6.58	164	3.87	200	2.55
21	2.24	57	4.66	93	1.01	129	1.54	165	4.16	201	2.54
22	1.41	58	9.25	94	3.27	130	2.79	166	6.99	202	2.44
23	5.64	59	5.57	95	5.64	131	3.34	167	9.19	203	4.67
24	9.71	60	8.36	96	6.06	132	2.2	168	7.08	204	5.75
25	6.01	61	5.26	97	1.93	133	2.83	169	4.01	205	11.21
26	10.74	62	3	98	2.43	134	1.47	170	5.08	206	6.84
27	10.74	63	0.23	99	0.44	135	0.74	171	3.35	207	5.61
28	4.97	64	2.98	100	3.67	136	1.77	172	6.74	208	7.01
29	6.39	65	4.17	101	1.53	137	3.59	173	3.18	209	9.25
30	4.68	66	2.17	102	0.77	138	0.89	174	6.72	210	6.14
31	5.46	67	3.86	103	4.37	139	3.47	175	5.86	211	2.73
32	4.25	68	4.34	104	1.7	140	2.74	176	1.89	212	5.81
33	3.49	69	2.54	105	3.66	141	3.92	177	3.78	213	2.06
34	5.25	70	5.9	106	1.63	142	1.66	178	9.29	214	3.56
35	5.14	71	1.94	107	0.96	143	6.34	179	5.04	215	6.53
36	7.76	72	2.2	108	7.95	144	4.83	180	6.56	216	6.56

Table B.4: Relative energies of all trimers. The energies in the table are relative energies compared to the most stable trimer (Trimer-90). The energy unit is kcal/mol.

B.8 Pulling tests for GO and GO–PDA paper

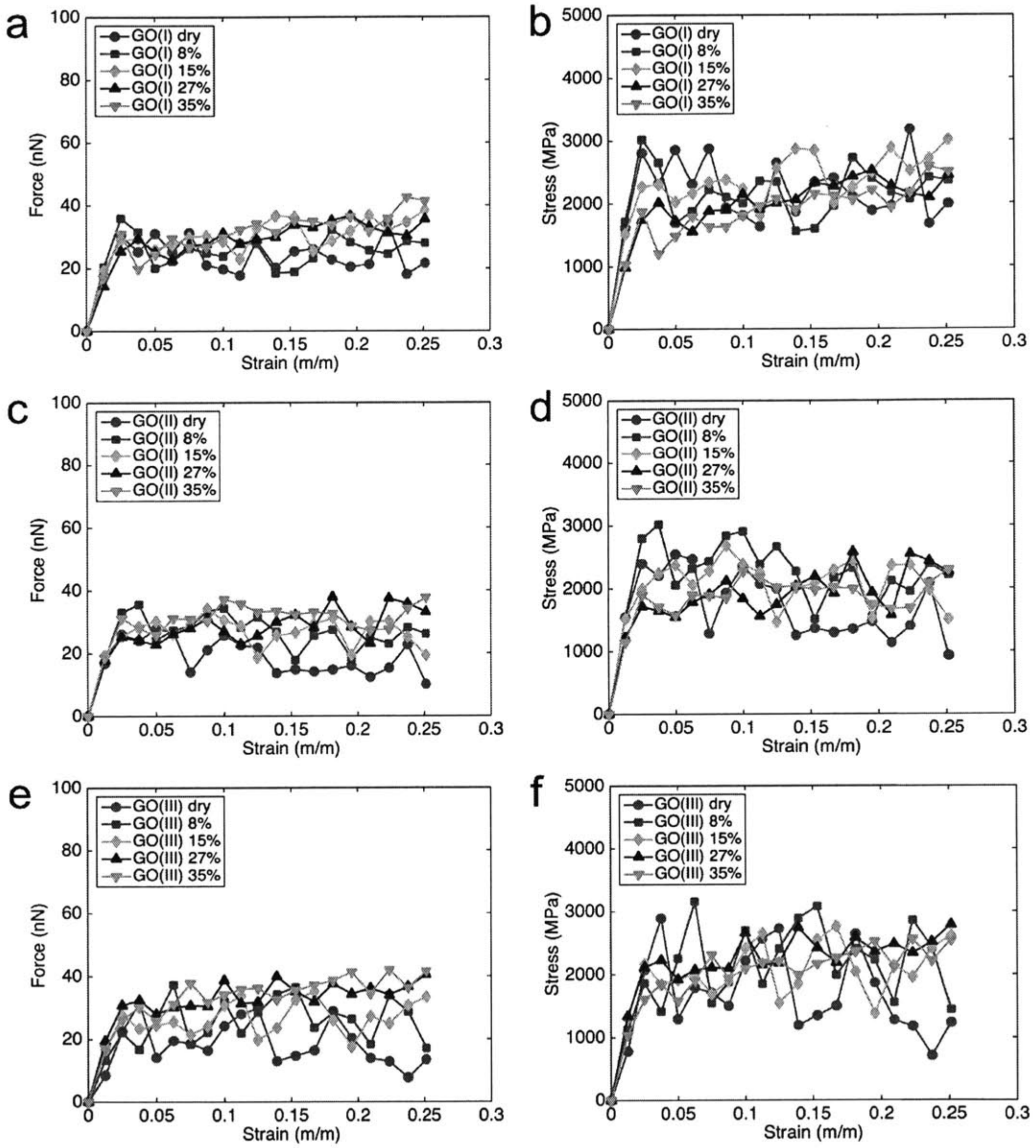

Figure B-23: Force-strain and stress-strain curves for GO models.

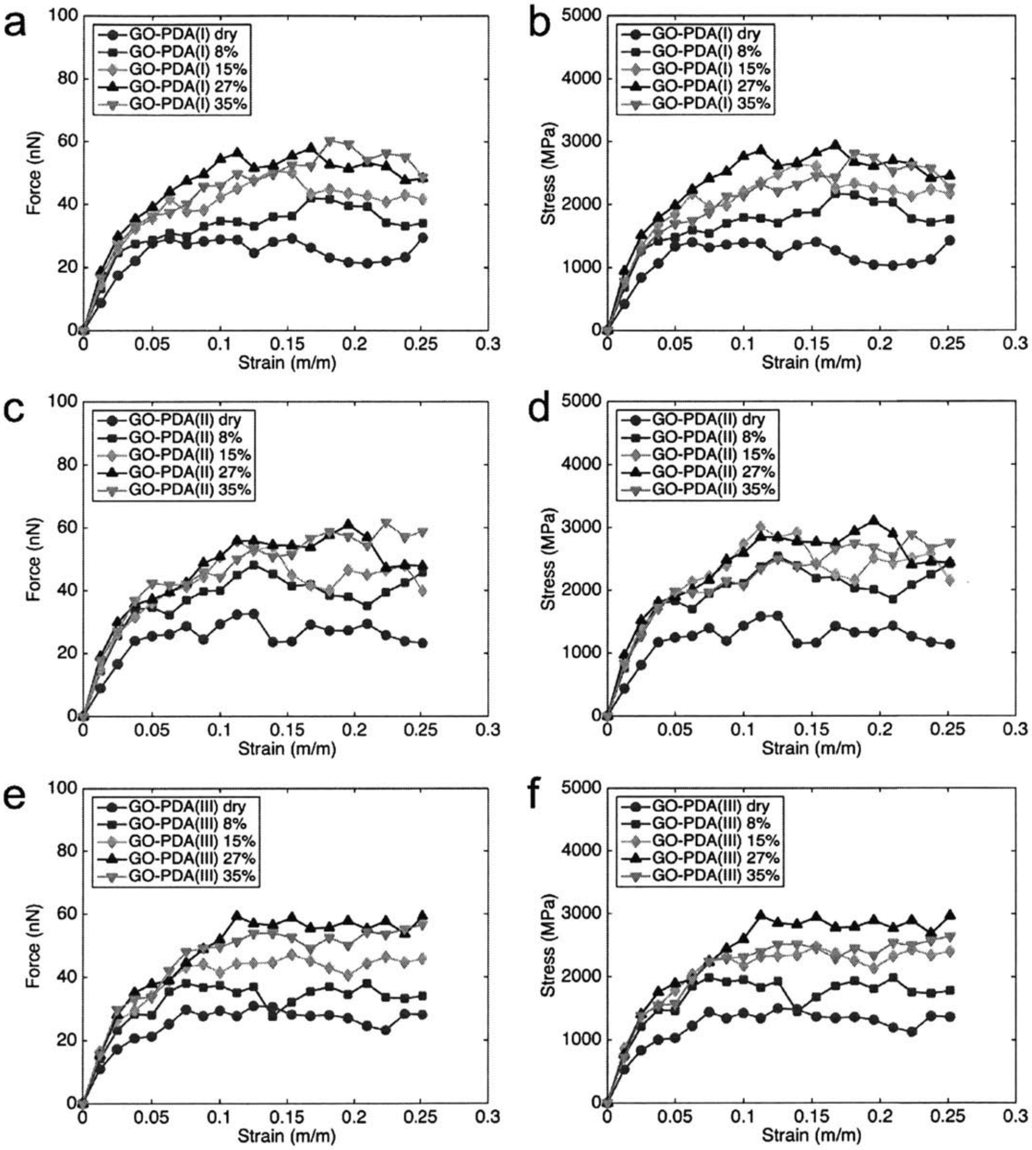

Figure B-24: Force-strain and stress-strain curves for GO–PDA models.

Appendix C

Supplementary simulation data

C	-2.817892	1.255942	0.000249
C	-3.653165	2.472596	0.000097
N	-2.900824	3.595696	-0.000049
C	-1.593339	3.162186	-0.000001
C	-0.416748	3.908658	-0.000078
C	0.863371	3.143171	-0.00015
O	1.979206	3.658893	0.000624
C	0.855637	1.641968	0.000208
O	2.073069	1.095179	0.00035
C	-0.301035	0.938668	0.000305
C	-1.529869	1.678537	0.000185
H	-3.194141	0.240444	0.000395
H	2.706435	1.851993	0.000124
H	-0.302817	-0.153741	0.000489
C	0.783977	6.154075	-0.00021
C	-0.336071	5.346179	-0.000092
N	-1.484809	6.176498	0.000009
C	-1.137632	7.479031	-0.000007
C	-1.946232	8.626131	0.000115
C	-1.212386	9.932066	0.000274
O	-1.743077	11.022618	-0.000628
C	0.355769	9.946528	-0.000545
O	0.922793	11.020735	-0.000526
C	1.059444	8.673309	-0.000365
C	0.345274	7.509161	-0.000199
C	-4.213148	9.804104	0.000257
C	-3.378202	8.587824	0.000148
N	-4.128879	7.467136	0.000083

C	-5.441144	7.900446	0.000137
C	-6.618982	7.162976	0.000094
C	-7.924604	7.923558	0.000098
O	-9.011475	7.376559	-0.000117
C	-7.897599	9.42872	0.0002
O	-9.12899	9.96462	0.000191
C	-6.730768	10.115322	0.000277
C	-5.499642	9.378766	0.000232
C	-7.814935	4.912443	-0.000056
C	-6.697904	5.723988	0.000036
N	-5.546267	4.892268	0.000053
C	-5.890138	3.590504	0.00004
C	-5.081843	2.439396	0.000138
C	-5.81888	1.133297	0.000461
O	-5.290071	0.042629	-0.000983
C	-7.386202	1.12074	-0.000622
O	-7.956085	0.048501	-0.00058
C	-8.088009	2.395769	-0.000297
C	-7.372537	3.558607	-0.000105
H	1.80996	5.81009	-0.000332
H	-2.442556	5.824596	0.000116
H	2.152907	8.688248	-0.00053
H	-3.835185	10.819164	0.000322
H	-9.065118	10.936075	0.000251
H	-6.705352	11.210464	0.000346
H	-8.841802	5.252976	-0.000125
H	-4.588935	5.246514	0.000127
H	-9.181554	2.38318	-0.000437

Table C.1: Atom types and coordinates (unit: Å) of eumelanin tetrameric model proposed by Kaxiras et al. [5]. The molecular structure is optimized using DFT calculations.

C	-6.596462	4.758326	0.204575
C	-7.767197	5.681664	0.049121
N	-8.878707	5.064569	-0.231067
C	-8.559588	3.712062	-0.312884
C	-9.424691	2.720826	-0.648563
C	-8.945703	1.326714	-0.725939
O	-9.677232	0.398623	-1.022798
C	-7.488554	1.106092	-0.416372
O	-7.121835	-0.177751	-0.49264
C	-6.646922	2.134726	-0.081006
C	-7.142887	3.474694	-0.020448
H	-6.179879	-0.27542	-0.261511
H	-10.473803	2.917394	-0.87754
H	-5.61014	1.904544	0.163078
C	-6.650385	8.095879	0.205046
C	-7.796312	7.138541	0.202184
N	-8.958984	7.730831	0.289754
C	-8.701771	9.086259	0.33402
C	-9.654661	10.048228	0.439866
C	-9.252356	11.455269	0.458063
O	-10.035819	12.371955	0.577913
C	-7.735157	11.788183	0.303808
O	-7.443848	12.975179	0.261336
C	-6.745669	10.680425	0.219837
C	-7.255203	9.353284	0.252091
H	-10.715454	9.798483	0.514349
H	-5.666747	13.040299	0.042507
C	-5.261091	7.777583	0.183032
C	-4.177959	8.712558	0.099252
N	-2.99515	7.982173	0.136671
C	-3.253355	6.617659	0.296321
C	-2.2527	5.644207	0.353807
C	-2.757719	4.297217	0.559181

O	-2.080809	3.275228	0.544366
C	-4.264259	4.129475	0.878333
O	-4.5702	3.167083	1.54573
C	-5.248806	5.157921	0.427905
C	-4.694614	6.447839	0.311184
C	-1.665809	8.349232	0.011445
C	-1.001865	9.645055	-0.173359
N	0.314452	9.488635	-0.262185
C	0.570879	8.119196	-0.138635
C	1.724809	7.406029	-0.157927
C	1.668105	5.927816	0.00242
O	2.687337	5.261751	-0.011139
C	0.323436	5.244789	0.18631
O	0.432551	3.93641	0.313929
C	-0.844186	6.000727	0.199566
C	-0.678494	7.415243	0.034667
H	-0.472387	3.522643	0.413829
H	2.714763	7.84797	-0.28752
C	-4.171526	10.148575	0.011125
C	-5.384061	10.995265	0.083735
N	-4.974431	12.285382	-0.002334
C	-3.612068	12.389945	-0.136856
C	-2.87307	13.535273	-0.267194
C	-1.429916	13.459485	-0.402189
O	-0.693411	14.425963	-0.529095
C	-0.846044	12.063821	-0.368904
O	0.447817	12.001352	-0.469368
C	-1.650438	10.910182	-0.229635
C	-3.08128	11.042735	-0.119228
H	0.738776	11.01093	-0.421171
H	-3.332179	14.525948	-0.276796

Table C.2: Atom types and coordinates (unit: Å) of eumelanin pentameric model proposed by Cheng et al. [6, 7]. The molecular structure is optimized using DFT calculations.

C	-14.962405	5.375431	-0.111761
C	-16.132772	4.450071	-0.332022
N	-17.24038	5.10672	-0.560114
C	-16.908976	6.456764	-0.5253
C	-17.763678	7.476881	-0.813363
C	-17.229493	8.824508	-0.810901
O	-17.871263	9.837439	-1.108995
C	-15.797668	9.025726	-0.431108
O	-15.45038	10.312905	-0.498717
C	-14.93547	7.997728	-0.076055
C	-15.495364	6.656838	-0.202316
H	-16.275412	10.772077	-0.814761
H	-18.809117	7.315246	-1.07966
C	-13.552436	8.238312	0.318716
C	-6.181978	8.093144	0.411427
C	-13.611554	4.978752	0.07027
C	-6.216765	4.845034	0.623784
C	-12.448193	7.285133	0.211497
C	-7.296816	7.18903	0.752027
C	-12.468448	5.891358	0.122973
C	-7.323113	5.795346	0.777179
N	-11.22335	7.894586	0.432264
N	-8.465373	7.890816	0.905466
N	-11.291222	5.205698	0.238434
N	-8.545925	5.147474	0.7593
C	-11.472339	9.117711	0.819312
C	-8.200566	9.150373	0.634437
C	-11.59135	3.928435	0.331114
C	-8.305191	3.897225	0.444424
C	-10.512253	10.164488	1.120995
C	-9.151999	10.231242	0.754198
C	-10.647199	2.842476	0.462748
C	-9.263608	2.818744	0.290621
C	-11.079375	11.307901	1.887228
C	-8.628281	11.547787	0.348067

C	-11.321746	1.577358	0.92977
C	-8.718503	1.49316	-0.182463
O	-10.414793	12.079383	2.573544
O	-9.317285	12.548723	0.146567
O	-10.87642	0.919328	1.839969
O	-9.445217	0.603364	-0.585055
C	-12.554268	11.488096	1.936128
C	-7.175195	11.716135	0.013613
C	-12.72167	1.243975	0.396208
C	-7.235043	1.32337	-0.283854
O	-12.939777	12.573251	2.591976
O	-6.906736	12.962346	-0.293957
O	-13.025799	0.06421	0.294687
O	-6.876496	0.097385	-0.674883
C	-13.44641	10.580384	1.413167
C	-6.247592	10.664603	-0.026329
C	-13.633713	2.385254	0.14773
C	-6.360049	2.355376	-0.070799
C	-12.942204	9.394057	0.831931
C	-6.766395	9.361097	0.303963
C	-13.056221	3.694417	0.203951
C	-6.84784	3.635318	0.329558
H	-12.101668	12.992608	2.917934
H	-7.7928	13.423535	-0.225088
H	-14.814607	0.03691	-0.089696
H	-5.906972	0.033363	-0.752336
H	-14.513223	10.769101	1.509259
H	-5.291261	2.188913	-0.232674
C	-16.117853	3.006533	-0.325155
C	-14.986231	2.112533	-0.111597
N	-15.45833	0.824242	-0.198713
C	-16.805996	0.801307	-0.453159
C	-17.651557	-0.254408	-0.613011
C	-19.06717	0.002926	-0.882414
O	-19.891812	-0.881154	-1.039656

C	-19.49282	1.460104	-0.962273
O	-20.791578	1.611263	-1.208984
C	-18.611024	2.497002	-0.795628
C	-17.245393	2.196293	-0.537218
H	-21.019068	2.558846	-1.252725
H	-17.33318	-1.296793	-0.550433
H	-18.916023	3.543205	-0.855077
C	-4.817066	7.694539	0.288676
C	-3.648948	8.59575	0.003155
N	-2.500873	7.962092	0.094412
C	-2.800384	6.657925	0.445714
C	-1.908722	5.686322	0.773276
C	-2.40375	4.384671	1.234993
O	-1.662155	3.479345	1.582805
C	-3.897556	4.189865	1.260763
O	-4.239834	3.006316	1.788403
C	-4.79753	5.135069	0.787204
C	-4.251572	6.446063	0.502041
H	-5.20525	2.968979	1.929128
H	-0.829076	5.847452	0.752845
C	-3.699188	9.98024	-0.373653
C	-4.865363	10.934731	-0.414257
N	-4.508365	12.124965	-0.834962
C	-3.151745	12.06777	-1.099207
C	-2.376293	13.077664	-1.575015
C	-0.953406	12.807787	-1.786464
O	-0.147245	13.628282	-2.212083
C	-0.422223	11.42724	-1.463728
O	0.880499	11.294663	-1.688276
C	-1.223088	10.428122	-0.98802
C	-2.608189	10.726839	-0.801623
H	1.187558	12.172395	-2.025241
H	-2.769497	14.069471	-1.803661
H	-0.83563	9.438921	-0.751429

Table C.3: Atom types and coordinates (unit: Å) of eumelanin octameric model proposed by Cheng et al. [6, 7]. The molecular structure is optimized using DFT calculations.

C	-7.790908	5.002893	-0.002731
C	-6.488093	5.867092	-0.026004
N	-5.407027	4.890595	-0.005158
C	-5.873416	3.591093	0.031108
C	-5.151616	2.390947	0.0621
C	-5.844596	1.170511	0.096848
O	-5.203583	-0.031076	0.128464
C	-7.25549	1.14782	0.100693
O	-7.867159	-0.077554	0.135951
C	-7.958045	2.360606	0.069323
C	-7.277629	3.575619	0.034774
H	-8.415153	5.244307	0.877156
H	-4.430187	5.143993	-0.01137
H	-9.055336	2.338243	0.072731
H	-8.828857	0.054019	0.134592
H	-4.244492	0.121229	0.121987
H	-8.415791	5.197408	-0.893707
H	-6.438161	6.546164	0.848299
H	-6.441871	6.503904	-0.93155
H	-4.055448	2.388807	0.059946

Table C.4: Atom types and coordinates (unit: Å) of eumelanin monomeric model (M1) proposed by Dreyer et al. [8]. The molecular structure is optimized using DFT calculations.

C	0.744963	6.102932	0.002474
C	-0.543527	5.239162	0.002538
N	-1.620615	6.219489	0.000719
C	-1.226016	7.52131	0.000158
C	-1.985694	8.659458	-0.001289
C	-1.338042	9.959021	-0.00163
O	-1.932037	11.023175	-0.003536
C	0.228571	9.983385	0.0004
O	0.820919	11.041058	-0.001209
C	0.946938	8.686677	0.001239
C	0.252382	7.533518	0.001347
H	1.371532	5.898445	-0.882803
H	-2.596991	5.949632	0.000163
H	2.04116	8.7254	0.002
H	1.370951	5.899536	0.888406
H	-0.603517	4.586826	0.893937
H	-0.602326	4.584843	-0.887481
H	-3.07898	8.635843	-0.002258

Table C.5: Atom types and coordinates (unit: Å) of eumelanin monomeric model (M2) proposed by Dreyer et al. [8]. The molecular structure is optimized using DFT calculations.

Bibliography

[1] Haeshin Lee, Shara M Dellatore, William M Miller, and Phillip B Messersmith. Mussel-inspired surface chemistry for multifunctional coatings. *Science*, 318(5849):426–430, 2007.

[2] Marco d'Ischia, Alessandra Napolitano, Vincent Ball, Chun-Teh Chen, and Markus J. Buehler. Polydopamine and eumelanin: from structure–property relationships to a unified tailoring strategy. *Accounts of Chemical Research*, 47(12):3541–3550, 2014.

[3] GW Zajac, JM Gallas, J Cheng, M Eisner, SC Moss, and AE Alvarado-Swaisgood. The fundamental unit of synthetic melanin: a verification by tunneling microscopy of x-ray scattering results. *Biochimica et Biophysica Acta (BBA)-General Subjects*, 1199(3):271–278, 1994.

[4] Adri CT Van Duin, Siddharth Dasgupta, Francois Lorant, and William A Goddard. Reaxff: a reactive force field for hydrocarbons. *The Journal of Physical Chemistry A*, 105(41):9396–9409, 2001.

[5] Efthimios Kaxiras, Argyrios Tsolakidis, George Zonios, and Sheng Meng. Structural model of eumelanin. *Physical Review Letters*, 97(21):218102, 2006.

[6] Jin Cheng, Simon C Moss, Melvin Eisner, and Paul Zschack. X-ray characterization of melanins—i. *Pigment Cell Research*, 7(4):255–262, 1994.

[7] Jin Cheng, Simon C Moss, and Melvin Eisner. X-ray characterization of melanins—ii. *Pigment Cell Research*, 7(4):263–273, 1994.

[8] Daniel R Dreyer, Daniel J Miller, Benny D Freeman, Donald R Paul, and Christopher W Bielawski. Elucidating the structure of poly (dopamine). *Langmuir*, 28(15):6428–6435, 2012.

[9] Chun-Teh Chen, Chern Chuang, Jianshu Cao, Vincent Ball, David Ruch, and Markus J. Buehler. Excitonic effects from geometric order and disorder explain broadband optical absorption in eumelanin. *Nature Communications*, 5, 2014.

[10] Chun-Teh Chen, Vincent Ball, José Joaquim de Almeida Gracio, Manoj Kumar Singh, Valérie Toniazzo, David Ruch, and Markus J. Buehler. Self-assembly of tetramers of 5, 6-dihydroxyindole explains the primary physical properties of

eumelanin: Experiment, simulation, and design. *ACS Nano*, 7(2):1524–1532, 2013.

[11] Shangchao Lin, Chun-Teh Chen, Igor Bdikin, Vincent Ball, José Grácio, and Markus J. Buehler. Tuning heterogeneous poly(dopamine) structures and mechanics: in silico covalent cross-linking and thin film nanoindentation. *Soft Matter*, 10(3):457–464, 2014.

[12] Lucia Panzella, Alessandro Pezzella, Alessandra Napolitano, and Marco d'Ischia. The first 5, 6-dihydroxyindole tetramer by oxidation of 5, 5', 6, 6'-tetrahydroxy-2, 4'-biindolyl and an unexpected issue of positional reactivity en route to eumelanin-related polymers. *Organic Letters*, 9(7):1411–1414, 2007.

[13] Marianna Arzillo, Alessandro Pezzella, Orlando Crescenzi, Alessandra Napolitano, Edward J Land, Vincenzo Barone, and Marco d'Ischia. Cyclic structural motifs in 5, 6-dihydroxyindole polymerization uncovered: biomimetic modular buildup of a unique five-membered macrocycle. *Organic Letters*, 12(14):3250–3253, 2010.

[14] Marco d'Ischia, Kazumasa Wakamatsu, Alessandra Napolitano, Stefania Briganti, José-Carlos Garcia-Borron, Daniela Kovacs, Paul Meredith, Alessandro Pezzella, Mauro Picardo, Tadeusz Sarna, et al. Melanins and melanogenesis: methods, standards, protocols. *Pigment Cell & Melanoma Research*, 26(5):616–633, 2013.

[15] Dana N Peles, Lian Hong, Dan-Ning Hu, Shosuke Ito, Robert J Nemanich, and John D Simon. Human iridal stroma melanosomes of varying pheomelanin contents possess a common eumelanic outer surface. *The Journal of Physical Chemistry B*, 113(32):11346–11351, 2009.

[16] Nikiforos Kollias, Robert M Sayre, Lisa Zeise, and Miles R Chedekel. New trends in photobiology: Photoprotection by melanin. *Journal of Photochemistry and Photobiology B: Biology*, 9(2):135–160, 1991.

[17] Christine MR Clancy, J Brian Nofsinger, R Kyle Hanks, and John D Simon. A hierarchical self-assembly of eumelanin. *The Journal of Physical Chemistry B*, 104(33):7871–7873, 2000.

[18] J Brian Nofsinger, Susan E Forest, and John D Simon. Explanation for the disparity among absorption and action spectra of eumelanin. *The Journal of Physical Chemistry B*, 103(51):11428–11432, 1999.

[19] J Brian Nofsinger and John D Simon. Radiative relaxation of sepia eumelanin is affected by aggregation. *Photochemistry and Photobiology*, 74(1):31–37, 2001.

[20] M Linh Tran, Ben J Powell, and Paul Meredith. Chemical and structural disorder in eumelanins: a possible explanation for broadband absorbance. *Biophysical Journal*, 90(3):743–752, 2006.

[21] Hao Ou-Yang, Georgios Stamatas, and Nikiforos Kollias. Spectral responses of melanin to ultraviolet a irradiation. *Journal of Investigative Dermatology*, 122(2):492–496, 2004.

[22] Michaela Brenner and Vincent J Hearing. The protective role of melanin against uv damage in human skin. *Photochemistry and Photobiology*, 84(3):539–549, 2008.

[23] Tom Lister, Philip A Wright, and Paul H Chappell. Optical properties of human skin. *Journal of Biomedical Optics*, 17(9):0909011–09090115, 2012.

[24] Annemarie Huijser, Alessandro Pezzella, and Villy Sundström. Functionality of epidermal melanin pigments: current knowledge on uv-dissipative mechanisms and research perspectives. *Physical Chemistry Chemical Physics*, 13(20):9119–9127, 2011.

[25] Gertrude-E Costin and Vincent J Hearing. Human skin pigmentation: melanocytes modulate skin color in response to stress. *The FASEB Journal*, 21(4):976–994, 2007.

[26] Jennifer Jean Riesz. *The spectroscopic properties of melanin.* University of Queensland, 2007.

[27] Jennifer Y Lin and David E Fisher. Melanocyte biology and skin pigmentation. *Nature*, 445(7130):843–850, 2007.

[28] Paul Meredith and Tadeusz Sarna. The physical and chemical properties of eumelanin. *Pigment Cell Research*, 19(6):572–594, 2006.

[29] Wenbo Sheng, Bin Li, Xiaolong Wang, Bin Dai, Bo Yu, Xin Jia, and Feng Zhou. Brushing up from "anywhere" under sunlight: a universal surface-initiated polymerization from polydopamine-coated surfaces. *Chemical Science*, 6(3):2068–2073, 2015.

[30] Vincent Ball, Doriane Del Frari, Marc Michel, Markus J. Buehler, Valérie Toniazzo, Manoj K Singh, Jose Gracio, and David Ruch. Deposition mechanism and properties of thin polydopamine films for high added value applications in surface science at the nanoscale. *BioNanoScience*, 2(1):16–34, 2012.

[31] Sook Hee Ku, Joon Seok Lee, and Chan Beum Park. Spatial control of cell adhesion and patterning through mussel-inspired surface modification by polydopamine. *Langmuir*, 26(19):15104–15108, 2010.

[32] Hongcai Gao, Yimin Sun, Jiajing Zhou, Rong Xu, and Hongwei Duan. Mussel-inspired synthesis of polydopamine-functionalized graphene hydrogel as reusable adsorbents for water purification. *ACS Applied Materials & Interfaces*, 5(2):425–432, 2013.

[33] Zhen Li, Xiaoyong Zhang, Shiqi Wang, Yang Yang, Benye Qin, Ke Wang, Tao Xie, Yen Wei, and Yan Ji. Polydopamine coated shape memory polymer: enabling light triggered shape recovery, light controlled shape reprogramming and surface functionalization. *Chemical Science*, 2016.

[34] Jiuke Mu, Chengyi Hou, Hongzhi Wang, Yaogang Li, Qinghong Zhang, and Meifang Zhu. Origami-inspired active graphene-based paper for programmable instant self-folding walking devices. *Science Advances*, 1(10):e1500533, 2015.

[35] Martin E Lynge, Rebecca van der Westen, Almar Postma, and Brigitte Städler. Polydopamine—a nature-inspired polymer coating for biomedical science. *Nanoscale*, 3(12):4916–4928, 2011.

[36] Weibing Qiang, Wei Li, Xiaoqing Li, Xiang Chen, and Danke Xu. Bioinspired polydopamine nanospheres: a superquencher for fluorescence sensing of biomolecules. *Chemical Science*, 5(8):3018–3024, 2014.

[37] Ben Wang, Guangchuan Wang, Binjie Zhao, Jiajun Chen, Xueyun Zhang, and Ruikang Tang. Antigenically shielded universal red blood cells by polydopamine-based cell surface engineering. *Chemical Science*, 5(9):3463–3468, 2014.

[38] Sung Min Kang, Sungjin Park, Daewon Kim, Sung Young Park, Rodney S Ruoff, and Haeshin Lee. Simultaneous reduction and surface functionalization of graphene oxide by mussel-inspired chemistry. *Advanced Functional Materials*, 21(1):108–112, 2011.

[39] Shosuke Ito. A chemist's view of melanogenesis. *Pigment Cell Research*, 16(3):230–236, 2003.

[40] Andrew AR Watt, Jacques P Bothma, and Paul Meredith. The supramolecular structure of melanin. *Soft Matter*, 5(19):3754–3760, 2009.

[41] Yan Liu and John D Simon. Isolation and biophysical studies of natural eumelanins: applications of imaging technologies and ultrafast spectroscopy. *Pigment Cell Research*, 16(6):606–618, 2003.

[42] GW Zajac, JM Gallas, and AE Alvarado-Swaisgood. Tunneling microscopy verification of an x-ray scattering-derived molecular model of tyrosine-based melanin. *Journal of Vacuum Science & Technology B*, 12(3):1512–1516, 1994.

[43] Pilar Díaz, Yurima Gimeno, Pilar Carro, Sergio González, Patricia L Schilardi, Guillermo Benítez, Roberto C Salvarezza, and Alberto Hernández Creus. Electrochemical self-assembly of melanin films on gold. *Langmuir*, 21(13):5924–5930, 2005.

[44] Alessandra Napolitano, Alessandro Pezzella, Giuseppe Prota, Roberta Seraglia, and Pietro Traldi. Structural analysis of synthetic melanins from 5, 6-dihydroxyindole by matrix-assisted laser desorption/ionization mass spectrometry. *Rapid Communications in Mass Spectrometry*, 10(4):468–472, 1996.

[45] Alessandro Pezzella, Alessandra Napolitano, Marco d'Ischia, Giuseppe Prota, Roberta Seraglia, and Pietro Traldi. Identification of partially degraded oligomers of 5, 6-dihydroxyindole-2-carboxylic acid in sepia melanin by matrix-assisted laser desorption/ionization mass spectrometry. *Rapid Communications in Mass Spectrometry*, 11(4):368–372, 1997.

[46] Antonella Bertazzo, Carlo Costa, Graziella Allegri, Roberta Seraglia, and Pietro Traldi. Biosynthesis of melanin from dopamine. an investigation of early oligomerization products. *Rapid Communications in Mass Spectrometry*, 9(8):634–640, 1995.

[47] Antonella Bertazzo, Carlo VL Costa, Graziella Allegri, Marta Schiavolin, Donata Favretto, and Pietro Traldi. Enzymatic oligomerization of tyrosine by tyrosinase and peroxidase studied by matrix-assisted laser desorption/ionization mass spectrometry. *Rapid Communications in Mass Spectrometry*, 13(6):542–547, 1999.

[48] Christoph Kroesche and Martin G Peter. Detection of melanochromes by maldi-tof mass spectrometry. *Tetrahedron*, 52(11):3947–3952, 1996.

[49] Samantha Reale, Marcello Crucianelli, Alessandro Pezzella, Marco d'Ischia, and Francesco De Angelis. Exploring the frontiers of synthetic eumelanin polymers by high-resolution matrix-assisted laser/desorption ionization mass spectrometry. *Journal of Mass Spectrometry*, 47(1):49–53, 2012.

[50] Jürgen Liebscher, Radosław Mrówczyński, Holger A Scheidt, Claudiu Filip, Niculina D Hădade, Rodica Turcu, Attila Bende, and Sebastian Beck. Structure of polydopamine: a never-ending story? *Langmuir*, 29(33):10539–10548, 2013.

[51] Klaus B Stark, James M Gallas, Gerry W Zajac, Melvin Eisner, and Joseph T Golab. Spectroscopic study and simulation from recent structural models for eumelanin: I. monomer, dimers. *The Journal of Physical Chemistry B*, 107(13):3061–3067, 2003.

[52] Klaus B Stark, James M Gallas, Gerry W Zajac, Melvin Eisner, and Joseph T Golab. Spectroscopic study and simulation from recent structural models for eumelanin: Ii. oligomers. *The Journal of Physical Chemistry B*, 107(41):11558–11562, 2003.

[53] Sheng Meng and Efthimios Kaxiras. Theoretical models of eumelanin protomolecules and their optical properties. *Biophysical Journal*, 94(6):2095–2105, 2008.

[54] Klaus B Stark, James M Gallas, Gerry W Zajac, Joseph T Golab, Shirley Gidanian, Theresa McIntire, and Patrick J Farmer. Effect of stacking and redox state on optical absorption spectra of melanins-comparison of theoretical and experimental results. *The Journal of Physical Chemistry B*, 109(5):1970–1977, 2005.

[55] Paul Meredith, Ben J Powell, Jennifer Riesz, Stephen P Nighswander-Rempel, Mark R Pederson, and Evan G Moore. Towards structure–property–function relationships for eumelanin. *Soft Matter*, 2(1):37–44, 2006.

[56] George Zonios, Aikaterini Dimou, Ioannis Bassukas, Dimitrios Galaris, Argyrios Tsolakidis, and Efthimios Kaxiras. Melanin absorption spectroscopy: new method for noninvasive skin investigation and melanoma detection. *Journal of Biomedical Optics*, 13(1):014017–014017, 2008.

[57] Steve Plimpton. Fast parallel algorithms for short-range molecular dynamics. *Journal of Computational Physics*, 117(1):1–19, 1995.

[58] Pnina Dauber-Osguthorpe, Victoria A Roberts, David J Osguthorpe, Jon Wolff, Moniqe Genest, and Arnold T Hagler. Structure and energetics of ligand binding to proteins: Escherichia coli dihydrofolate reductase-trimethoprim, a drug-receptor system. *Proteins: Structure, Function, and Bioinformatics*, 4(1):31–47, 1988.

[59] Jon R Maple, Uri Dinur, and Arnold T Hagler. Derivation of force fields for molecular mechanics and dynamics from ab initio energy surfaces. *Proceedings of the National Academy of Sciences*, 85(15):5350–5354, 1988.

[60] Chun-Teh Chen, Soumyajit Ghosh, C Malla Reddy, and Markus J. Buehler. Molecular mechanics of elastic and bendable caffeine co-crystals. *Physical Chemistry Chemical Physics*, 16(26):13165–13171, 2014.

[61] Oral Büyüköztürk, Markus J. Buehler, Denvid Lau, and Chakrapan Tuakta. Structural solution using molecular dynamics: Fundamentals and a case study of epoxy-silica interface. *International Journal of Solids and Structures*, 48(14):2131–2140, 2011.

[62] M Segall, P Linda, M Probert, C Pickard, P Hasnip, S Clark, and M Payne. Materials studio castep, version 2.2. *Accelrys: San Diego, CA*, 2002.

[63] Nikhil V Medhekar, Ashwin Ramasubramaniam, Rodney S Ruoff, and Vivek B Shenoy. Hydrogen bond networks in graphene oxide composite paper: structure and mechanical properties. *ACS Nano*, 4(4):2300–2306, 2010.

[64] Owen C Compton, Steven W Cranford, Karl W Putz, Zhi An, L Catherine Brinson, Markus J. Buehler, and SonBinh T Nguyen. Tuning the mechanical properties of graphene oxide paper and its associated polymer nanocomposites by controlling cooperative intersheet hydrogen bonding. *ACS Nano*, 6(3):2008–2019, 2012.

[65] JM Gallas, KC Littrell, S Seifert, GW Zajac, and P Thiyagarajan. Solution structure of copper ion-induced molecular aggregates of tyrosine melanin. *Biophysical Journal*, 77(2):1135–1142, 1999.

[66] Christine MR Clancy and John D Simon. Ultrastructural organization of eumelanin from sepia officinalis measured by atomic force microscopy. *Biochemistry*, 40(44):13353–13360, 2001.

[67] Yuta Miyasaka, Atsushi Nakamura, and Jiro Temmyo. Graphite thin films consisting of nanograins of multilayer graphene on sapphire substrates directly grown by alcohol chemical vapor deposition. *Japanese Journal of Applied Physics*, 50(4S):04DH12, 2011.

[68] Sheng Meng and Efthimios Kaxiras. Mechanisms for ultrafast nonradiative relaxation in electronically excited eumelanin constituents. *Biophysical Journal*, 95(9):4396–4402, 2008.

[69] Bernard F Godley, Farrukh A Shamsi, Fong-Qi Liang, Stuart G Jarrett, Sallyanne Davies, and Mike Boulton. Blue light induces mitochondrial dna damage and free radical production in epithelial cells. *Journal of Biological Chemistry*, 280(22):21061–21066, 2005.

[70] Marco d'Ischia, Alessandra Napolitano, Alessandro Pezzella, Paul Meredith, and Tadeusz Sarna. Chemical and structural diversity in eumelanins: Unexplored bio-optoelectronic materials. *Angewandte Chemie International Edition*, 48(22):3914–3921, 2009.

[71] Frank Neese. The orca program system. *Wiley Interdisciplinary Reviews: Computational Molecular Science*, 2(1):73–78, 2012.

[72] Chengteh Lee, Weitao Yang, and Robert G Parr. Development of the colle-salvetti correlation-energy formula into a functional of the electron density. *Physical Review B*, 37(2):785, 1988.

[73] Axel D Becke. A new mixing of hartree–fock and local density-functional theories. *The Journal of Chemical Physics*, 98(2):1372–1377, 1993.

[74] Ansgar Schäfer, Hans Horn, and Reinhart Ahlrichs. Fully optimized contracted gaussian basis sets for atoms li to kr. *The Journal of Chemical Physics*, 97(4):2571–2577, 1992.

[75] MJ Frisch, GW Trucks, HB Schlegel, GE Scuseria, MA Robb, JR Cheeseman, G Scalmani, V Barone, B Mennucci, GA Petersson, et al. Gaussian 09, rev. b. 01. *Gaussian Inc., Wallingford CT*, 2010.

[76] SM Vlaming, R Augulis, MCA Stuart, J Knoester, and PHM Van Loosdrecht. Exciton spectra and the microscopic structure of self-assembled porphyrin nanotubes. *The Journal of Physical Chemistry B*, 113(8):2273–2283, 2009.

[77] Carole Ecoffet, Dimitra Markovitsi, Philippe Millié, and Jean-Pierre Lemaistre. Electronic excitations in organized molecular systems. a model for columnar aggregates of ionic compounds. *Chemical Physics*, 177(3):629–643, 1993.

[78] Sylvie Marguet, Dimitra Markovitsi, Philippe Millie, Herve Sigal, and Sandeep Kumar. Influence of disorder on electronic excited states: an experimental and numerical study of alkylthiotriphenylene columnar phases. *The Journal of Physical Chemistry B*, 102(24):4697–4710, 1998.

[79] David Beljonne, Jérôme Cornil, R Silbey, P Millié, and Jean-Luc Brédas. Interchain interactions in conjugated materials: the exciton model versus the supermolecular approach. *The Journal of Chemical Physics*, 112(10):4749–4758, 2000.

[80] Wichard JD Beenken and Tonu Pullerits. Excitonic coupling in polythiophenes: comparison of different calculation methods. *The Journal of Chemical Physics*, 120(5):2490–2495, 2004.

[81] Jean-Christophe Denis, Stefan Schumacher, and Ian Galbraith. Quantitative description of interactions between linear organic chromophores. *The Journal of Chemical Physics*, 137(22):224102, 2012.

[82] Henk Fidder, Jasper Knoester, and Douwe A Wiersma. Optical properties of disordered molecular aggregates: a numerical study. *The Journal of Chemical Physics*, 95(11):7880–7890, 1991.

[83] EW Knapp. Lineshapes of molecular aggregates, exchange narrowing and intersite correlation. *Chemical Physics*, 85(1):73–82, 1984.

[84] Demet Gülen. Significance of the excitonic intensity borrowing in the j-/h-aggregates of bacteriochlorophylls/chlorophylls. *Photosynthesis Research*, 87(2):205–214, 2006.

[85] Frank C Spano. The spectral signatures of frenkel polarons in h-and j-aggregates. *Accounts of Chemical Research*, 43(3):429–439, 2009.

[86] Laura Ascione, Alessandro Pezzella, Veronica Ambrogi, Cosimo Carfagna, and Marco d'Ischia. Intermolecular π-electron perturbations generate extrinsic visible contributions to eumelanin black chromophore in model polymers with interrupted interring conjugation. *Photochemistry and Photobiology*, 89(2):314–318, 2013.

[87] Alessandro Pezzella, Alfonso Iadonisi, Silvia Valerio, Lucia Panzella, Alessandra Napolitano, Matteo Adinolfi, and Marco d'Ischia. Disentangling eumelanin "black chromophore": visible absorption changes as signatures of oxidation state-and aggregation-dependent dynamic interactions in a model water-soluble 5, 6-dihydroxyindole polymer. *Journal of the American Chemical Society*, 131(42):15270–15275, 2009.

[88] Dana N Moses, Michael A Mattoni, Nelle L Slack, J Herbert Waite, and Frank W Zok. Role of melanin in mechanical properties of glycera jaws. *Acta Biomaterialia*, 2(5):521–530, 2006.

[89] Dana N Moses, John H Harreld, Galen D Stucky, and J Herbert Waite. Melanin and glycera jaws emerging dark side of a robust biocomposite structure. *Journal of Biological Chemistry*, 281(46):34826–34832, 2006.

[90] Marianna Arzillo, Gaetano Mangiapia, Alessandro Pezzella, Richard K Heenan, Aurel Radulescu, Luigi Paduano, and Marco d'Ischia. Eumelanin buildup on the nanoscale: aggregate growth/assembly and visible absorption development in biomimetic 5, 6-dihydroxyindole polymerization. *Biomacromolecules*, 13(8):2379–2390, 2012.

[91] Zhao Qin and Markus J. Buehler. Molecular mechanics of dihydroxyphenylalanine at a silica interface. *Applied Physics Letters*, 101(8):083702, 2012.

[92] Zhao Qin and Markus J. Buehler. Mechanical properties of crosslinks controls failure mechanism of hierarchical intermediate filament networks. *Theoretical and Applied Mechanics Letters*, 2(1):014005, 2012.

[93] Markus J. Buehler. Nanomechanics of collagen fibrils under varying cross-link densities: atomistic and continuum studies. *Journal of the Mechanical Behavior of Biomedical Materials*, 1(1):59–67, 2008.

[94] Lisa Zeise, Rudolph B Addison, and Miles R Chedekel. Bio-analytical studies of eumelanins. i. characterization of melanin the particle. *Pigment Cell Research*, 3(S2):48–53, 1990.

[95] B Brushan. Handbook of nanotechnology, 2007.

[96] Hidekazu Okuda, Kyoji Yoshino, Kazumasa Wakamatsu, Shosuke Ito, and Takayuki Sota. Degree of polymerization of 5, 6-dihydroxyindole-derived eumelanin from chemical degradation study. *Pigment Cell & Melanoma Research*, 27(4):664–667, 2014.

[97] Paul Geerlings, F De Proft, and W Langenaeker. Conceptual density functional theory. *Chemical Reviews*, 103(5):1793–1874, 2003.

[98] Young Jo Kim, Abhishek Khetan, Wei Wu, Sang-Eun Chun, Venkatasubramanian Viswanathan, Jay F Whitacre, and Christopher J Bettinger. Evidence of porphyrin-like structures in natural melanin pigments using electrochemical fingerprinting. *Advanced Materials*, 2016.

[99] Changgu Lee, Xiaoding Wei, Jeffrey W Kysar, and James Hone. Measurement of the elastic properties and intrinsic strength of monolayer graphene. *Science*, 321(5887):385–388, 2008.

[100] Weiwei Cai, Richard D Piner, Frank J Stadermann, Sungjin Park, Medhat A Shaibat, Yoshitaka Ishii, Dongxing Yang, Aruna Velamakanni, Sung Jin An, Meryl Stoller, et al. Synthesis and solid-state nmr structural characterization of 13c-labeled graphite oxide. *Science*, 321(5897):1815–1817, 2008.

[101] Jeffrey T Paci, Ted Belytschko, and George C Schatz. Computational studies of the structure, behavior upon heating, and mechanical properties of graphite oxide. *The Journal of Physical Chemistry C*, 111(49):18099–18111, 2007.

[102] Dmitriy A Dikin, Sasha Stankovich, Eric J Zimney, Richard D Piner, Geoffrey HB Dommett, Guennadi Evmenenko, SonBinh T Nguyen, and Rodney S Ruoff. Preparation and characterization of graphene oxide paper. *Nature*, 448(7152):457–460, 2007.

[103] Chengmeng Chen, Quan-Hong Yang, Yonggang Yang, Wei Lv, Yuefang Wen, Peng-Xiang Hou, Maozhang Wang, and Hui-Ming Cheng. Self-assembled free-standing graphite oxide membrane. *Advanced Materials*, 21(29):3007–3011, 2009.

[104] Haiqun Chen, Marc B Müller, Kerry J Gilmore, Gordon G Wallace, and Dan Li. Mechanically strong, electrically conductive, and biocompatible graphene paper. *Advanced Materials*, 20(18):3557–3561, 2008.

[105] Yanwu Zhu, Shanthi Murali, Weiwei Cai, Xuesong Li, Ji Won Suk, Jeffrey R Potts, and Rodney S Ruoff. Graphene and graphene oxide: synthesis, properties, and applications. *Advanced Materials*, 22(35):3906–3924, 2010.

[106] Ye Tian, Yewen Cao, Yu Wang, Wuli Yang, and Jiachun Feng. Realizing ultrahigh modulus and high strength of macroscopic graphene oxide papers through crosslinking of mussel-inspired polymers. *Advanced Materials*, 25(21):2980–2983, 2013.

[107] Wonoh Lee, Jea Uk Lee, Byung Mun Jung, Joon-Hyung Byun, Jin-Woo Yi, Sang-Bok Lee, and Byung-Sun Kim. Simultaneous enhancement of mechanical, electrical and thermal properties of graphene oxide paper by embedding dopamine. *Carbon*, 65:296–304, 2013.

[108] Wei Cui, Mingzhu Li, Jiyang Liu, Ben Wang, Chuck Zhang, Lei Jiang, and Qunfeng Cheng. A strong integrated strength and toughness artificial nacre based on dopamine cross-linked graphene oxide. *ACS Nano*, 8(9):9511–9517, 2014.

[109] Karl W Putz, Owen C Compton, Marc J Palmeri, SonBinh T Nguyen, and L Catherine Brinson. High-nanofiller-content graphene oxide–polymer nanocomposites via vacuum-assisted self-assembly. *Advanced Functional Materials*, 20(19):3322–3329, 2010.

[110] Yuan-Qing Li, Ting Yu, Tian-Yi Yang, Lian-Xi Zheng, and Kin Liao. Bio-inspired nacre-like composite films based on graphene with superior mechanical, electrical, and biocompatible properties. *Advanced Materials*, 24(25):3426–3431, 2012.

[111] Mingyang Ji, Nan Jiang, Jian Chang, and Junqi Sun. Near-infrared light-driven, highly efficient bilayer actuators based on polydopamine-modified reduced graphene oxide. *Advanced Functional Materials*, 24(34):5412–5419, 2014.

[112] Changhong Cao, Matthew Daly, Chandra Veer Singh, Yu Sun, and Tobin Filleter. High strength measurement of monolayer graphene oxide. *Carbon*, 81:497–504, 2015.

[113] Goki Eda and Manish Chhowalla. Chemically derived graphene oxide: towards large-area thin-film electronics and optoelectronics. *Advanced Materials*, 22(22):2392–2415, 2010.

[114] Kimberly Chenoweth, Adri CT Van Duin, and William A Goddard. Reaxff reactive force field for molecular dynamics simulations of hydrocarbon oxidation. *The Journal of Physical Chemistry A*, 112(5):1040–1053, 2008.

[115] Akbar Bagri, Cecilia Mattevi, Muge Acik, Yves J Chabal, Manish Chhowalla, and Vivek B Shenoy. Structural evolution during the reduction of chemically derived graphene oxide. *Nature Chemistry*, 2(7):581–587, 2010.

[116] Amar M Kamat, Adri CT van Duin, and Alexei Yakovlev. Molecular dynamics simulations of laser-induced incandescence of soot using an extended reaxff reactive force field. *The Journal of Physical Chemistry A*, 114(48):12561–12572, 2010.

[117] Fidel Castro-Marcano, Amar M Kamat, Michael F Russo, Adri CT van Duin, and Jonathan P Mathews. Combustion of an illinois no. 6 coal char simulated using an atomistic char representation and the reaxff reactive force field. *Combustion and Flame*, 159(3):1272–1285, 2012.

[118] In Kyu Moon, Junghyun Lee, Rodney S Ruoff, and Hyoyoung Lee. Reduced graphene oxide by chemical graphitization. *Nature Communications*, 1:73, 2010.

[119] Yanzhong Hong, Zhiyong Wang, and Xianbo Jin. Sulfuric acid intercalated graphite oxide for graphene preparation. *Scientific Reports*, 3:3439, 2013.

[120] A Lerf, A Buchsteiner, J Pieper, S Schöttl, I Dekany, T Szabo, and HP Boehm. Hydration behavior and dynamics of water molecules in graphite oxide. *Journal of Physics and Chemistry of Solids*, 67(5):1106–1110, 2006.

[121] Yilun Liu, Bo Xie, Zhong Zhang, Quanshui Zheng, and Zhiping Xu. Mechanical properties of graphene papers. *Journal of the Mechanics and Physics of Solids*, 60(4):591–605, 2012.